Effects of Two-Phase Flow in a Multistage Centrifugal Compressor

Chaitanya Vishwajit Halbe

Dissertation submitted to the Faculty of the

Virginia Polytechnic Institute and State University

in partial fulfillment of the requirements for the degree of

Doctor of Philosophy

in

Mechanical Engineering

Walter F. O'Brien, Chair

K. Todd Lowe

Danesh K. Tafti

Brian Vick

William T. Cousins

Vishnu Sishtla

September 22, 2016

Blacksburg, Virginia

Keywords: Turbomachinery, Compressor, Centrifugal, Multistage, Multiphase, CFD, Performance

Effects of Two-Phase Flow in a Multistage Centrifugal Compressor

Chaitanya Vishwajit Halbe

ABSTRACT

The performance of a vapor compression system is known to be affected by the ingestion of liquid droplets in the compressor. In these multiphase flows, the liquid and the vapor phase are tightly coupled. Therefore the interphase heat, mass and momentum transfer as well as droplet dynamics including droplet breakup and droplet-wall interactions play a vital role in governing these flows. Only thermodynamic analyses or two-dimensional mean-line calculations are not sufficient to gain an in-depth understanding of the complex multiphase flow field within the compressor. The objective of this research was to extend the current understanding of the operation of a multistage centrifugal compressor under two-phase flow conditions, by performing three-dimensional computational analysis.

In this work, two-phase flow of a single constituent (refrigerant R134a) through a two-stage, in-line centrifugal compressor was analyzed using CFD. The CFD model accounted for real gas behavior of the vapor phase. Novel user defined routines were implemented to ensure accurate calculations of interphase heat, mass and momentum transfer terms and to model droplet impact on the compressor surfaces. An erosion model was developed and implemented to locate the erosion "hot spots" and to estimate the amount of material eroded.

To understand the effects of increasing liquid carryover, the mass flow rate of the liquid phase was increased from 1% to 5% of the vapor mass flow rate. The influence of droplet size on the compressor performance was assessed by varying the droplet diameter at the inlet from 100 microns to 400 microns. The results of the two-phase flow simulations were compared with the simulation involving only the vapor phase.

Liquid carryover altered the flow field within the compressor, and as a result, both impellers were observed to operate at off-design conditions. This effect was more pronounced for the second impeller. The overall effects of liquid carryover were detrimental to the compressor performance. The erosion calculations showed maximum erosion potential on the blade and shroud of the first impeller.

The results from this investigation provided new and useful information that can be used to support improved design solutions.

Effects of Two-Phase Flow in a Multistage Centrifugal Compressor

Chaitanya Vishwajit Halbe

GENERAL AUDIENCE ABSTRACT

The performance of a compressor is known to be affected by the ingestion of liquid droplets, and thus, it is a research topic of interest for both academia as well as industry. This work extends the current understanding of the operation of a multistage centrifugal compressor under two-phase flow conditions, by employing high-fidelity computational fluid dynamics (CFD).

In this research, the two-phase flow of refrigerant R134a through a two-stage, in-line centrifugal compressor was analyzed. The CFD model used in this research incorporated real gas behavior of the vapor phase, as well as the interphase heat, mass and momentum transfer processes. An erosion model was also developed and implemented to locate the erosion "hot spots" on the compressor surfaces, and to estimate the amount of material eroded. The effects of increasing the liquid carryover, as well as the influence of droplet size on the compressor performance were assessed.

Liquid carryover altered the flow field within the compressor. As a result, the compressor operated at off-design conditions. The overall effects of liquid carryover were detrimental to the compressor performance. The erosion calculations showed maximum erosion potential on the blade and shroud of the first impeller.

The results from this investigation provided new and useful information that can be used to support improved design solutions.

Acknowledgments

First, I would like to express my sincere gratitude to my advisor, Dr. Walter O'Brien, for his guidance, mentorship, moral support and encouragement throughout my doctoral studies. He has played a vital role in my development as a researcher. I also thank him for giving me the opportunity to work with a talented team of researchers at the VT TurboLab.

I would like to thank the committee members: Drs. Todd Lowe, Danesh Tafti, Brian Vick, William Cousins and Vishnu Sishtla for their technical advice and feedback throughout this research. It has been a pleasure and privilege to work with them.

I would like to acknowledge the financial and technical support of Carrier Corporation and United Technologies Research Center, without which this research would not have been possible.

To my colleagues and friends from the VT TurboLab: Bill Schneck, Dustin Frohnapfel, Tony Ferrar and Justin Bailey, thank you for your friendship and for your support throughout my doctoral studies. Also, to Kedar Halbe and Amey Bapat, thank you for making me feel at home in Blacksburg.

Finally, to my parents: Thank you for your unconditional love and support. I couldn't have come this far without you.

Contents

List of Figures

List of Tables

Nomenclature

β	Relative flow angle
$\dot{Q}_C$	Convective heat transfer rate
$\dot{S}$	Entropy generation rate
$\dot{W}_c$	Compressor power
η_p	Polytropic efficiency
η_{ts}	Total to static adiabatic efficiency
η_{tt}	Total to total adiabatic efficiency
Γ_t	Eddy diffusivity
λ	Thermal conductivity
ω	Angular velocity
$\mathbf{F_D}$	Drag force
$\mathbf{F_R}$	Pseudo force in rotating domain
$\mathbf{r_p}$	Radius vector

$\mathbf{x}_p$ Particle position vector

μ Viscosity

ρ Density

σ Surface tension

θ Angle of the velocity vector measured from the surface

Φ Flux

A Area of cross section

B_T Transfer number

C_D Drag coefficient

c_p Specific heat at constant pressure

COR Coefficient of restitution

d_p Particle diameter

E Energy

H Enthalpy

h Specific enthalpy

h_0 Total specific enthalpy

h_{fg} Enthalpy of vaporization

k Kinetic energy

La	Laplace number
m	Mass
N_s	Number of secondary droplets
Nu	Nusselt number
p	Pressure
p_0	Total pressure
Pr	Prandtl number
Re_p	Particle Reynolds number
S	Particle source term
s	Specific entropy
T	Temperature
t	Time
T_0	Total temperature
U	Velocity
We	Weber number
We_c	Critical Weber number
We_p	Particle Weber number

Chapter 1

Introduction and Literature Review

Two-phase flow - specifically a flow where small amount of liquid is dispersed in the gaseous phase in the form of droplets - is encountered in many turbomachinery applications. Some of the typical examples include gas turbine engines employing wet compression for boosting power or undergoing water wash, steam turbines, chiller compressors etc. This dissertation presents numerical analysis of the operation of a two-stage centrifugal compressor with two-phase flow of refrigerant R134a. The investigations reported in this dissertation extend the understanding of the behavior of the two-phase flow through a centrifugal compressor as well as the implications for the performance of the compressor.

This introductory chapter covers the motivation for this research and the state of the art in the applicable fields. The major objectives of this research are stated next. Lastly, the organization of the dissertation is presented.

1.1 Motivation

The performance of turbomachines is known to be affected by two-phase flow conditions, and thus, it is a research topic of interest for both academia as well as industry. Both thermodynamic and aerodynamic effects of two-phase flow can affect the performance, and hence are needed to be accounted in the analysis of the turbomachine.

In a compressor, the vaporization of liquid reduces the temperature of the surrounding gaseous phase. For a given pressure rise, the major thermodynamic effect of this cooling process is to reduce the compression work. This can be seen from Figure 1.1. In the figure, path $1-2$ depicts a compression process without the intercooling effect, path $1-2_s$ shows an isentropic compression process, and path $1-2^*$ shows a compression process with intercooling. From the figure, it is clear that path $1-2^*$ requires less work as compared to path $1-2$. This implies that the presence of liquid phase can improve the performance of the turbomachine.

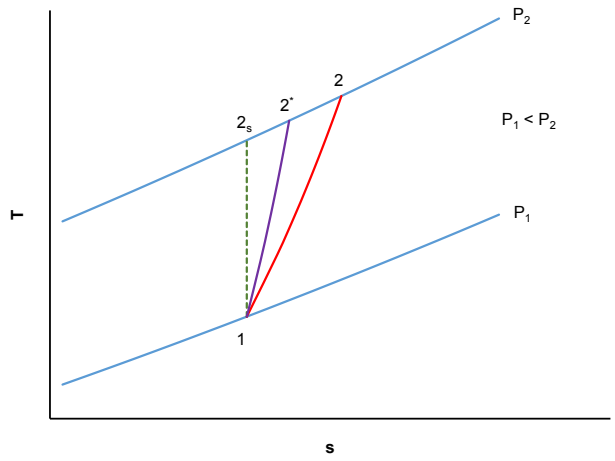

Figure 1.1: T-S diagram for the compression processes

On the other hand, the changes in the flow behavior may result in the compressor operating at an off-design condition, thereby reducing its aerodynamic efficiency. Vaporization of the liquid and

mixing of the two phases also increase the entropy of the system. As a result, the performance of the compressor can be adversely affected.

Thus, the overall effect of two-phase flow can be beneficial or detrimental to the compressor performance. This is governed by the property relations of the working fluid and the variation in its state functions (e.g. enthalpy, entropy) with temperature and pressure, as well as the design and characteristics and the operating conditions of the compressor.

In addition to the effect on the compressor performance, the impact, condensation and agglomeration of liquid droplets on the compressor components can cause pitting, roughening and erosion of the surfaces. Thus, this aspect of two-phase flow is a cause for concern and requires careful consideration.

From the above discussions, it is clear that an in-depth analysis of the flow behavior - including the liquid vaporization process in the compressor stages, and of the droplet dynamics is necessary to fully understand how liquid carryover affects the compressor operation. The motivation of this research is to gain a better understanding of the thermodynamic and aerodynamic effects of the two-phase flow using CFD analysis. This knowledge can then be used to provide guidance for design improvements.

1.2 State of the Art

1.2.1 Effects of Two-Phase Flow

As mentioned in the previous section, two-phase flow through turbomachines has been an active area of research. The topic of wet compression in particular has received great attention, because

it is a simple and cost-effective method of increasing the power output of a gas turbine engine, especially in hot and dry conditions. The basic idea of wet compression is to boost the power output of the gas turbine by leveraging the combined effects of the intercooling process due to water evaporation, and the associated increase in the mass flow rate. Many theoretical, numerical (2D meanline calculations as well as 3D CFD) and experimental studies have been carried out to examine the effect of injecting water droplets on the performance of the gas turbine engines [1–18].

In general, these studies report reduction in the specific work and increase in the total pressure ratio with wet compression. These observations have been attributed to the lower temperature and increased air density during wet compression. The polytropic index of compression has also been reported to be lower as compared to dry compression [14]. A shift in the compressor characteristics and narrowing of the efficiency peak have also been noted [11]. Zheng et al. [14] have proposed three alternate definitions for computing the efficiency of wet compression, namely, (i) Equivalent adiabatic efficiency, which compares the isentropic dry compression work to the work done in the actual wet compression process, (ii) Wet isentropic compression efficiency, which is defined as the ratio of work done in the isentropic and actual wet compression process, and (iii) Efficiency of wet compression, which denotes the deviation of ideal wet compression from the dry compression.

The impingement of liquid droplets on the compressor surfaces is another topic of interest that is closely related to two-phase flow through compressors. Williams and Young [19] have presented a theoretical approach for describing the movement of water deposited on the blade surface. Their research indicates that most of the deposited water is centrifuged towards the blade tip. Numerical investigations by Nikolidis et al. [20] have shown that the droplet impingement occurs mainly on the pressure surface of the rotor blade. Sun et al. [21] have analyzed the droplet-wall interactions by incorporating the theory of spray impingement in their computational model.

It should be noted that the above reported studies involve a two-phase flow of air and water through axial compressors. In the case of centrifugal compressors, 2D meanline calculations by Kang et al. [22] and CFD analysis of a single stage compressor by Surendran and Kim [23] have also shown reduction in the specific work for a given pressure ratio. However, in-depth understanding of two-phase flow through a multistage centrifugal compressor that accounts for the real gas behavior of the vapor phase is still lacking. This work aims to address this issue.

1.2.2 Modeling of Interphase Transfer Terms and Droplet Dynamics

Due to the tight coupling between the two phases, the interphase heat, mass and momentum transfer as well as the droplet dynamics including breakup and droplet-wall interactions play a vital role in governing the behavior of two-phase flow. Therefore, accurate modeling of these processes is necessary for performing a high fidelity CFD analysis. Many models that describe these processes have been developed by studying the spray of gasoline or water droplets. However, since these models are based on non-dimensional parameters such as the particle Reynolds number, Prandtl number and Weber number, they can be potentially applied to the flows involving different liquids.

1.2.2.1 Momentum and Heat Transfer Models

The calculation of interphase momentum transfer involves estimating the drag coefficient C_D, whereas the calculation of interphase heat transfer involves estimating the Nusselt number Nu. Several methods of estimating these parameters have been proposed in literature. These involve theoretical models [24–27], models derived from experimental investigations [28, 29], and numerical analyses [30, 31]. These models have also been compared and reviewed in multiple stud-

ies [32–39]. These reviews can be employed for judging the applicability of the models in numerical simulations.

1.2.2.2 Droplet-Wall Interactions and Erosion Models

The impingement of droplets on a surface is a complex phenomenon that involves a number of factors such as the droplet size, angle and velocity of impact, temperature, viscosity and surface tension of the impinging liquid, as well as the surface roughness and temperature, and liquid film thickness on the surface [40]. A direct numerical simulation of the impact of multiple drops is computationally extremely expensive, and therefore, simplified models that can predict the normal and parallel coefficients of restitution for the impinging droplets, and the number of splashing droplets (if any) are often used in numerical simulations. For example, the gasoline spray impingement model developed by Bai et al. [40, 41] has been used in a numerical simulation of droplet impingement in wet compression [21]. These simplified models are usually semi-empirical, and are based on experimental studies involving a single-drop impact. Several papers that review these droplet impingement models are available in literature [42–46]. These papers point out the special features as well as the possible weaknesses in these models.

Similarly, several models have been proposed to calculate surface erosion. Models such as Finnie [47], Grant and Tabakoff [48], Hamed et al. [49] estimate the surface erosion due to the impact of solid particles. As for predicting the erosion of turbomachinery components due to liquid impact, the main focus has been on steam turbines. Several theoretical and semi-empirical models are available [50–54] for calculating the erosion due to the impact of water droplets on turbines. However, in general, the theoretical models are difficult to implement in numerical simulations due to the associated computational requirements. On the other hand, the semi-empirical models use constants for data fitting and hence are applicable only for that particular combination of

surface material and impacting liquid. Therefore, the validity of these models for computing erosion in the cases involving a different combination of surface material - impacting liquid needs to be assessed.

1.3 Objectives

Although many studies on the operation of turbomachines under two-phase flows are available in literature, in-depth understanding of the operation of a multistage centrifugal compressor in two-phase flow that involves real gas behavior is still lacking. Therefore, the following objectives were set for this research:

1. Develop a high-fidelity CFD model that predicts the operation of a two-stage centrifugal compressor in two-phase flow conditions
2. Understand the droplet dynamics and vaporization, and compare the flow behavior in the compressor under single and two-phase flow conditions
3. Analyze and provide insights on the effects of the two-phase flow on the compressor performance
4. Identify the locations on the compressor surfaces where erosion, if any, is likely to occur and estimate the amount of eroded material
5. Based on the analysis, provide recommendations on the operating conditions in terms of liquid/vapor mass ratio and droplet size

1.4 Organization of the Dissertation

This dissertation is organized into 7 chapters. Chapter 1 covers the introductory material, i.e. the motivation for this research, a review of the current state of the art, the research objectives and expected contributions. Chapter 2 describes the numerical methodology, including an overview of the governing equations as well as the specifics of the modeling techniques that were employed in this research.

The major sources of numerical error are estimated in Chapter 3. This chapter also shows the verification and validation of the modeling techniques that were described in Chapter 2.

Chapters 4, 5 and 6 discuss the results of the two-phase flow analysis. Chapter 4 compares the behavior of the flow through the compressor under single phase and two-phase flow conditions. Chapter 5 presents a detailed analysis of the effects of two-phase flow on the compressor performance. The surfaces likely to show erosion are identified in Chapter 6. The volume of material eroded from these surfaces is also estimated in Chapter 6.

Chapter 7 summarizes the major findings of this research as well as provides recommendations for future work in this field.

Chapter 2

Numerical Methodology

This chapter describes the numerical methodology that was employed for computing the two-phase flow. This includes an overview of the governing equations as well as the specifics of the modeling techniques that were employed in this research.

2.1 Numerical Modeling of Multiphase Flows

In multiphase flow computations, a separate mathematical formulation is required to describe each phase. The choice of the mathematical formulation depends on the type of the multiphase flow as well as the nature of the information sought from the analysis. A detailed description of the above modeling techniques can be found in Multiphase Flow Handbook [37]. Broadly, these modeling techniques are classified as [37]:

1. Eulerian-Eulerian Modeling: In this approach, both the continuous phase as well as the

dispersed phase are solved using Eulerian framework. This implies that the dispersed phase is also solved using an Eulerian transport model.

2. Eulerian-Lagrangian Modeling: In this approach, the continuous phase is solved in the Eulerian framework, whereas the dispersed phase is solved using Lagrangian framework. Individual particles corresponding to the dispersed phase are tracked through the flow field and their interactions with the surrounding fluid and other particles are computed.

3. Particle Distribution Functions: In this approach, particle distribution functions are used to describe the dispersed phase properties.

In this research, the two-phase flow of a single constituent, refrigerant R134a, was solved using a commercial CFD code, ANSYS CFX®, using the Eulerian-Lagrangian framework. The implementation of this model in ANSYS CFX® is described in the next section.

2.2 Eulerian-Lagrangian Approach

In the Eulerian-Lagrangian approach, several individual particles representing the dispersed phase are tracked through the continuous phase. The particles are tracked from the injection point until they escape the computational domain or satisfy other criteria such as minimum size or maximum traveled distance. The continuous phase is solved using the Eulerian framework. To account for the effect of the dispersed phase, mass, energy and momentum source terms (positive or negative) are generated for each tracked particle along the particle track and are balanced in the continuous phase equations. The following section gives an overview of the Eulerian-Lagrangian approach as implemented in ANSYS CFX®. A detailed explanation of this methodology can be found in CFX-Solver Theory Guide [55] and Multiphase Flow Handbook [37].

2.2.1 Continuous Phase

The governing equations for the continuous phase are the Navier-Stokes equations describing the conservation of mass, momentum and energy. These equations, in their discretized form, are solved numerically on a mesh. Typically, the flow associated with turbomachinery applications is turbulent, i.e. it consists of 3D flow fluctuations with respect to both space and time. Theoretically, the governing equations can fully describe a turbulent flow without the need of any additional information through direct numerical simulations (DNS). However, the mesh size required for resolving the turbulence using DNS makes this method prohibitive to be used in most practical applications. This necessitates using turbulence models to account for the effects of turbulence. Development of these turbulence models has been a prime area of research within the field of CFD. These turbulence models range from Large Eddy Simulation (LES), Detached Eddy Simulation (DES) to statistical turbulence models. The statistical turbulence models are computationally less expensive since all scales of the turbulence field are modeled. However, they require the governing equations to be modified such that each instantaneous variable is split into a mean component and a fluctuating component. These modified equations are called Reynolds-Averaged Navier-Stokes (RANS) equations, given by Equations 2.1, 2.2, and 2.3.

2.2.1.1 Continuity Equation

$$\frac{\partial \rho}{\partial t} + \frac{\partial (\rho U_j)}{\partial x_j} = S_{Mass} \tag{2.1}$$

where S_{Mass} is the mass source term due to dispersed phase.

2.2.1.2 Momentum Equation

$$\frac{\partial(\rho U_j)}{\partial t} + \frac{\partial(\rho U_i U_j)}{\partial x_j} = -\frac{\partial p}{\partial x_i} + \frac{\partial(\tau_{ij} - \rho\overline{u_i u_j})}{\partial x_j} + S_{Momentum} \tag{2.2}$$

where $S_{Momentum}$ is the momentum source term due to dispersed phase, τ_{ij} represents the normal and shear components of stress and the term $\rho\overline{u_i u_j}$ represents Reynolds stresses.

2.2.1.3 Energy Equation

$$\frac{\partial(\rho h_0)}{\partial t} + \frac{\partial(\rho U_j h_0)}{\partial x_j} = \frac{\partial}{\partial x_j}(\lambda\frac{\partial T}{\partial x_j} - \rho\overline{u_j h}) + \frac{\partial}{\partial x_j}(U_i(\tau_{ij} - \rho\overline{u_i u_j})) + \frac{\partial p}{\partial t} + S_{Energy} \tag{2.3}$$

In the above equation, S_{Energy} is the energy source term, $\rho\overline{u_j h}$ represents turbulence energy flux, and the term $U_i(\tau_{ij} - \rho\overline{u_i u_j})$ represents viscous work. It should be noted that ANSYS CFX® assumes that the work contribution from the momentum source term $S_{Momentum}$ is negligible.

The total enthalpy in above equation is calculated using Equation 2.4,

$$h_0 = h + \frac{1}{2}U_i U_i + k \tag{2.4}$$

where k is the turbulence kinetic energy given by Equation 2.5.

$$k = \frac{1}{2}\overline{u_i^2} \tag{2.5}$$

2.2.1.4 Equations of State

For closure of the above system of equations, constitutive equations of state for density and enthalpy are needed. These are of the form

$$\rho = \rho(p, T) \tag{2.6}$$

and

$$dh = c_p dT + \frac{\partial h}{\partial p}|_T dp \tag{2.7}$$

where $c_p = c_p(p, T)$

2.2.1.5 Turbulence Model

The Reynolds stresses and the turbulent flux terms in the RANS equations need to be modeled. In this research, the $\kappa - \omega$ based Shear Stress Transport (SST) turbulence model was used. This is an eddy-viscosity based statistical turbulence model. Menter [56] and Bardina et al. [57] have shown that this model performs well in complex flows that involve boundary layer separation as well as simple free-shear flows. Considering the performance of this model, the mesh size required for adequately capturing the compressor geometry (described in the next section) and the computational resources required for solving the multiphase flow, the SST turbulence model is appropriate for this research. This model calculates the Reynolds stresses based on the mean velocity gradients and eddy viscosity using Equation 2.8.

$$-\rho\overline{u_i u_j} = \mu_t\left(\frac{\partial U_i}{\partial x_j} + \frac{\partial U_j}{\partial x_i}\right) - \frac{2}{3}\delta_{ij}\left(\rho\kappa + \mu_t\frac{\partial U_k}{\partial x_k}\right) \tag{2.8}$$

Here μ_t is the eddy viscosity, given by Equation 2.9.

$$\mu_t = \rho\frac{\kappa}{\omega} \tag{2.9}$$

The values of the turbulence kinetic energy κ and turbulence frequency ω are obtained by solving their respective transport equations.

The turbulent flux terms are assumed to be linearly related to the scalar gradient and calculated using Equation 2.10.

$$-\rho\overline{u_i\varphi} = \Gamma_t\frac{\partial \Phi}{\partial x_i} \tag{2.10}$$

Here Γ_t is the eddy diffusivity and is given by Equation 2.11.

$$\Gamma_t = \frac{\mu_t}{Pr_t} \tag{2.11}$$

where Pr_t is the turbulent Prandtl number. For more details of the SST turbulence model, please refer [55] and [56].

2.2.1.6 Effects of the Dispersed Phase on Turbulence

A restriction in ANSYS CFX® is that in the Eulerian-Lagrangian approach, the turbulence model applies only to the continuous phase. Thus, the dispersed phase cannot directly modulate the turbulence.

2.2.2 Dispersed Phase

In the Eulerian-Lagrangian method, particles representing the dispersed phase are tracked through the computational domain. The position of every tracked particle is calculated using forward Euler integration, shown in Equation 2.12.

$$\mathbf{x}_p^n = \mathbf{x}_p^{n-1} + \mathbf{U}_p^{n-1}\,\delta t \tag{2.12}$$

Here δt is a pseudo-timestep, and is calculated using the element dimension, the particle velocity and the desired number of integration steps. The particle velocity is calculated from the particle momentum equation (described in the next section) at the start of every timestep and is assumed to be constant during that timestep.

If the continuous phase and the dispersed phase form a two-way coupled system, the continuous phase can affect the dispersed phase and vice versa. This requires solving the transport equation for the mass, momentum and energy source terms for each tracked particle. The general form of transport equation for these source terms is given by Equation 2.13.

$$\frac{dS_p}{dt} = C_s\,\phi_p + R_s \tag{2.13}$$

where $C_s\ \phi_p$ represents the linear term in the solution variable and R_s is the non-linear term. The mass, momentum and energy source terms are then added to the corresponding continuous phase equations, as described in the previous section.

2.2.3 Particle Number Rate

Tracking of all physically extant particles can be computationally very expensive. Therefore, only a fraction of the physical particles are tracked in the numerical simulation. The tracked particles are assumed to represent the behavior of all physical particles. The number of physical particles characterized by each tracked particle in the simulation is determined from the particle number rate. The mass, momentum and energy source terms corresponding to each tracked particle are multiplied by the particle number rate.

2.2.4 Advantages of the Eulerian-Lagrangian Approach

The Eulerian-Lagrangian approach has some distinct advantages over the other modeling techniques. Some of these advantages are listed below.

1. Since individual particles are tracked through the computational domain, complete information on their behavior is available. This includes the path followed by every representative particle, the variation in temperature and size along the particle path, the location of impact, if any, on the wall boundaries etc.

2. Particle tracking enables implementing the mass, momentum and energy transfer models as desired by the user. In addition, it also allows the incorporation of the particle-wall interactions in the computation.

3. Because individual particles are tracked, this approach is computationally efficient in handling different particle sizes in the same simulation.

2.2.5 Assumptions / Limitations in the Eulerian-Lagrangian Approach

While the Eulerian-Lagrangian approach is deemed appropriate for this research, it is also important to note the assumption and limitations of this approach. Some of the assumptions / limitations are listed below.

1. In this approach, the dispersed phase is assumed to occupy a negligible fraction of volume, as compared to the continuous phase. Thus, this approach is valid only for dilute flows.

2. For the dispersed phase, the density, thermal conductivity, viscosity and specific heat are assumed to be constant.

3. Since the dispersed phase is assumed to have constant thermodynamic properties, a liquid-vapor phase change is supported only when the vapor phase is modeled as an ideal gas. This limitation is imposed so as to maintain the thermodynamic consistency during the phase change process.

4. Although the temperature of a dispersed phase particle can change as it travels in the computational domain, the temperature variation within the particle is neglected, i.e. the entire particle is assumed to be at the same temperature. This assumption is valid when the conduction heat transfer within the particle dominates the convective heat transfer between the particle and the continuous phase.

2.2.6 Consequences of the Assumptions / Limitations in the Eulerian-Lagrangian Approach

It is recognized that the assumptions / limitations in the Eulerian-Lagrangian approach may result in introducing modeling errors in the simulations. The possible consequences of the modeling errors are noted below:

1. The fraction of volume occupied by the dispersed phase particles is not included in the continuous phase calculations. Therefore, if the flow is not dilute, the associated modeling error may result in computing non-physical volume fraction for the dispersed phase.

2. The assumption of constant thermodynamic and transport properties may affect the calculations of the interphase heat, mass and momentum transfer terms. The assumption of constant temperature for the particles will mainly result in erroneous calculation of the interphase heat transfer, and thereby, the interphase mass transfer.

3. Assuming ideal gas behavior for the vapor phase may result in incorrect calculations of properties such as pressure and enthalpy within the computational domain.

4. Turbulence modulation due to the dispersed phase may alter the behavior of the continuous phase. In simulations involving turbomachinery, neglecting this turbulence modulation effect can result in incorrect performance predictions.

Thus, for the Eulerian-Lagrangian approach to be considered valid, it is necessary to ensure that the consequences of the modeling errors in the simulations are negligible. The following sections describe the modeling of the vapor and liquid phase, and discuss the applicability of the Eulerian-Lagrangian approach in this research.

2.3 Modeling of Refrigerant R134a

In this research, a two-phase (liquid-vapor) flow of a single constituent - refrigerant R134a was solved using the Eulerian-Lagrangian approach. Cases with liquid carryover of up to 5% of the vapor mass flow rate were analyzed. The vapor phase was modeled as the continuous phase, whereas the liquid droplets were defined as the dispersed phase. The following subsections describe the modeling of each phase in detail.

2.3.1 Vapor Phase

As mentioned previously, the Eulerian-Lagrangian framework in ANSYS CFX® does not support liquid-vapor phase change when the vapor phase is modeled as a real gas. To overcome this limitation, the vapor phase was defined as an ideal mixture of a real gas and an ideal gas. The ideal gas component of the mixture was assumed to participate in the phase change process. Since the maximum amount of liquid carryover in this research was 5%, the ideal gas component in the gas mixture could not exceed 5%, even assuming the extreme case of complete vaporization of the liquid phase. Therefore, this modeling error was assumed to be negligible.

For the ideal gas component, the specific heat, thermal conductivity and the dynamic viscosity were assumed to be constant. In this research, the expected range of temperature was 280 K - 320 K, therefore these properties were assigned the values corresponding to the average temperature of 300 K.

The real gas component of the vapor phase was modeled by supplying a real gas property table to the solver. This table was generated using NIST REFPROP® [58,59] program and contained the following properties as a function of temperature and pressure: specific enthalpy, speed of sound,

specific volume, specific heats at constant pressure and volume, specific entropy, dynamic viscosity, thermal conductivity and the partial derivative of pressure with respect to specific volume at constant temperature.

2.3.2 Liquid Phase

One of the limitations of the Eulerian-Lagrangian approach is that the properties of the dispersed phase such as density, specific heat, thermal conductivity and dynamic viscosity are assumed to be constant. In this work, these properties were assigned for liquid R134a corresponding to the temperature of 300 K. For the range of temperature (280 K - 320 K) observed in this research, the effects of variations in these properties were assumed to be negligible.

2.4 Applicability of the Eulerian-Lagrangian Approach

Since the Eulerian-Lagrangian approach is valid only for dilute flows, the volume fraction of the liquid phase was calculated to ascertain its applicability in this research. The volume fraction of the liquid phase corresponding to the maximum liquid mass (i.e. 5% liquid carryover) was ~ 6.8×10^{-4}. Therefore, the flow was considered to be dilute [38]. Also, based on this assumption, the droplet-droplet collisions were neglected [60].

Another limitation in the Eulerian-Lagrangian approach is that the temperature variation within each dispersed phase particle is neglected. To judge the validity of this assumption in this research, the Biot number, ($Bi = \frac{Nu\,\lambda_g}{\lambda_p}$) was calculated. Assuming Nusselt number of 2 (typical value for a solid sphere), the Biot number was approximately 0.27. This implies that the assumption of constant droplet temperature can result in a small but non-negligible modeling error.

However, given the small mass fraction of the liquid phase, this modeling error is not expected to affect the overall simulation results significantly.

2.5 Features of Droplet Modeling

As explained in the previous section, the liquid and vapor phase were assumed to to form a two-way coupled system. Therefore accurate modeling of the interactions between the liquid droplets and the vapor phase was necessary. This was achieved by implementing user defined routines for calculating the interphase mass, momentum and energy transfer. A user defined routine was also written to incorporate the droplet-wall interactions . In addition, a secondary droplet breakup model in ANSYS CFX® was utilized to account for the droplet breakup due to aerodynamic deformation. These models are based on correlations that are characterized in terms of dimensionless numbers, and therefore can be assumed to be applicable for a wide number of two-phase gas-liquid flows. The implementation of these models in the numerical simulations is shown schematically in Figure 2.1.

2.5.1 Interphase Momentum Transfer

The motion of the droplets in the computational domain is governed by the net forces acting on the droplets. In general, the forces acting on a particle can be classified as drag force, pseudo forces, Saffman lift force, virtual mass force, pressure gradient force, Basset force, Magnus lift force etc. For the droplet sizes analyzed in this study (100 μm - 400 μm), and considering the density ratio of the liquid phase to vapor phase, only the drag force (F_D) and the pseudo forces (F_R) (viz. centrifugal and Coriolis forces in the rotating frame) have significant effects on the

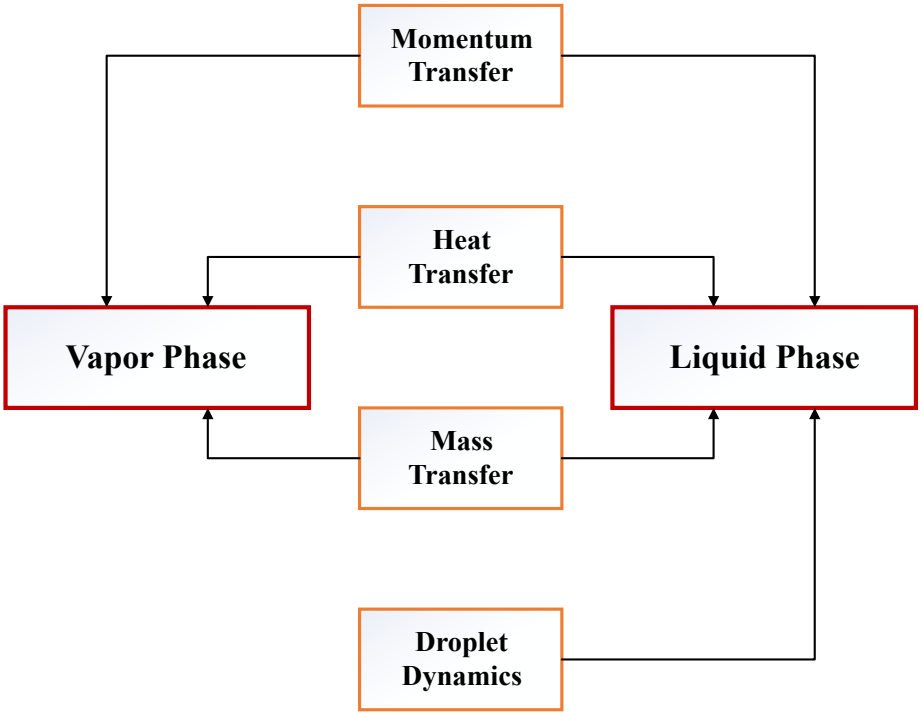

Figure 2.1: Overview of CFD implementation of two-phase flow

droplet motion [8], [61]. Therefore, the equation of motion for a representative droplet can be written using Equation 2.14.

$$m_p \frac{d\mathbf{U}_p}{dt} = \mathbf{F_R} + \mathbf{F_D} \tag{2.14}$$

The pseudo forces can be calculated by using Equation 2.15

$$\mathbf{F_R} = m_p(-2\,\omega \times \mathbf{U_p} - \omega \times \omega \times \mathbf{r_p}) \tag{2.15}$$

where ω is the angular velocity, $\mathbf{U_p}$ is the droplet velocity and $\mathbf{r_p}$ is the radius vector of the droplet.

The drag force is given by Equation 2.16.

$$\mathbf{F_D} = \frac{1}{2} C_D \rho_g A_p \mid \mathbf{U_p} - \mathbf{U_g} \mid (\mathbf{U_p} - \mathbf{U_g}) \tag{2.16}$$

where C_D is the drag coefficient, ρ_g is the vapor phase density, A_p is the effective area of cross section of the droplet. The drag coefficient can be estimated from the empirical correlations [37] which are shown in Table 2.1.

$C_{D0} = \frac{24}{Re_p}$	$Re_p < 0.1$
$C_{D0} = \frac{24}{Re_p}(1 + \frac{3}{16} Re_p)$	$0.1 \leq Re_p < 0.7$
$C_{D0} = \frac{24}{Re_p}(1 + 0.15\, Re_p^{0.687})$	$0.7 \leq Re_p < 1000$
$C_{D0} = 0.44$	$1000 \leq Re_p$

Table 2.1: Correlations for drag coefficient

In the above correlations, the particle Reynolds number Re_p is based on the slip velocity and is given by Equation 2.17.

$$Re_p = \frac{\rho_g \, d_p \mid \mathbf{U_p} - \mathbf{U_g} \mid}{\mu_g} \tag{2.17}$$

It should be noted that the above correlations were derived for the motion of a solid sphere. However, the vaporization of a liquid droplet causes the surrounding gas to flow away from the droplet surface. This is called as Stefan flow, and results in lowering the drag coefficient [37]. Several methods have been proposed [34, 35] that account for this effect through a transfer number, B_T, shown in Equation 2.18.

$$B_T = \frac{c_{p,g}\,(T_g - T_p)}{h_{fg}} \tag{2.18}$$

Sun et al. [32] have compared a number of these methods to experimental results. Based on their investigations, the drag coefficient in this research was calculated using Equation 2.19.

$$C_D = \frac{C_{D0}}{(1 + B_T)^{0.2}} \tag{2.19}$$

The above calculation is valid for a spherical droplet. However, as the droplet travels through the computational domain, it might be subjected to aerodynamic deformation, resulting in a change in the drag coefficient. This can be incorporated in ANSYS CFX® by using the modification proposed by Liu et al. [62], and shown in Equation 2.20.

$$C_{D,p} = C_D\,(1 + 2.632\,y) \tag{2.20}$$

Here y is the measure of droplet distortion, and takes the values between 0 and 1.

Using this value of the drag coefficient, the drag force on the droplet, F_D, was calculated.

Since the pseudo forces do not contribute to the momentum source term in the continuous phase equation, the momentum source term was calculated by using only the drag force, as shown in Equation 2.21.

$$\frac{dS_{Momentum}}{dt} = -F_D \tag{2.21}$$

2.5.1.1 Effects of Turbulence on Droplet Motion

The drag coefficient calculation in the above formulation is based on the mean flow velocity at the location of the droplet. However, instantaneous fluctuations in the flow velocity due to turbulence may cause dispersion of the droplets. The effect of instantaneous fluctuations in flow velocity on the droplet motion can be judged through the Stokes number [37], which is defined as the ratio of the droplet momentum response time τ_p and the characteristic time scale of the flow τ_f (Equation 2.22).

$$St_p = \frac{\tau_p}{\tau_f} \tag{2.22}$$

For a flow through a compressor, the characteristic time scale of the flow can be estimated as $\frac{1}{\omega}$. The droplet momentum response time is given by $\tau_p = \frac{\rho_p d_p^2}{18\mu_g}$. Using these definitions, the Stokes number for a droplet with a diameter of 100 μm comes to 48.93. Thus, the Stokes number is much larger than unity, implying that the effect of instantaneous fluid velocity fluctuation on the droplet motion is likely to be very small. However, the droplet size reduces along its trajectory due to vaporization and / or secondary breakup, and the Stokes number approaches unity as the droplet diameter falls below 14 μm.

2.5.2 Interphase Heat Transfer

The rate of change of droplet temperature can be calculated from the energy balance equation, shown in Equation 2.23.

$$m_p \, c_{p,p} \, \frac{dT_p}{dt} \; = \; \dot{Q}_C \; + \; + \dot{Q}_R \; + \; \frac{dm_p}{dt} \, h_{fg} \tag{2.23}$$

where $\dot{Q}_C$ is the interphase convective heat transfer, $\dot{Q}_R$ is the radiative heat transfer and $\frac{dm_p}{dt} \, h_{fg}$ represents the latent heat transfer associated with vaporizing droplet. In this research, the radiative heat transfer was neglected.

The interphase convective heat transfer is given by Equation 2.24.

$$\dot{Q}_C \; = \; \pi \, d_p \, \lambda_g \, Nu \, (T_g - T_p) \tag{2.24}$$

Thus it is necessary to calculate the Nusselt number for calculating the convective heat transfer. Several correlations have been proposed to estimate the Nusselt number for evaporating droplets [34,35]. These depend on the particle Reynolds number, Prandtl number and the transfer number (defined in the previous subsection). Based on the investigations of Sun et al. [32], the Nusselt number in this research was calculated by using Equation 2.25.

$$Nu \; = \; \frac{2 \; + \; 0.57 \, Re_p^{0.5} \, Pr^{0.33}}{(1 \; + \; B_T)^{0.7}} \tag{2.25}$$

The energy source term in the continuous phase equation depends only on the interphase convective heat transfer, and was calculated by using Equation 2.26.

$$\frac{dS_{Energy}}{dt} \; = \; - \dot{Q}_C \tag{2.26}$$

2.5.3 Interphase Mass Transfer

The interphase mass transfer can occur through two mechanisms: (i) Vaporization, when the droplet temperature is above the boiling point, and (ii) Diffusion, when the droplet temperature is below the boiling point and there is a concentration gradient in the vapor phase. The boiling point can be determined using the Antoine equation. For refrigerant R134a, the Antoine equation is given by Equation 2.27 [63].

$$T_{sat} = 33.06 + \frac{2094}{14.41 - \log_{10}(p_{sat})} \tag{2.27}$$

For a vaporizing droplet, assuming that the droplet temperature remains constant during the vaporization process, the mass transfer rate can be calculated using the energy balance equation, shown in Equation 2.28.

$$\frac{dm_p}{dt} = \frac{-\dot{Q}_C}{h_{fg}} \tag{2.28}$$

The enthalpy of vaporization can be estimated by using Equation 2.29.

$$h_{fg} = (c_{p,g} - c_{p,f})\,(T_{sat} - T_{ref}) + h_{fg,ref} \tag{2.29}$$

The reference temperature was taken as 300 K.

For a two-phase flow of a single constituent, there can be no concentration gradients in the vapor phase. Therefore, when the droplet temperature is below the boiling point, mass transfer through diffusion process cannot occur, and the mass transfer rate is (Equation 2.30)

$$\frac{dm_p}{dt} = 0 \tag{2.30}$$

The mass source term in the continuous phase equation is given by Equation 2.31

$$\frac{dS_{Mass}}{dt} = -\frac{dm_p}{dt} \tag{2.31}$$

2.5.4 Droplet-Wall Interactions

Droplet-wall interactions involve complicated mechanisms that depend on a number of factors such as the droplet size, impact angle and velocity, the liquid viscosity and surface tension, surface and droplet temperatures, surface roughness, and liquid film thickness on the surface [37]. Modeling the droplet-wall interactions is necessary to predict the parallel and normal coefficients of restitution (COR) and the number of secondary droplets produced (if any) due to the droplet breakup after impact. In this research, the spray wall impingement model developed by Bai and Gosman [41] was used.

2.5.4.1 Droplet Impingement Regimes

The user defined routine determines the droplet impingement regime for each tracked droplet. This is based on the droplet Weber number (shown in Equation 2.32), which represents the ratio of the liquid inertia to its surface tension.

$$We_{p,n} = \frac{\rho_p \, d_p \, U_{p,n}^2}{\sigma} \tag{2.32}$$

Here, $U_{p,n}$ is the component of the droplet velocity normal to the surface.

Figure 2.2 shows the droplet behavior corresponding to different impingement regimes. In this research, the walls were assumed to be smooth and adiabatic. Since the heat transfer from the walls to the droplets was neglected, they were treated as wet walls. Accordingly, the relevant regimes of droplet-wall interactions are listed in Table 2.2 [41].

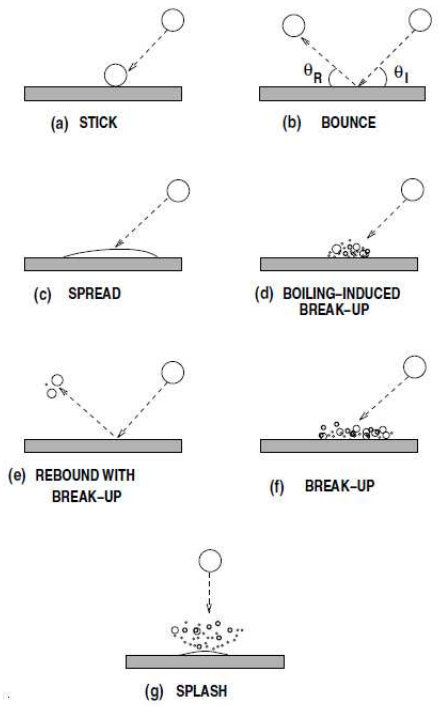

Figure 2.2: Droplet impact regimes [40] [Used as per "fair use" guidelines]

In the above formulation, We_c represents the critical Weber number and is given by Equation 2.33 [41]:

$$We_c = 1320\, La_p^{-0.183} \tag{2.33}$$

Here, La_p is the Laplace number, which represents the ratio of the surface tension to the viscous

Stick	$We_p \leq 2$
Rebound	$2 \leq We_p \leq 20$
Spread	$20 \leq We_p \leq We_c$
Splash	$We_c < We_p$

Table 2.2: Droplet impingement regimes

dissipation within the liquid, and is defined by Equation 2.34.

$$La_p = \frac{\rho_p d_p \sigma}{\mu_p^2} \tag{2.34}$$

2.5.4.2 Droplet Breakup

Secondary droplet breakup occurs only if the droplet impingement results in splashing. Droplet impingement corresponding to the stick, spread or rebound regime does not result in generating smaller secondary droplets. The number of secondary droplets generated by a splashing droplet is given by Equation 2.35 [41]:

$$N_s = [5\,(\frac{We_p}{We_c} - 1)] \tag{2.35}$$

In the numerical simulations, instead of generating and tracking all resulting secondary droplets due to a splashing droplet, a single droplet was tracked. The effects of the droplet breakup were incorporated by adjusting the particle number rate and the size of the tracked droplet.

2.5.4.3 Coefficients of Restitution

The normal and parallel coefficients of restitution were also determined based on the droplet impingement regime, and are listed in Table 2.3. Note that the normal and parallel coefficients of restitution for the stick and spread regimes were specified a small value of 0.1. In the absence of any external forces, both coefficients would be zero, resulting in termination of the droplet tracking. However, a droplet is not likely to remain stationary on a compressor surface due to the action of the aerodynamic, centrifugal and Coriolis forces. Hence specifying the small value of the coefficients of restitution is justified. This assumption implies that the formation of liquid film on the walls was not considered in this research. It can be seen that the normal coefficient of restitution depends only on the angle of impact in the rebound regime, whereas in the splash regime, it depends on the magnitude of relative velocity and the angle of the impinging droplet as well as the secondary droplets [41].

2.5.4.4 Surface Erosion Prediction

Droplet impingement on the compressor surfaces can potentially cause erosion of the surfaces, and thus it is a cause of concern. In this research, the amount of erosion was predicted using the conservation of energy of the impinging droplets. For each droplet, the energy equation can be written as shown in Equation 6.1.

$$(E_{surface} + E_{kinetic})_{droplets\,before\,impingement} = n\,(E_{surface} + E_{kinetic})_{droplets\,after\,impingement} + E_{erosion} + E_{dissipation} \tag{2.36}$$

Stick	$COR_{normal} = 0.1$ $COR_{parallel} = 0.1$
Rebound	$COR_{normal} = 0.993 - 1.76\theta_i + 1.56\,\theta_i^2 - 0.49\theta_i^3$ $COR_{parallel} = \frac{5}{7}$
Spread	$COR_{normal} = 0.1$ $COR_{parallel} = 0.1$
Splash	$COR_{normal} = \frac{v_{s,n}\,\sin\theta_s}{v_i\,\theta_i}$ $COR_{parallel} = \frac{5}{7}$

Table 2.3: Coefficients of restitution

Here n is the number of secondary droplets and $E_{surface} = \sigma\pi d_p^2$

In the droplet impingement model of Bai et al. [41], only the normal component of the droplet velocity is assumed to be involved in the splashing and/or dissipation process. Therefore, the energy required for the erosion process is assumed to be due to the parallel component of the droplet velocity. This assumption is also consistent with the erosion in ductile materials due to solid particles. Since the velocity components are calculated using the coefficients of restitution, the predicted surface erosion depends on the droplet impingement regime.

The volume of the material eroded from the surface can be estimated from the energy of erosion as shown in Equation 2.37 [37]

$$V_{erosion} = \frac{E_{erosion}}{E_{sp}} \tag{2.37}$$

where $E_{sp} \approx 2\sigma_{yield}$ is the surface energy of the material.

It should be noted than the change in compressor geometry due to surface erosion was assumed to be negligible and therefore was not incorporated in the numerical simulations.

2.5.5 Secondary Breakup of Droplets

High droplet slip velocity with respect to the vapor phase can lead to significant deformation of the droplets, leading to secondary droplet breakup [21]. In this research, secondary droplet breakup was calculated by implementing the cascade atomization and breakup (CAB) model in ANSYS CFX®. This model assumes that the droplet distortion can be described by a 1D forced harmonic motion. The droplet breakup regime is determined from the Weber number. The details of CAB model can be found in Tanner [64].

2.6 Computational Model

2.6.1 Compressor Geometry and Description of the Computational Domain

The compressor model that was used in this research is a two-stage in-line centrifugal compressor. This compressor was chosen as a representative of the typical centrifugal compressors used in

chiller units. Figure 2.3 shows the schematic of the compressor geometry. Each stage of the compressor consists of a shrouded impeller and a vaneless diffuser. The two stages are connected by a vaned return channel.

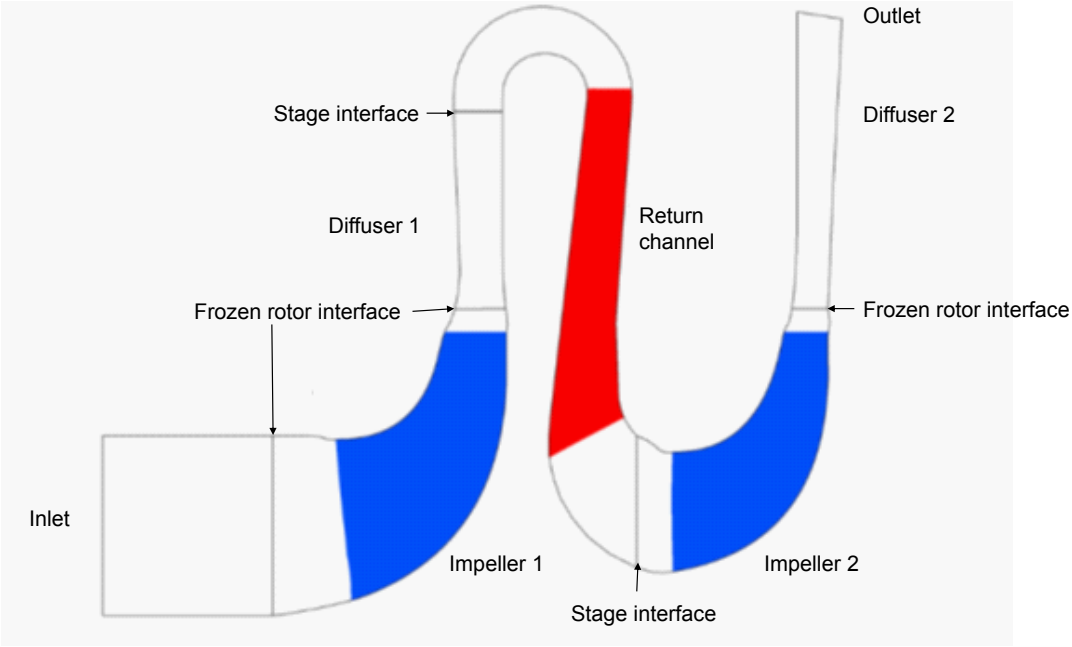

Figure 2.3: Compressor schematic

Taking advantage of the rotational periodicity of the geometry, a single blade passage of both impellers and the return channel, as well as the corresponding regions of the inlet and the diffusers were used to define the computational domain. The interfaces between Inlet - Impeller 1, Impeller 1 - Diffuser 1 and Impeller 2 - Diffuser 2 were defined using “Frozen Rotor” interface. This interface model assumes a fixed relative position for the connected regions and scales the fluxes based on the pitch change. The dispersed phase particles crossing the interface continue their motion from their previous position. The interface between Diffuser 1 - Return Channel and Return Channel - Impeller 2 were defined using “Stage” interface model. This model performs a circumferential averaging of the fluxes through the interface. Thus, this interface model accounts for the time-average interaction effects between the connected regions. Also, unlike the

"Frozen Rotor" interface, the circumferential position of the dispersed phase particles crossing the interface is set randomly.

2.6.2 Computational Grid

The computational domain was discretized with a multi-block structured grid with hexahedral elements, and was generated using ANSYS TurboGrid®. The grid in the impeller and return channel passages was defined using H/J/C/L-Grid topology, while H-Grid topology was used for the inlet and the diffuser regions. In order to improve the orthogonality of the grid elements and the boundary layer resolution around the surfaces of both impellers and the return channel vane, an O-Grid topology was used. Figure 2.4 shows the grid for the first stage of the compressor.

2.6.3 Boundary Conditions

For the vapor phase, the total pressure and total temperature conditions were specified at the inlet such that the corresponding static pressure and temperature represented a 3 K superheat condition for R134a. The flow direction was assumed to be normal to the inlet boundary. The turbulence intensity at the inlet was assumed to be 5 %. The droplet temperature at the inlet was specified to be the same as the saturation temperature. The droplet mass flow rate was calculated based on the amount of liquid carryover, ranging from 1% - 5% of the vapor mass flow rate. In practical situations, the droplets that are carried over in the compressor are non-uniform in size. But since one of the objectives of this research was to assess the effects of the droplet size on the compressor performance, uniform droplet size of 100 μm, 200 μm, 300 μm and 400 μm were specified. The number of tracked droplets varied from 2500 for the 1% liquid carryover cases to 12500 for the 5% liquid carryover cases. This ensured that in all cases, approximately 122,500

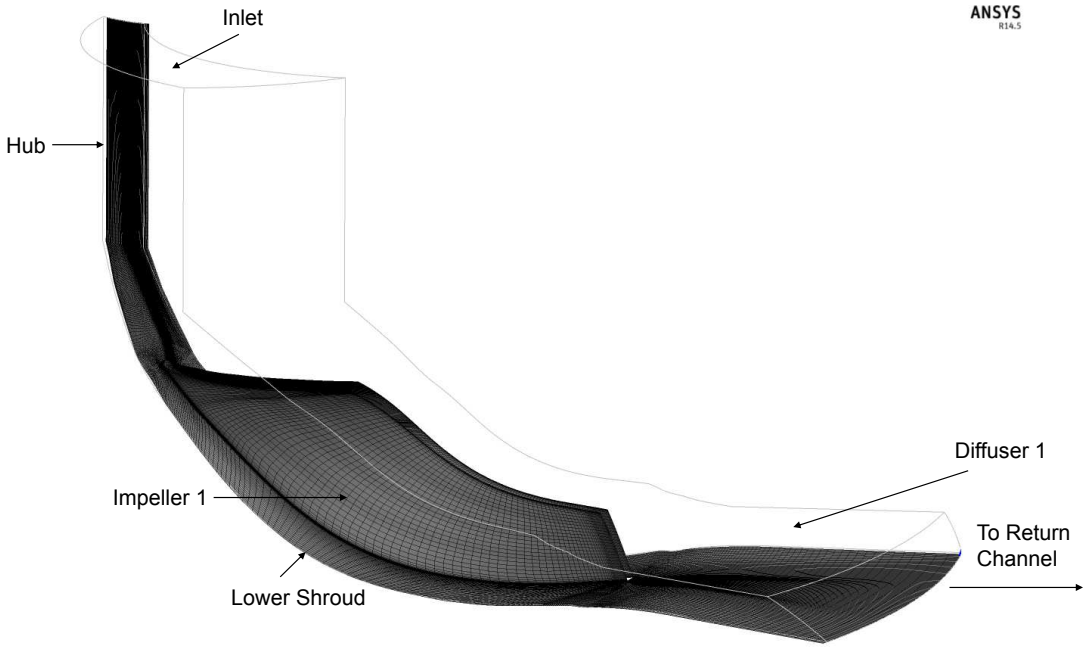

(a) Computational grid for Stage 1

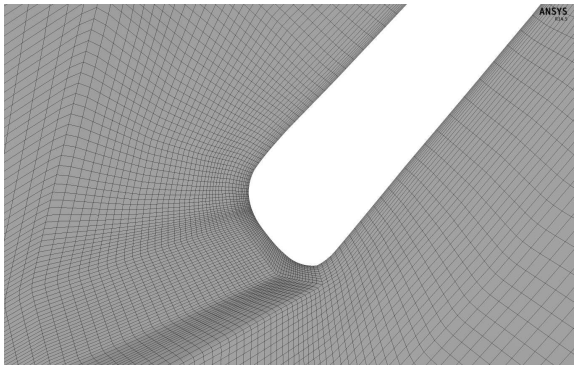

(b) Computational grid near the leading edge of Impeller 1

Figure 2.4: Computational grid

droplets were injected per unit mass of the liquid. This number was determined by considering the following factors: (i) The need to cover the fluid domain by enough droplets, and (ii) The computational resources required to track these droplets. The droplets were injected uniformly at the inlet, assuming zero slip velocity with respect to the vapor phase. The outlet boundary condition was defined by specifying the mass flow rate. Adiabatic and no-slip conditions were assumed at all wall boundaries i.e. the hub, shroud, and the blade surfaces.

2.6.4 Solver Settings

The governing equations were solved using the "High Resolution" scheme in ANSYS CFX® to get a steady-state solution. The "High Resolution" numerical scheme is second order accurate except in the regions of high variable gradients such as shocks. The calculations were performed using double precision. For the two-phase flow simulations, the results of single phase flow case were used as initial guess and the liquid droplets were injected after 40 iterations. This allowed the flow field to develop before starting the droplet tracking process. The droplets were injected and tracked every 10th iteration. For the particle track calculations, 10 integration steps were performed in each element. During each injection, the mass, momentum and energy source terms due to the droplets were calculated. These source terms were applied to the vapor phase equations during the next 10 iterations and were recalculated during the subsequent injection process. Under-relaxation factors were used for the source terms, to avoid divergence of the vapor phase equations. The under-relaxation factor for the momentum source term was kept at 0.75, whereas the under-relaxation factors for the mass and energy source terms were kept at 0.5. The source terms to the vapor phase equations were calculated by the solver using Equation 2.38.

$$S_F = (1 - U_F)\, S_F + U_F S_P \tag{2.38}$$

where S_F represents the source term applied to the vapor phase equations, S_P represents the droplet source terms and U_F is the under-relaxation factor.

Chapter 3

Verification and Validation

An important step in assessing the accuracy of a numerical simulation is quantifying the uncertainties associated with the simulation. In this chapter, the major sources of numerical error are estimated. The verification and validation of the user defined routines that were used in this research is also presented.

3.1 Grid Independence Study

The main sources of error in a numerical simulation are: (i) round-off error, (ii) iterative error, and (iii) discretization error (DE). The round-off error can be minimized by using double precision numerics, and the iterative error can be controlled through the convergence criteria. However, the contribution from the discretization error is usually the largest and hence needs to be quantified [39].

In this research, Generalized Richardson Extrapolation method was used to estimate the discretization errors. The details of this method can be found in Oberkampf and Roy [39]. Following this method, single phase flow simulations were performed on three grid sizes (i) Fine grid (6,909,160 elements), (ii) Medium grid (3,109,680 elements), and (iii) Coarse grid (1,358,976 elements). Note that the grid sizes differ by a factor of ~ 1.3^3, which is a recommended value for the Generalized Richardson Extrapolation method. The change in total specific enthalpy and the total to static and total to total pressure ratio were chosen as the variables of interest. Extrapolated solutions were computed for these variables following the Generalized Richardson Extrapolation method. The discretization errors were estimated by comparing the solution on each grid with the extrapolated solution. Table 3.1 shows the percent discretization error for the three variables on the three grids.

Grid	**% DE in $\triangle h_0$**	**% DE in total-to-static pressure ratio**	**% DE in total-to-total pressure ratio**
Fine	0.1299	0.0149	0.0584
Medium	0.4070	0.1739	0.3541
Coarse	1.2768	2.0340	2.1554

Table 3.1: Discretization errors and uncertainties

The estimated discretization errors on the Medium and the Fine grid were less than 0.5 %. Considering the complexity of the geometry, and the errors involved in the scaling and averaging of the

flow field to account for the rotating and stationary domains, these estimated discretization errors were considered to be within reasonable limits. The Medium grid was deemed to provide a good balance between accuracy and computational costs and was used to carry out all simulations in this research.

3.2 Particle Number Independence Study

In the Eulerian-Lagrangian method, only a fraction of the physical particles are tracked. The tracked particles are assumed to characterize the behavior of all physical particles. Therefore, it is necessary to track a sufficient number of particles such that the above assumption can be considered to be valid and the simulation results are independent of the number of tracked particles.. The mass, momentum and energy source terms due to each tracked particle are multiplied by the particle number rate. Thus, if the number of tracked particles is too small, i.e. if the particle number rate is too high, the source terms to the continuous phase equations will be large, resulting in divergence of the simulation. Therefore, the appropriate number of particles to be tracked in the simulation needs to be determined through a particle number independence study.

The particle number independence study in this research was performed for the case of 1% liquid carryover and initial droplet size of 100 μm. Five simulations were run by varying the number of tracked droplets from 1250 to 5000. The change in total specific enthalpy, total to static and total to total pressure ratio were chosen as the variables of interest. The solutions corresponding to particle numbers of 1250, 2000, 2500 and 3250 were compared with the solution using 5000 particles. The percent difference in the chosen variables is shown in Table 3.2.

It can be seen that for all four particle numbers, the differences in the chosen variables were less than 0.03%. Based on this observation, 2500 droplets were tracked for the 1% liquid carryover

Number of tracked droplets	**% Difference in** $\triangle h_0$	**% Difference in total-to-static pressure ratio**	**% Difference in total-to-total pressure ratio**
1250	-0.0029	0.0176	0.0184
2000	-0.0159	0.0270	0.0278
2500	-0.0095	0.0192	0.0200
3250	-0.0132	0.0242	0.0258

Table 3.2: Particle number sensitivity

case, resulting in 122,500 droplets per unit mass of the liquid. To keep the particle rate constant, the number of tracked droplets was increased in proportion with the liquid carryover. Table 3.3 shows the number of tracked droplets for all cases in this research.

3.3 Verification and Validation of Droplet Modeling

As discussed in Chapter 2, user routines were implemented to calculate the interphase mass, momentum, and energy source terms and the droplet-wall interactions. Since empirical correlations were used in the momentum, energy, and droplet-wall interactions routines, it is necessary to verify and validate their implementation in the numerical simulation. In this research, the verification and validation of these routines was performed by comparing the results of numer-

Liquid carryover	Number of tracked droplets
1 %	2500
2 %	5000
3 %	7500
4 %	10000
5 %	12500

Table 3.3: Number of tracked droplets in the simulations

ical simulations with experimental data reported in literature. This process is presented in this section.

3.3.1 Verification and Validation of Interphase Momentum Transfer

The implementation of the interphase momentum transfer user routine was validated by using the experimental investigations of Bai et al. [65]. The experiment involved studying the interaction of sprayed water droplets with air flowing through a rectangular duct. The dimensions of the duct were $0.095\,m \times 0.095\,m \times 1\,m$. The schematic of the computational model used in the validation study is shown in Figure 3.1. In the simulation, uniform velocity of 7 m/s and total temperature of 293 K was specified at the inlet boundary. Average static pressure of 1 atm was imposed at the outlet boundary. Water was sprayed through two nozzles, located 0.1 m downstream of the duct inlet as shown in Figure 3.1. Each spray was directed normal to the direction of air flow. Water

mass flow rate at each location was specified as 0.0659 kg/s. The droplet injection velocity was estimated based on the operating pressure on the nozzle. The spray angle, water temperature and average droplet diameter were 80^0, 293 K and 100 μm respectively. Additional details about the experiment can be found in [65].

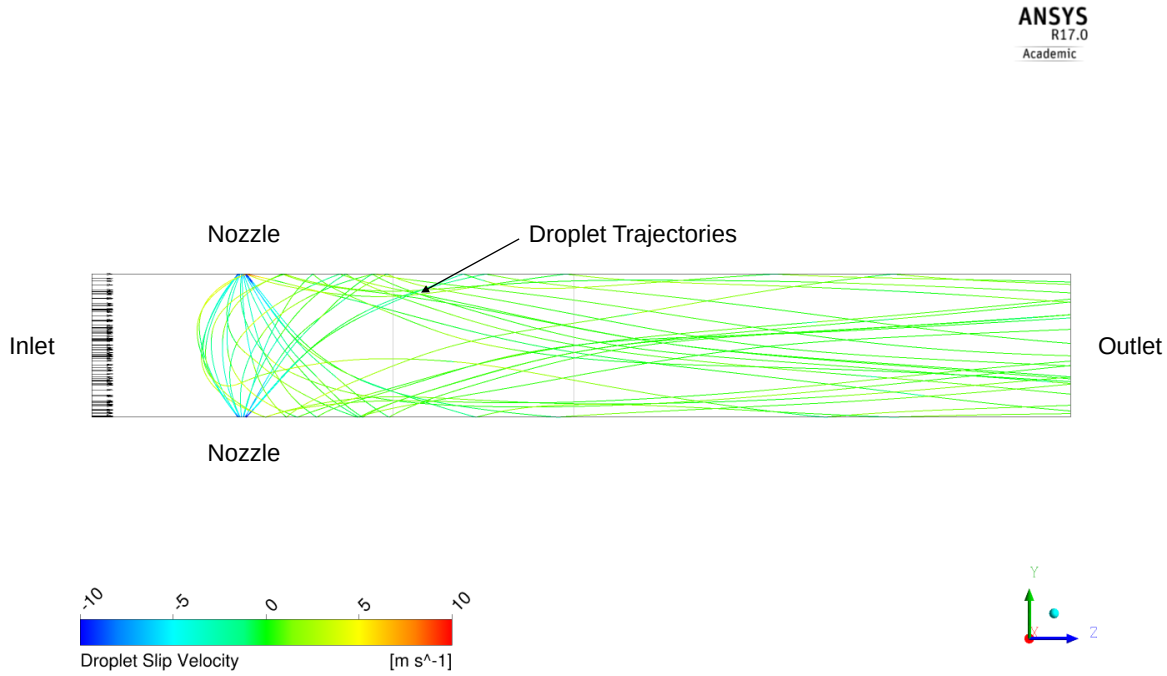

Figure 3.1: Computational model for verification and validation of interphase momentum transfer

Figure 3.1 also shows the trajectories of a sample number of water droplets. It can be seen that in the vicinity of the nozzles, the droplets do not immediately follow the air flow, and their motion is dominated by the direction in which they are sprayed. However, as they move along the duct, the droplet slip velocity is seen to approach zero, indicating that the droplets are following the air flow.

The flow structure resulting from the momentum transfer between the air flow and the water spray is shown in Figure 3.2. The figure qualitatively compares the flow streamlines at duct cross sections located 100 mm and 220 mm downstream of the nozzles, as observed from the

experiment [66] and as calculated from the computational simulation. In both cases, two pairs of counter-rotating vortices are observed.

A quantitative comparison between the numerical simulation (indicated in blue) and the experiment can be seen in Figure 3.3 which shows the maximum vorticity along the duct. As expected, the maximum vorticity is seen to decrease along the duct. The error in the simulation results is also seen to increase along the duct. The average $L2$ Norm for the error is 39.94 s^{-1},which is approximately 11 % of the average value of the vorticity. Considering the uncertainty in the droplet injection velocity, this error is within reasonable limits. Since the overall effects on the surrounding gas due to the droplets as predicted by the numerical simulations match reasonably well with the experimental results, the modeling of the interphase momentum transfer through the user routine was deemed to be acceptable.

3.3.2 Verification and Validation of Interphase Heat Transfer

The experimental investigations carried out by Sun et al. [32] were used to validate the implementation of the interphase heat transfer user routine. The experiment involved studying the heat transfer between air and acetone droplets. The experimental setup was similar to the one used by Bai et al. [65], as reported in the previous section. However, only one nozzle was used to spray acetone droplets. In the simulation, the air inlet velocity and total temperature were specified as 30 m/s and 673 K respectively. At the outlet, average static pressure of 1 atm was imposed. The temperature and Sauter diameter of acetone droplets at the nozzle were 284 K and 48 μm respectively. The mass flow rate and injection velocity were estimated from the operating pressure on the nozzle. Figure 3.4 shows the computational model and the tracks for a sample number of acetone droplets.

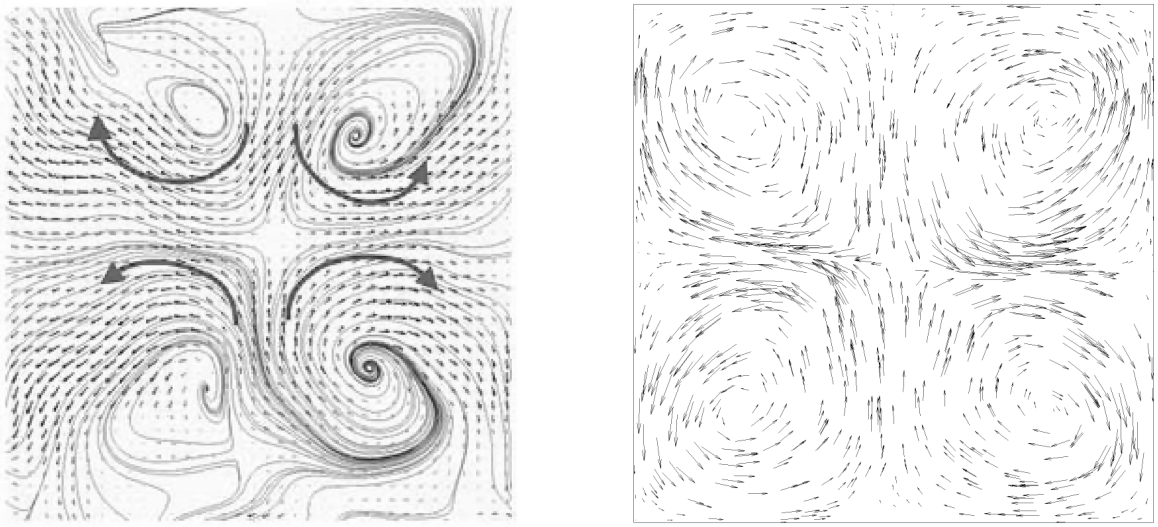

Experimental results Numerical results

(a)

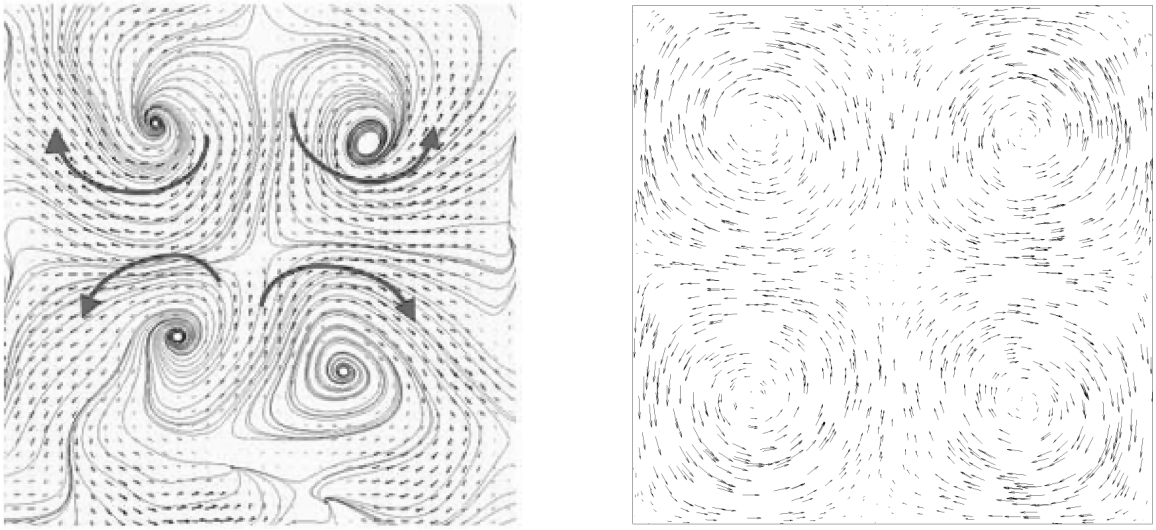

Experimental results Numerical results

(b)

Figure 3.2: Comparison of flow streamlines at (a) 100 mm downstream of the nozzles (b) 220 mm downstream of the nozzles [66] [Used as per “fair use” guidelines]

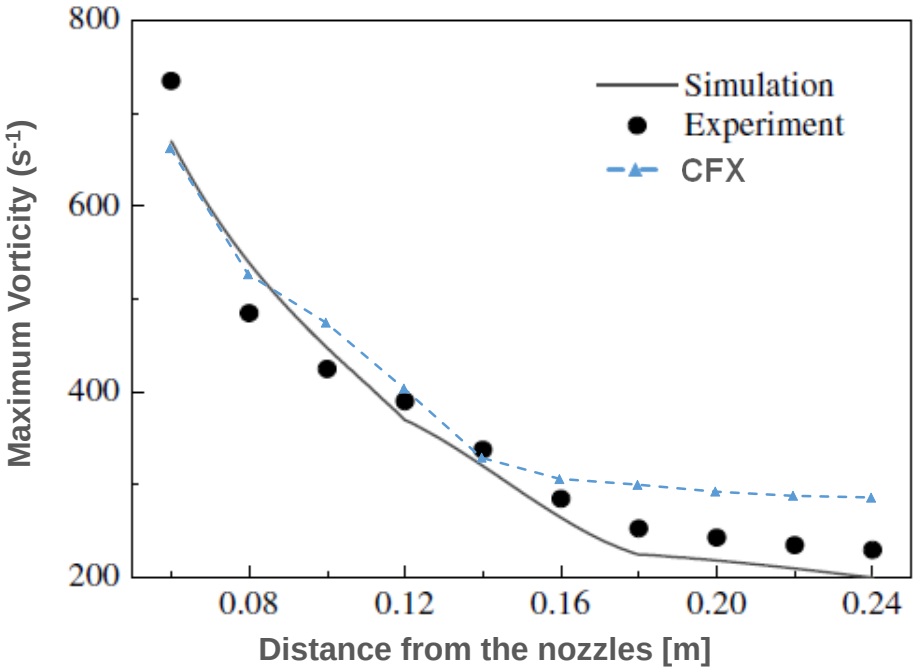

Figure 3.3: Comparison of vorticity along the duct [66] [Used as per "fair use" guidelines]

Due to the interphase heat transfer from the air to the cooler acetone droplets, the air temperature decreases along the duct. This was measured along the central vertical line at four locations along the duct, at a distance of 0.2 m, 0.3 m, 0.4 m and 0.5 m from the nozzle. The measurement locations are shown in Figure 3.4. The drop in air temperature from the inlet static temperature was computed in the numerical simulation (indicated in blue) and was compared with the results reported by Sun et al. [32].

From Figure 3.5, the simulation results and the experiments show similar trends in temperature drop. The maximum temperature drop is seen to occur at a distance of 0.2 m from the nozzle and it is seen to decrease along the duct. At all locations, the results from numerical simulations differ from the experimental results in the region near the center of the duct. The average $L2$ Norm for the error at location 1, location 2, location 3 and location 4 are 4.042 K, 3.646 K, 4.205 K and 3.863 K respectively, or 28.835%, 25.028%, 30.011% and 28.709% of the average temperature at the cor-

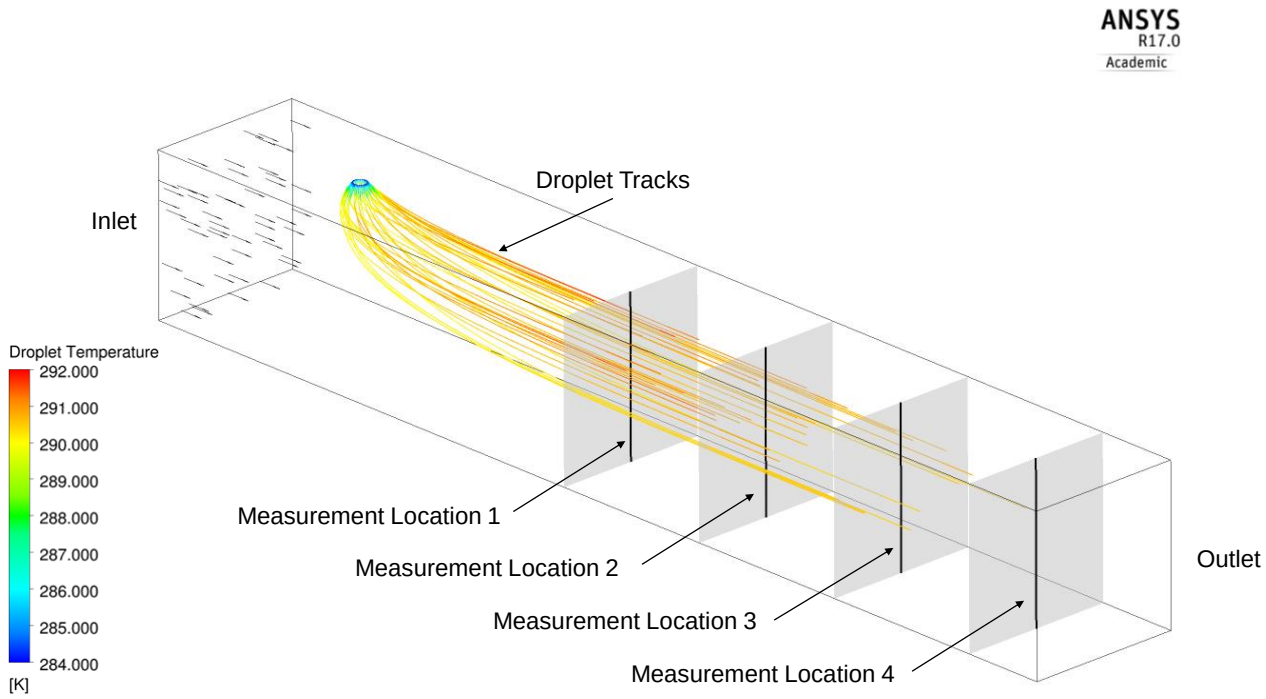

Figure 3.4: Computational model for verification and validation of interphase heat transfer

responding location. It should be noted the Biot number for acetone is 0.31. This implies that the assumption of uniform droplet temperature can result in a modeling error. However, accounting for the temperature distribution within the droplets in the simulations is not supported in the current CFD model. The uncertainties in the droplet mass flow rate and injection velocity also contribute to the numerical error. However, Figure 3.5 shows that the error is limited to a small region. Therefore, overall modeling of the interphase heat transfer through the user routine was considered to be acceptable.

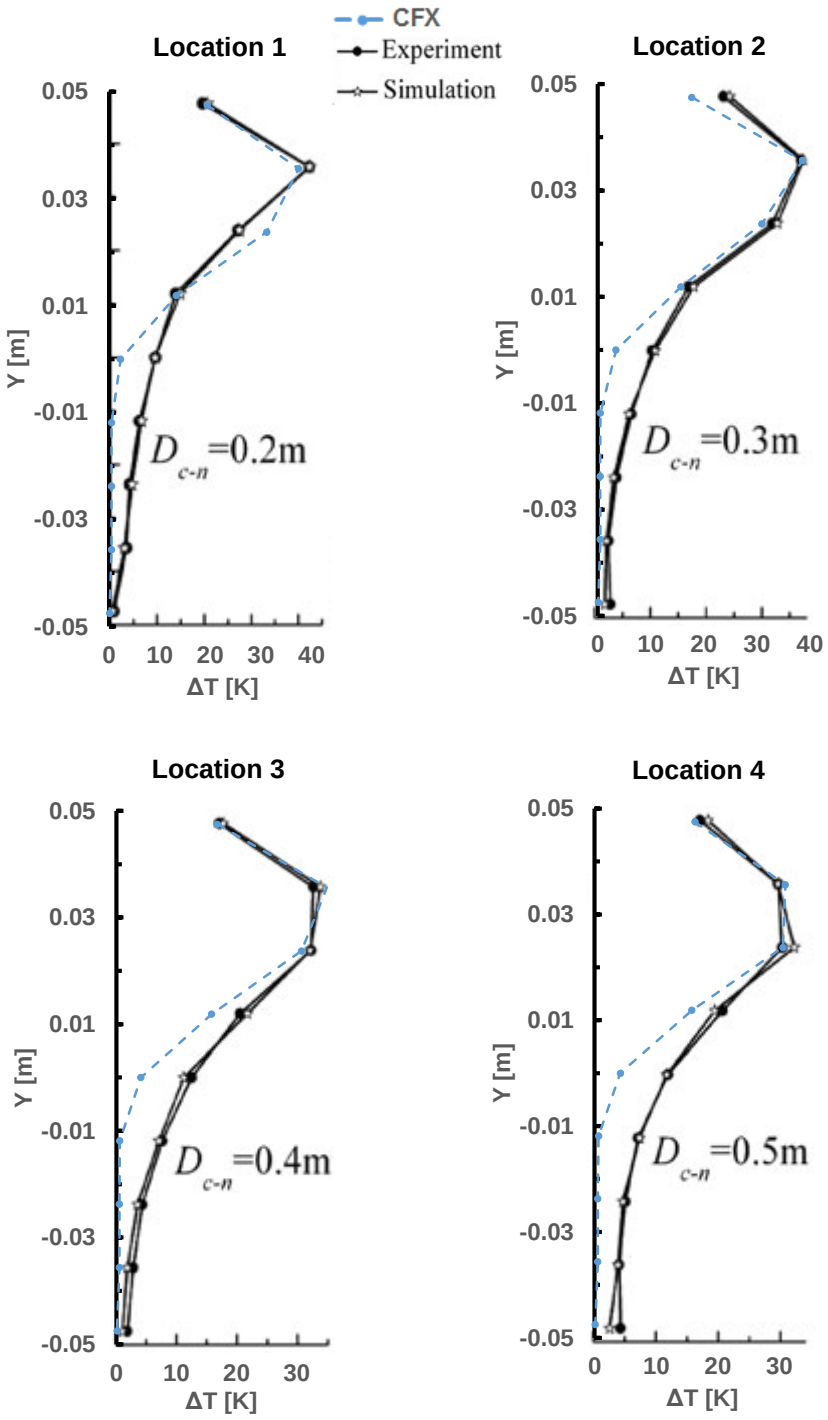

Figure 3.5: Comparison of calculated temperature drop [32] [Used as per “fair use” guidelines]

3.3.3 Verification and Validation of the Modeling of Droplet-Wall Interactions

As described in the previous chapter, the normal and parallel coefficients of restitution and the droplet breakup factor were calculated in the simulations by implementing a droplet-wall interactions user routine. The verification and validation of the user routine is presented below.

3.3.3.1 Calculation of Coefficients of Restitution and Droplet Breakup Factor

In the droplet-wall interactions model, the coefficients of restitution and the droplet breakup factor are defined based on the droplet impingement regime. Thus, the implementation of the user routine can be verified by simulating test cases in which the droplet injection velocity is specified so as to result in a predetermined impingement regime. The coefficients of restitution and the droplet breakup factor can then be calculated from the simulations and compared with the predetermined impingement regime.

Following this methodology, four simulations were run, corresponding to the four impingement regimes viz. stick, rebound, spread or splash. Figure 3.6 shows the normal and parallel coefficients of restitution for the four cases as a function of the droplet normal velocity. The normal velocities corresponding to a change in the impingement regime are also shown in the figure. It can be seen that the user routine calculates the coefficients of restitution in accordance with the impingement regime.

The numerical simulations predicted a droplet breakup factor of 1 for the stick, rebound, and spread regimes. For the splash regime, the predicted breakup factor was 3, which matches with the calculations based on Equation 2.35 in Chapter 2. These results show that the user routine

was correctly implemented in the numerical simulations.

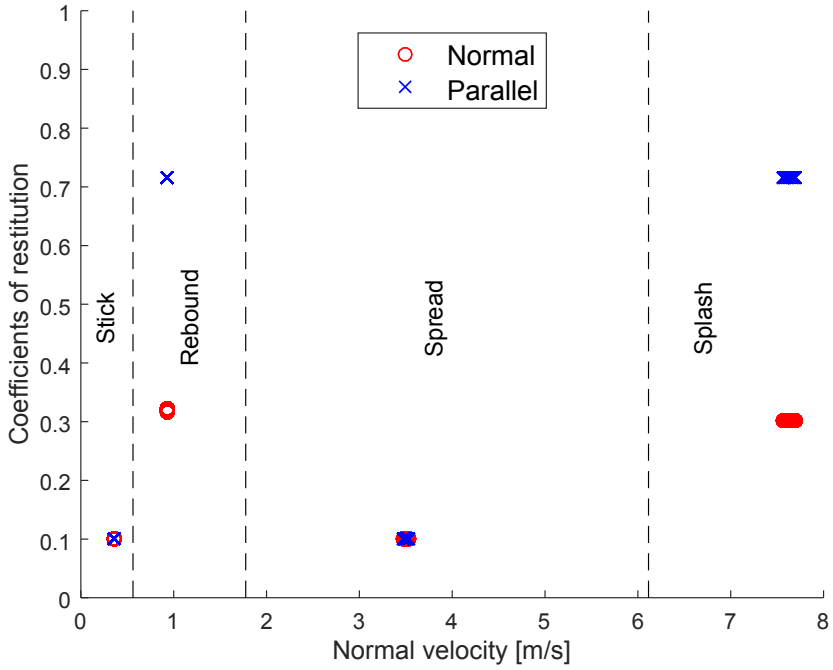

Figure 3.6: Coefficients of restitution from numerical simulation

3.3.3.2 Experimental Validation

The results reported in Bai et al. [41] were used to validate the implementation of the droplet-wall interactions user routine. In the experiments, gasoline spray was injected in a rectangular wind tunnel with cross section of ($32\,mm \times 172\,mm$), at an angle of 20^0 to the vertical direction. At the nozzle, the droplet diameter distribution was assumed to be normal, with a mean of 125 μm and standard deviation of 10 μm. The air inlet velocity and total temperature were specified as 15 m/s and 293 K respectively. The outlet boundary was maintained at an average static pressure of 1 atm. A measurement volume with dimensions of ($20\,mm \times 2\,mm \times 4\,mm$) was defined such that the centroid of the measurement volume was at a distance of 12 mm from the nozzle and 5 mm from the bottom surface. The computational model is shown in Figure 3.7, along with sample

droplet tracks.

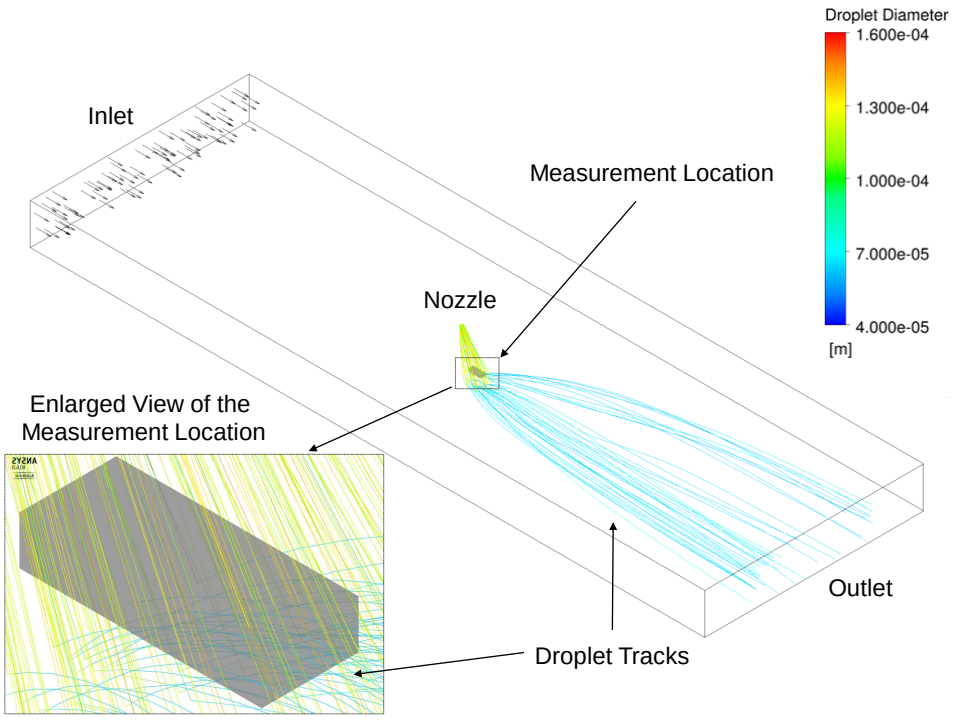

Figure 3.7: Setup for Verification of droplet-wall interactions

Figure 3.8 compares the droplet size distribution obtained from the numerical simulations (indicated in blue) with the results reported in Bai et al. [41]. The size distribution was calculated by ensemble-averaging the diameters over a period of 100 ms. Following the measurements reported in [41], only upward-moving droplets (i.e. droplets moving away from the bottom surface after impingement) were considered in the calculation.

It can be seen that the droplet size distribution from numerical simulation shows similar trend to the experimental results reported in [41]. In the experimental investigations, droplets with diameters of 50 μm or less were detected within the measurement volume. However, the numerical simulations predicted a negligible number of droplets with diameters less than 50 μm . Thus, the probability distribution function in this region is observed to be shifted slightly to the right. From experimental results, the peak of the distribution function appears to occur at droplet diameter

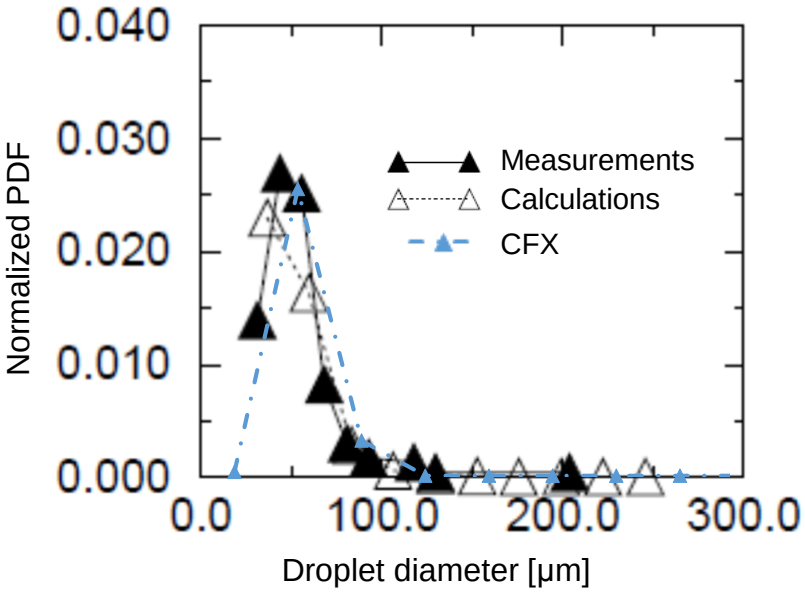

Figure 3.8: Comparison of droplet size distributions [41] [Used as per "fair use" guidelines]

of approximately 40 μm , whereas the numerical simulation predicts the peak to occur at approximately 60 μm . It should be noted that in the numerical simulations, the surfaces were assumed to be perfectly smooth. Also, even though droplet-droplet collisions (which can result in coalescence or breakup of colliding droplets) were neglected in the numerical simulations, they might be relevant for spray impingement [46]. Considering these factors, and the overall reasonable agreement between the simulation and the experimental results, the modeling of droplet-wall interactions through the user defined routine was deemed to be acceptable.

Chapter 4

Two-Phase Flow Behavior Through the Compressor

Following the methodology described in Chapter 2, the two-phase flow of refrigerant R134a through a two-stage in-line centrifugal compressor was analyzed. The two-phase flow cases that were analyzed correspond to liquid carryover at the compressor inlet ranging from 1% to 5% of the vapor mass flow rate, and droplet diameters varying from 100 μm to 400 μm. This chapter compares the flow behavior in the single phase (i.e. vapor only) case and the two-phase flow cases. The details of the droplet dynamics and vaporization within the compressor are also presented.

The schematic of the compressor geometry that was used in the above computational analysis is shown in Figure 4.1. The analysis was performed by dividing the compressor geometry into four components, viz. i) Inlet, ii) Stage 1 (i.e. Impeller 1 and Diffuser 1), iii) Return Channel, and iv) Stage 2 (i.e. Impeller 2 and Diffuser 2), as shown in the figure.

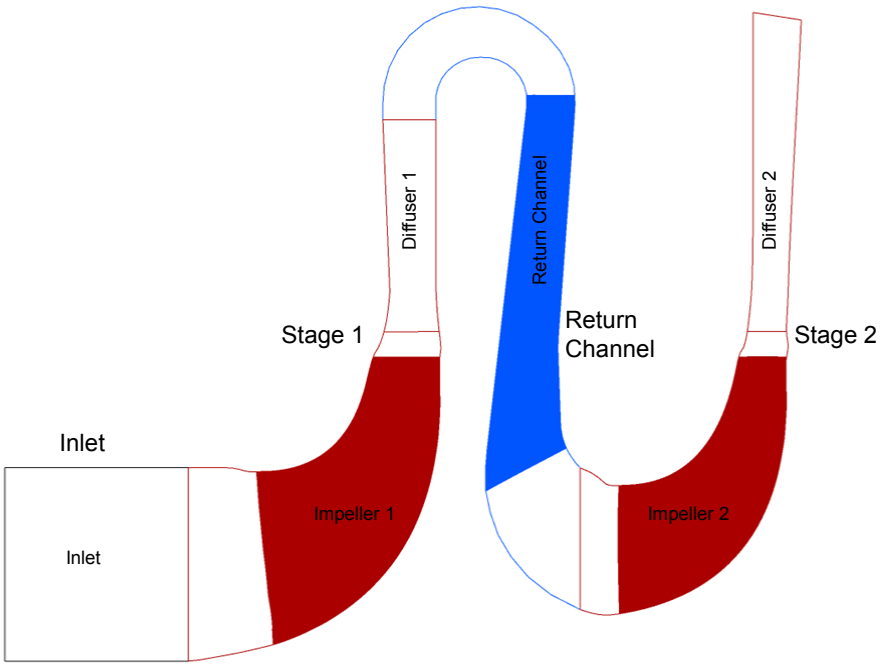

Figure 4.1: Compressor schematic

4.1 Droplet Dynamics

Tracking a representative number of droplets can provide information about how the droplets are transported within the compressor. This can be used to understand the droplet vaporization as well as the two-phase flow behavior in the compressor. This section covers the droplet dynamics in the compressor geometry, including the tracing of the droplet tracks and the changes in the droplet size due to vaporization and / or secondary breakup.

4.1.1 Droplet Tracks

Figure 4.2 shows the droplet tracks for four cases, corresponding to 5% liquid carryover and initial droplet diameter of 100 μm, 200 μm, 300 μm and 400 μm. These tracks are shown on the meridional

plane for better visualization. In the plots, the color of each droplet track corresponds to the size of the droplet normalized by the initial droplet size for that case. Thus, a change in the droplet track color indicates a relative change in the droplet size due to vaporization and / or breakup. The termination of the track indicates that the droplet size has fallen below the tracking criterion, which was set at $10^{-8}\ \mu m$.

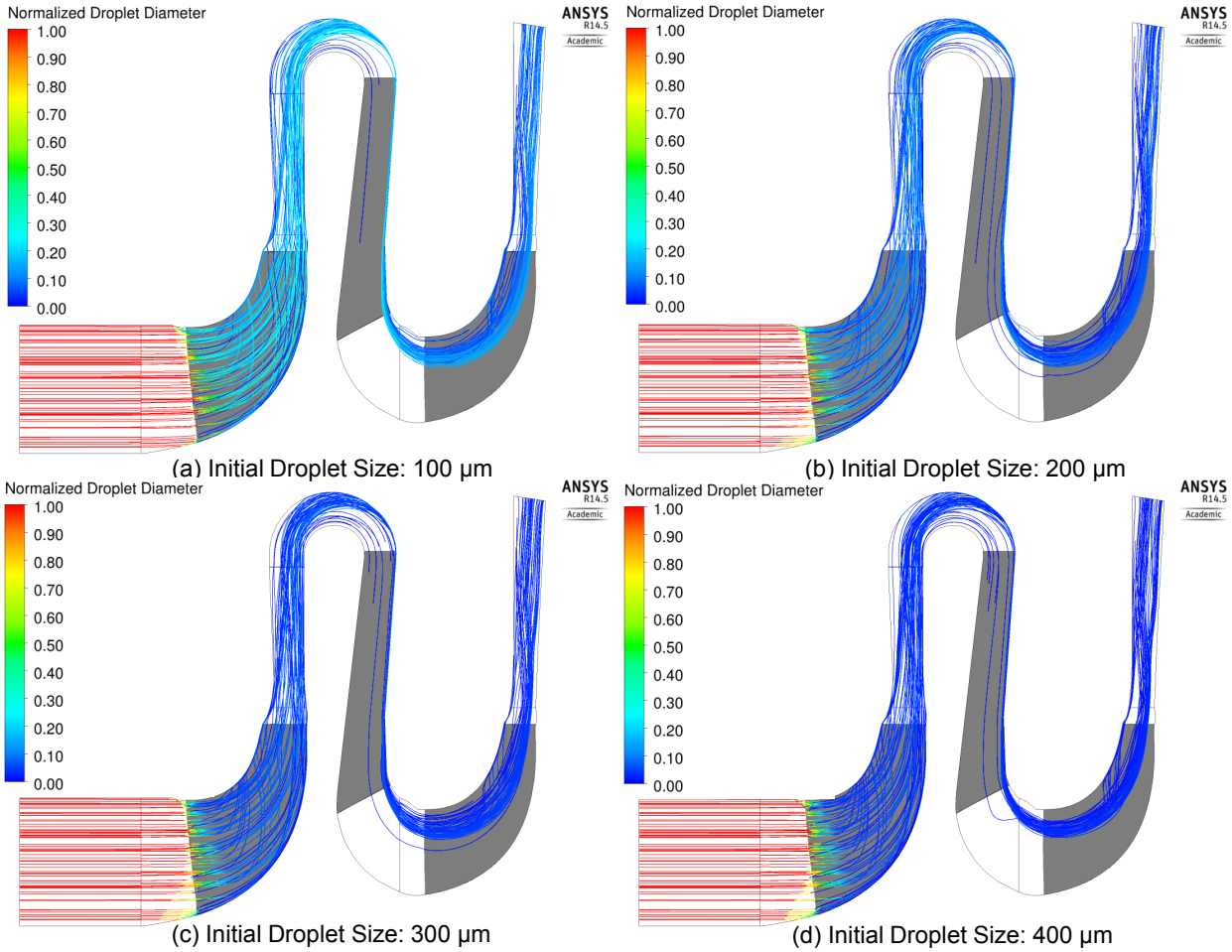

Figure 4.2: Comparison of the droplet tracks with increasing initial droplet size

The droplets can be seen to enter through the inlet boundary and continue their motion through the Inlet domain, without any significant change in size. This indicates that the droplet vaporization and / or breakup in the Inlet domain is negligible. This is expected, because the droplets were injected with zero slip velocity with respect to the vapor phase, resulting in small Reynolds,

Nusselt and Weber numbers. As noted in Chapter 2, these numbers play a significant role in the vaporization and breakup processes, and small values of these numbers will likely result in a small rate of vaporization.

As the flow accelerates near Impeller 1, the droplet size is observed to reduce, predominantly near the leading edge. This indicates that significant droplet vaporization and / or breakup occurs in this region. With increasing initial droplet size, this change in droplet size is seen to be more rapid. The droplet tracks also show that within the Impeller 1 domain, most of the droplets follow the main flow path within the blade passage, however some droplets are centrifuged towards the shroud.

As the droplets enter the Return Channel domain, most droplets are shown to impinge on the Return Channel shroud surface as they navigate the bend. After the impingement, these droplets continue their motion along the shroud. As a result, almost all droplets tracks are located in the region near the shroud as they enter Impeller 2. Similar to Impeller 1, most droplets are seen to follow the main flow path, while a few droplets are centrifuged towards the shroud. In all four cases, the droplet tracks are observed to continue till the outlet, indicating that the liquid phase is not completely vaporized within the compressor.

4.1.2 Droplet Dynamics in Impeller 1

Further investigations were carried out in the region near Impeller 1 to understand the droplet dynamics in that region. Figure 4.3 shows the droplet tracks for the 5% liquid carryover case and initial droplet size of 400 μm, from the blade pressure surface side. The limiting streamlines on the impeller blade surface are also shown in the figure. A large number of droplets are seen to impinge and rebound / break up near the leading edge. This is due to the relatively large angle of

impact, resulting in relatively large normal velocities. The droplets that are away from the blade surface or rebounding from the surface are observed to follow the main flow path within the blade passage. However, smaller droplets that are closer to the blade pressure surface follow the surface streamlines and are centrifuged towards the shroud. The blade suction surface shows negligible droplet impingement and the droplets on the side of the suction surface are seen to follow the main flow path. Similar flow features are observed for cases with smaller initial droplet sizes and lower amounts of liquid carryover.

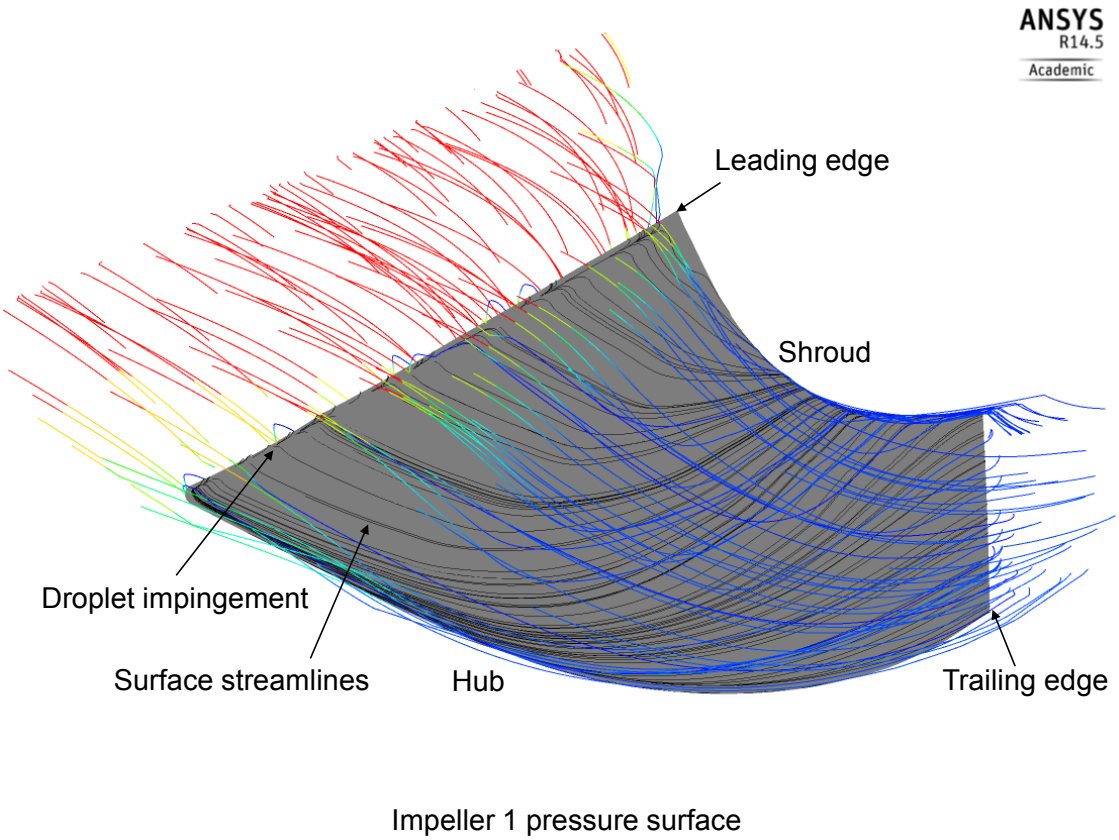

Figure 4.3: Droplet dynamics in impeller 1 domain

4.2 Droplet Vaporization

This section covers the details of the droplet vaporization process within the compressor. This includes identifying the locations where droplet vaporization occurs as well as the role played by the droplet size on the rate of vaporization.

4.2.1 Droplet Vaporization Along the Streamwise Location

The total liquid mass flow rate (normalized by the vapor mass flow rate) through the cross-sections along the streamwise direction was calculated and is plotted in Figure 4.4. In the figure, location 0 - 1 corresponds to the Inlet, 1 - 2 corresponds to Impeller 1, and so on. The figure shows all two-phase flow cases, i.e. liquid carryover ranging from 1% - 5% and initial droplet size varying from 100 μm - 400 μm.

The figure shows that the rate of droplet vaporization varies considerably along the streamwise location. This implies that the assumption of constant vaporization along the streamwise direction that is often used in wet compression analysis is not valid in this case. Negligible vaporization occurs in the Inlet domain, as noted previously. The liquid is seen to vaporize rapidly in the latter half of the Impeller 1 blade passage. The mass of liquid vaporized in this region shows increase from ~ 0.03% for the 1% carryover cases to ~ 0.1% for the 5% carryover cases. The rate of vaporization is seen to reduce downstream of the Impeller 1 trailing edge and through Diffuser 1, however, near the entrance of the Return Channel, i.e. in the region around the bend, the liquid shows rapid vaporization. For the 1% carryover case, ~ 0.05% liquid is observed to get vaporized in this region, whereas ~ 0.125% liquid vaporizes for the 5% liquid carryover case. Downstream of this region, the rate of vaporization is approximately constant. Overall, the variation in the rate of vaporization along the streamwise location is similar for all cases, however, with increasing

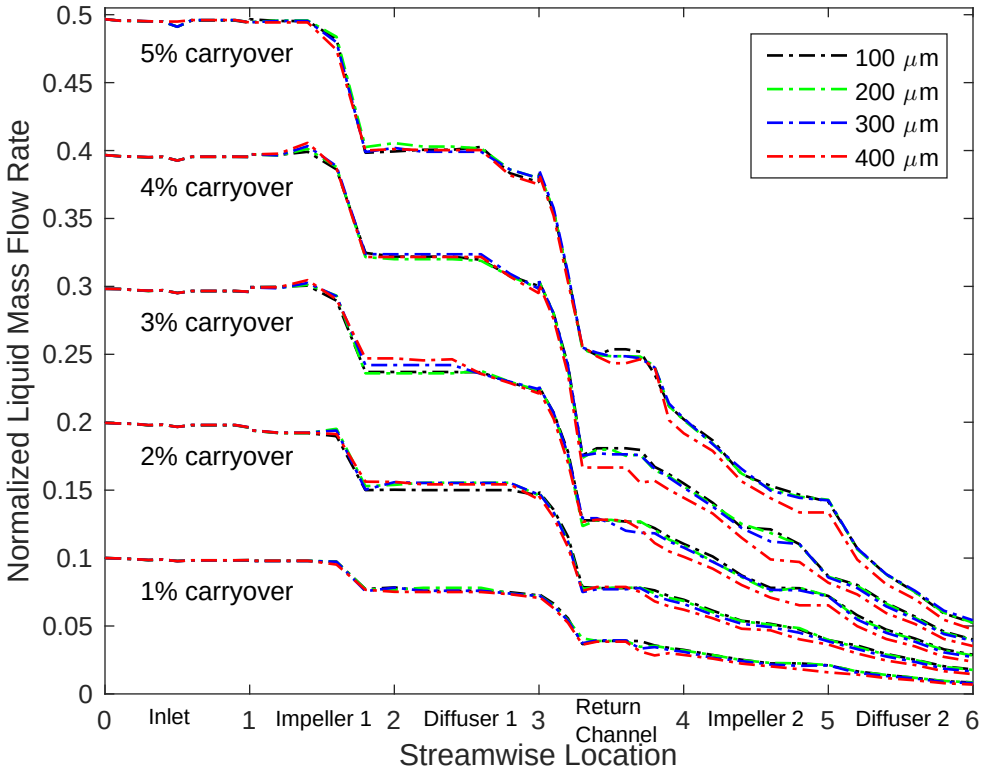

Figure 4.4: Streamwise liquid mass flow

liquid carryover, more amount of liquid is vaporized within the compressor geometry.

4.2.2 Effects of Droplet Size on Vaporization

A major factor governing the rate of liquid vaporization is the rate of interphase heat transfer. For the same mass of liquid carryover, a smaller droplet size will result in a larger surface area that is available for convective heat transfer. Therefore, smaller droplets can be expected to vaporize at a faster rate. However, Figure 4.4 shows that downstream of the Return Channel, the droplets with larger initial size vaporize at a faster rate. A possible explanation for this observation is that the droplets with larger initial size are more likely to undergo secondary breakup due to

aerodynamic deformation or splashing upon impingement. Figure 4.5 plots the droplet impact regimes as a function of the droplet diameter and the normal component of the droplet velocity. It can be seen that the normal velocity corresponding to the transition from rebound to splash regime is approximately double for droplets with diameter of 100 μm as compared to the droplets with diameter of 400 μm. This indicates that the number of droplets impinging in the splash regime, and hence the number of secondary droplets formed due to splashing are likely to be greater in cases with larger initial diameter.

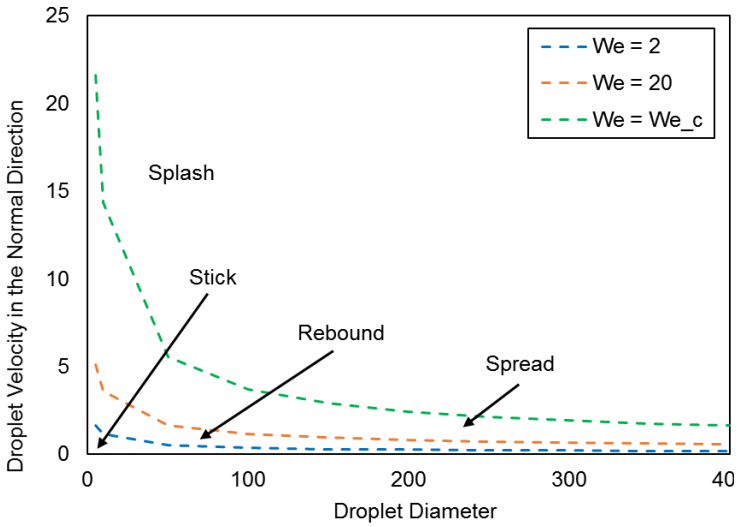

Figure 4.5: Droplet impact regimes

Aerodynamic deformation can also result in secondary droplet breakup. Since this process depends on the droplet Weber number, the average and maximum values of the droplet Weber number were calculated for the above simulations. For the case with initial droplet size of 100 μm, the average and maximum values of the droplet Weber number were found to be 5 and 388 respectively, whereas for the 400 μm case, these values were 27 and 5157. This indicates that the larger droplets are more likely to undergo secondary breakup due to aerodynamic deformation. The smaller secondary droplets formed due to splashing and / or breakup vaporize rapidly, which explains the trends seen in Figure 4.4.

4.3 Behavior of the Two-Phase Flow in the Compressor

The effects of two-phase flow on properties such as pressure, temperature and specific entropy were studied to gain insights on the behavior of two-phase flow in the compressor. In addition, the effects on the flow velocity were also examined. In the following subsections, the meridional contours of pressure, temperature, velocity and specific entropy (normalized on the basis of the average values at the compressor outlet) for the single phase as well as a representative two-phase flow case (5% liquid carryover and initial droplet size of 400 μm) are compared and the differences between the contours are highlighted.

4.3.1 Flow Behavior in Stage 1

4.3.1.1 Stage 1 Pressure

Figure 4.6 shows the static pressure contours in Stage 1. For the two cases, the difference in static pressure till the leading edge of the impeller is negligible, however it is seen to increase downstream of the leading edge. The diffuser region as well as the area near the impeller shroud show relatively greater differences. The maximum difference in static pressure between the two cases is ~ 0.7%. Overall, lower static pressures are observed in the two-phase flow case.

4.3.1.2 Stage 1 Temperature

The static temperature contours on the meridional plane are shown in Figure 4.7. Similar to static pressure, the difference in static temperature till the leading edge of the impeller is seen to be negligible, however the region near the impeller shroud shows greater difference. The maximum

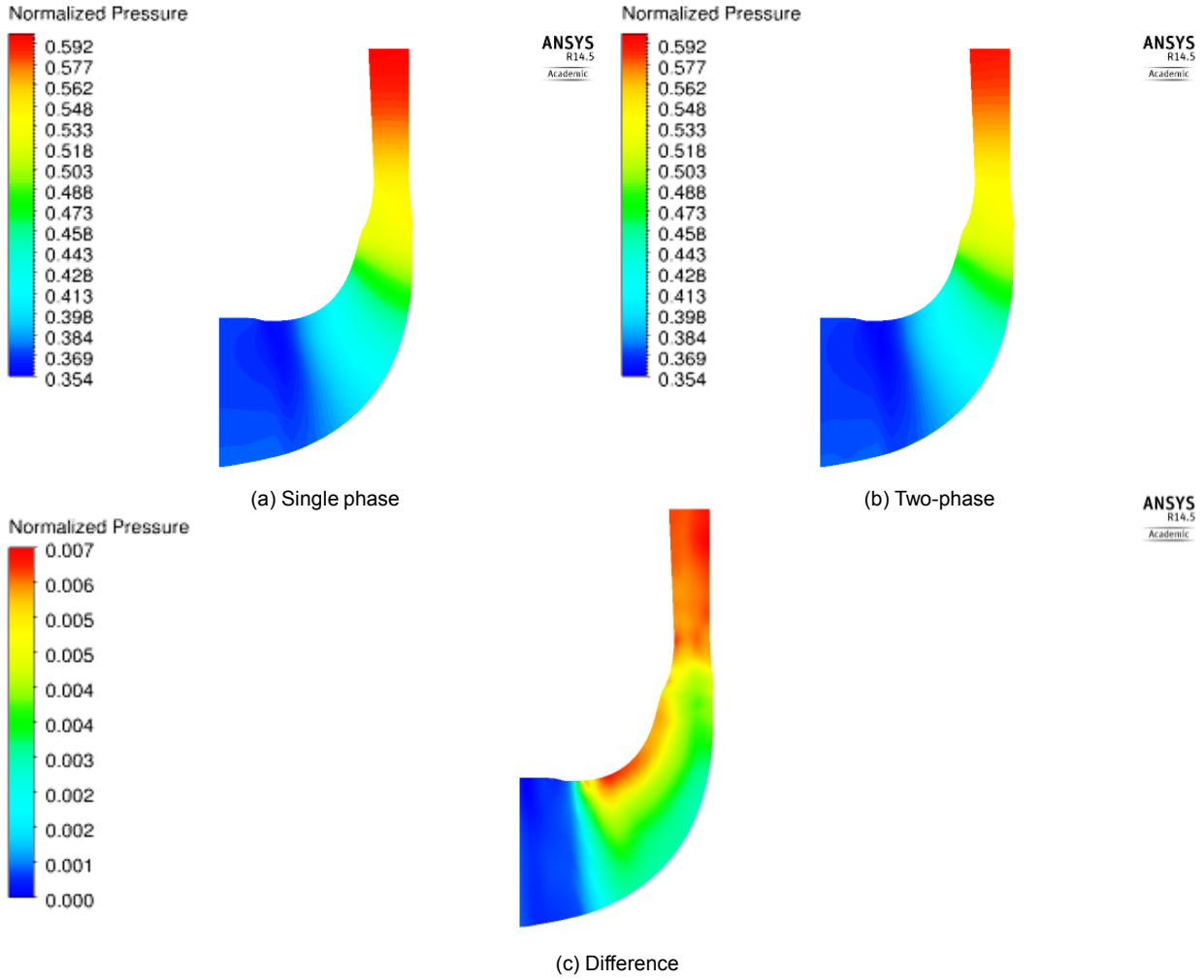

Figure 4.6: Stage 1 pressure contours

difference in static temperature between the two cases is observed near the shroud and the blade trailing edge, and is ~ 0.3%. Overall, the two-phase flow case shows lower static temperature as compared to the single phase flow case.

4.3.1.3 Stage 1 Velocity

Unlike static pressure and temperature, the velocity in the two-phase flow case is not consistently lower over the entire meridional plane, as seen from Figure 4.8. The difference in velocity till the

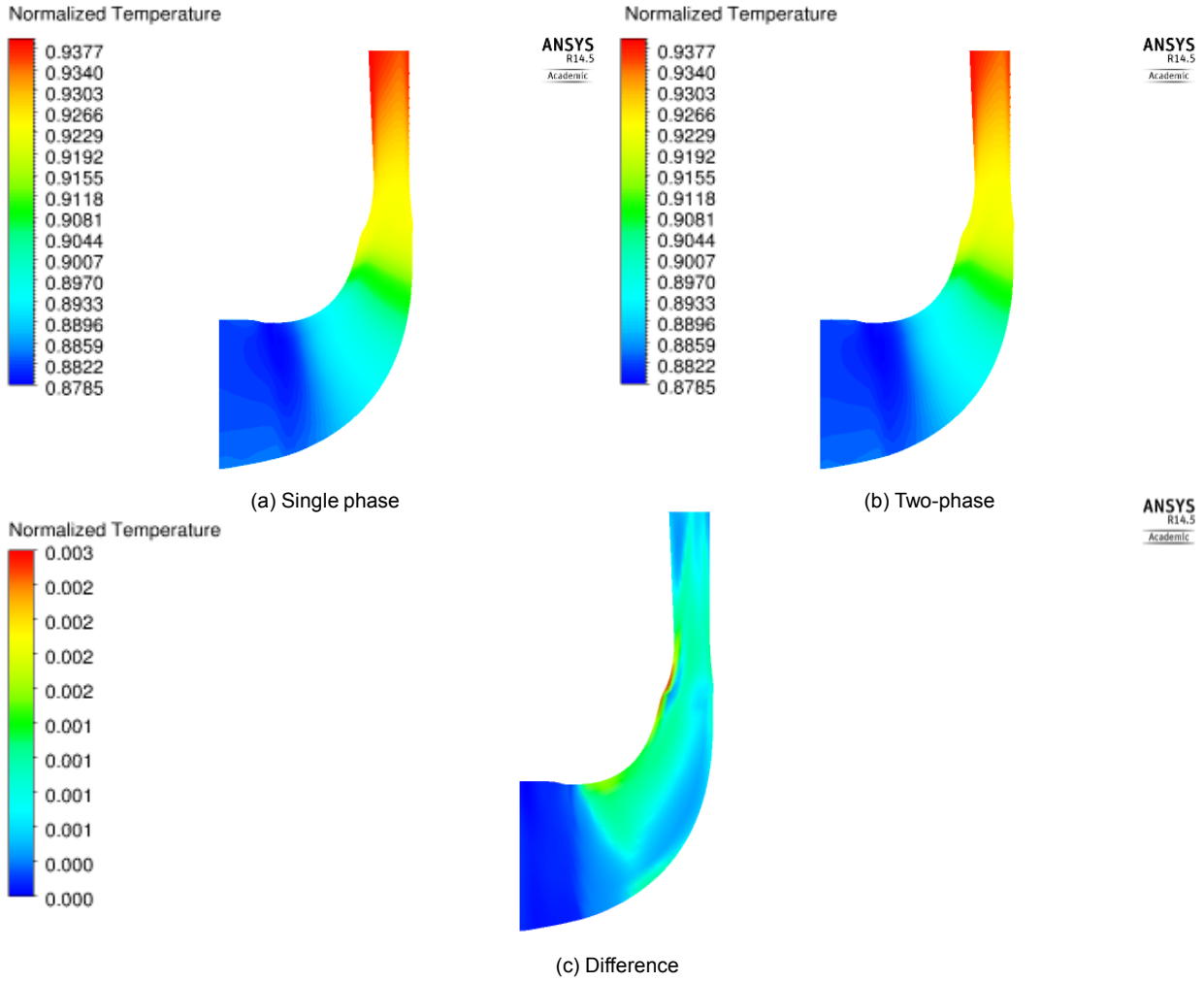

Figure 4.7: Stage 1 temperature contours

leading edge of the impeller is seen to be negligible, as in the previous cases. Also, as in the previous cases, the difference between the two contours is more noticeable near the shroud. In the region around the shroud and the blade leading edge and downstream of the trailing edge, the velocity in the two-phase flow case is observed to be higher by ~ 3.2%, whereas just upstream of the trailing edge, the two-phase flow velocity is lower by ~ 1.9%. The figure also shows that the extents of the regions that show differences in velocity field are smaller as compared to those for the temperature and pressure fields.

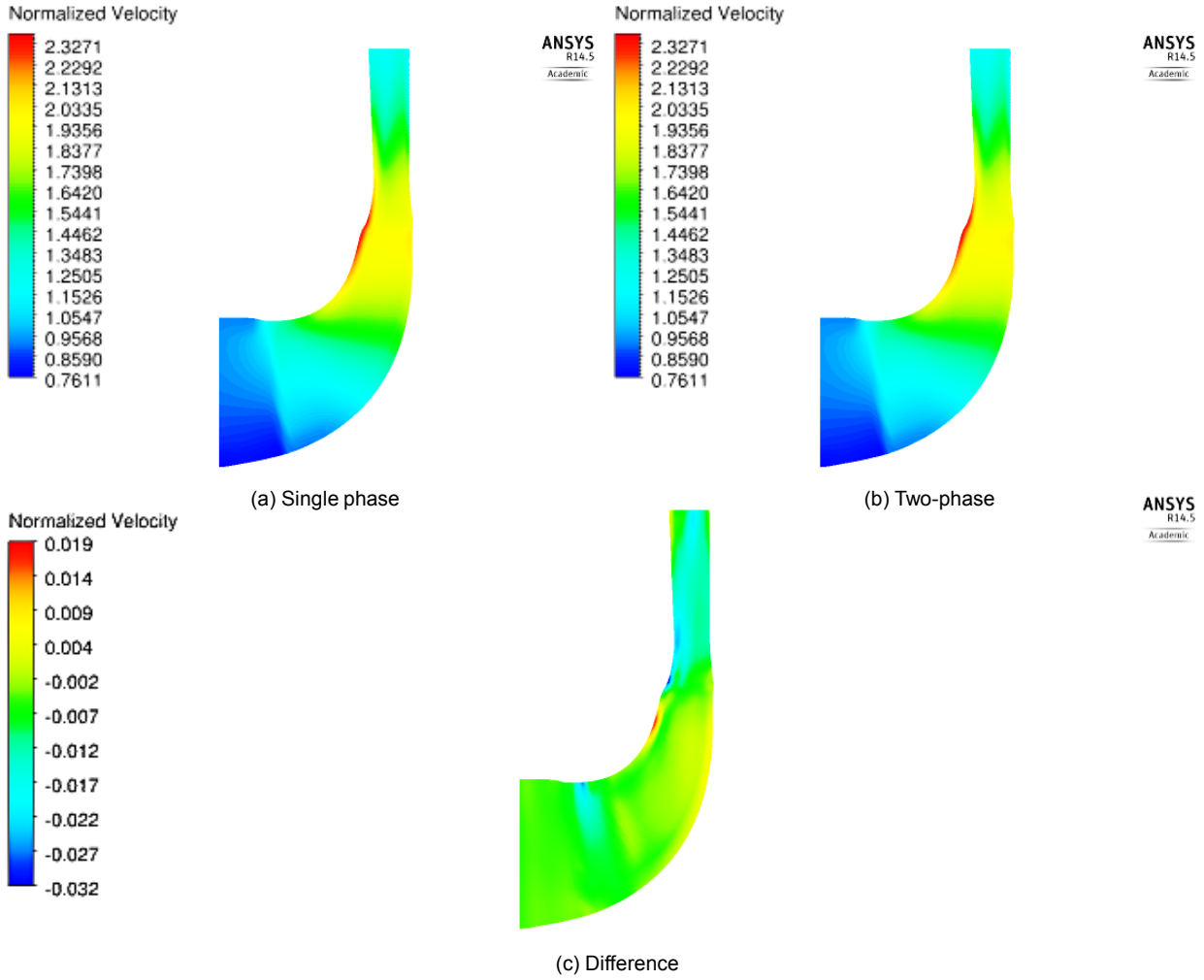

Figure 4.8: Stage 1 velocity contours

4.3.1.4 Stage 1 Specific Entropy

The specific entropy contours for the single phase and the two-phase flow case show negligible differences, as seen in Figure 4.9. The maximum difference (~ 0.2%) can be observed in a very small region near the shroud and the blade trailing edge.

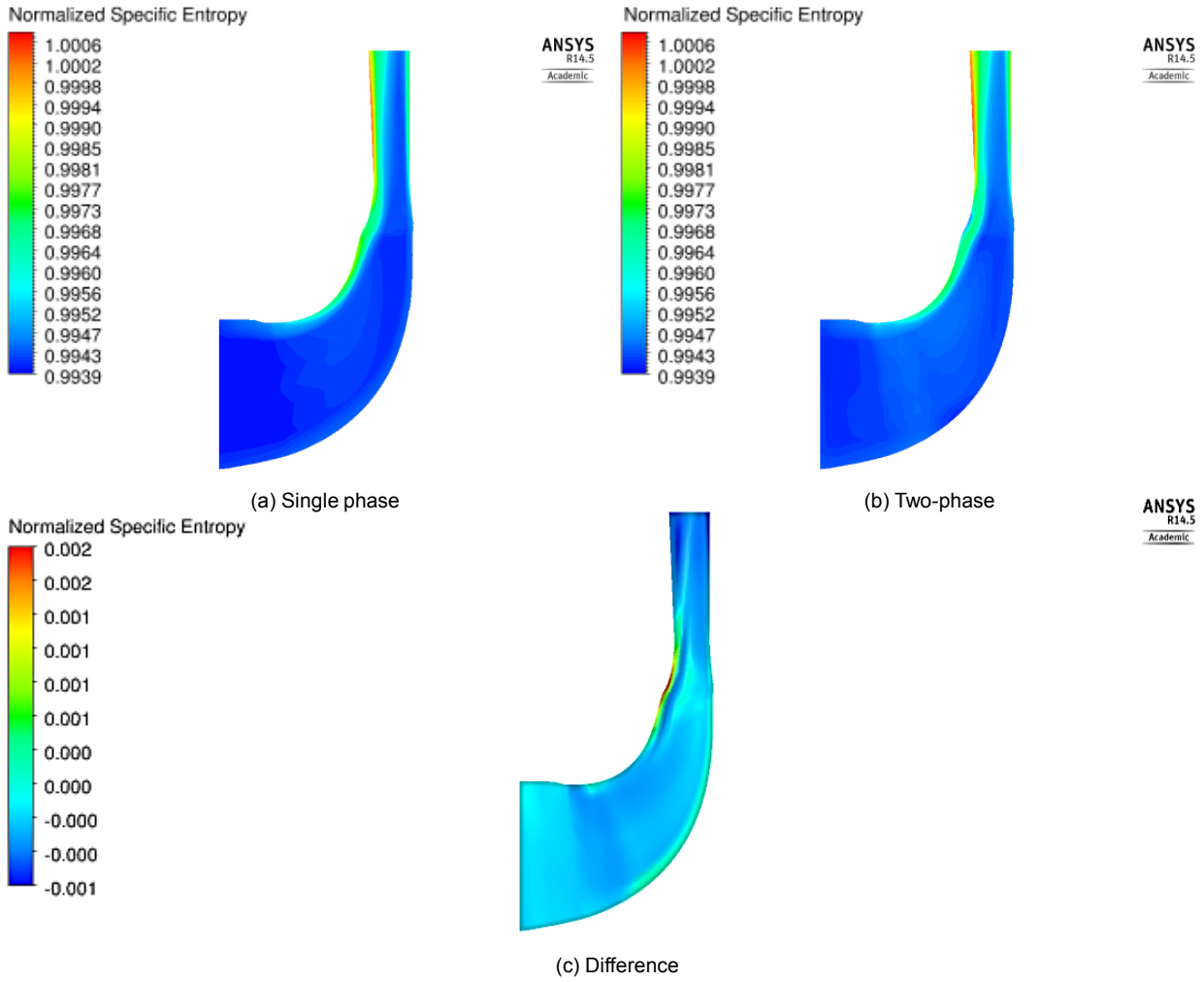

Figure 4.9: Stage 1 specific entropy contours

4.3.2 Flow Behavior in Return Channel

4.3.2.1 Return Channel Pressure

Figure 4.10 shows that the static pressure in the two-phase flow case is lower as compared to the single phase flow case. In the region near the bend, the difference between the two cases is ~ 0.5%, and is seen to increase downstream of the bend. From the figure, the maximum difference in static pressure between the two cases is ~ 1.6%.

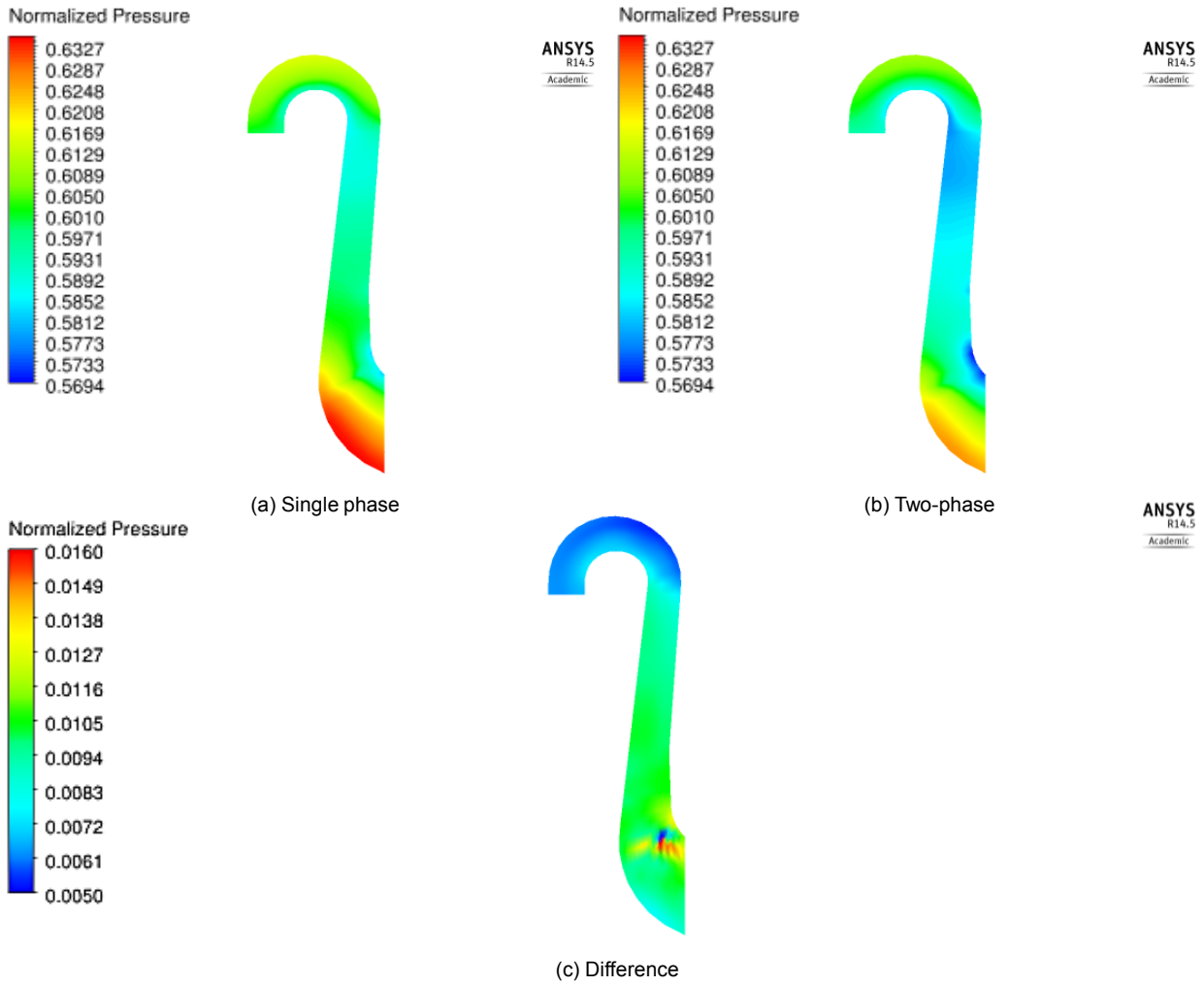

Figure 4.10: Return channel pressure contours

4.3.2.2 Return Channel Temperature

Figure 4.11 shows the static temperature contours on the meridional plane in the Return Channel. From the figure, the location of maximum difference (~ 0.23%) is the region near the shroud, immediately downstream of the bend. Overall, as expected, lower static temperatures are seen in the case of two-phase flow case.

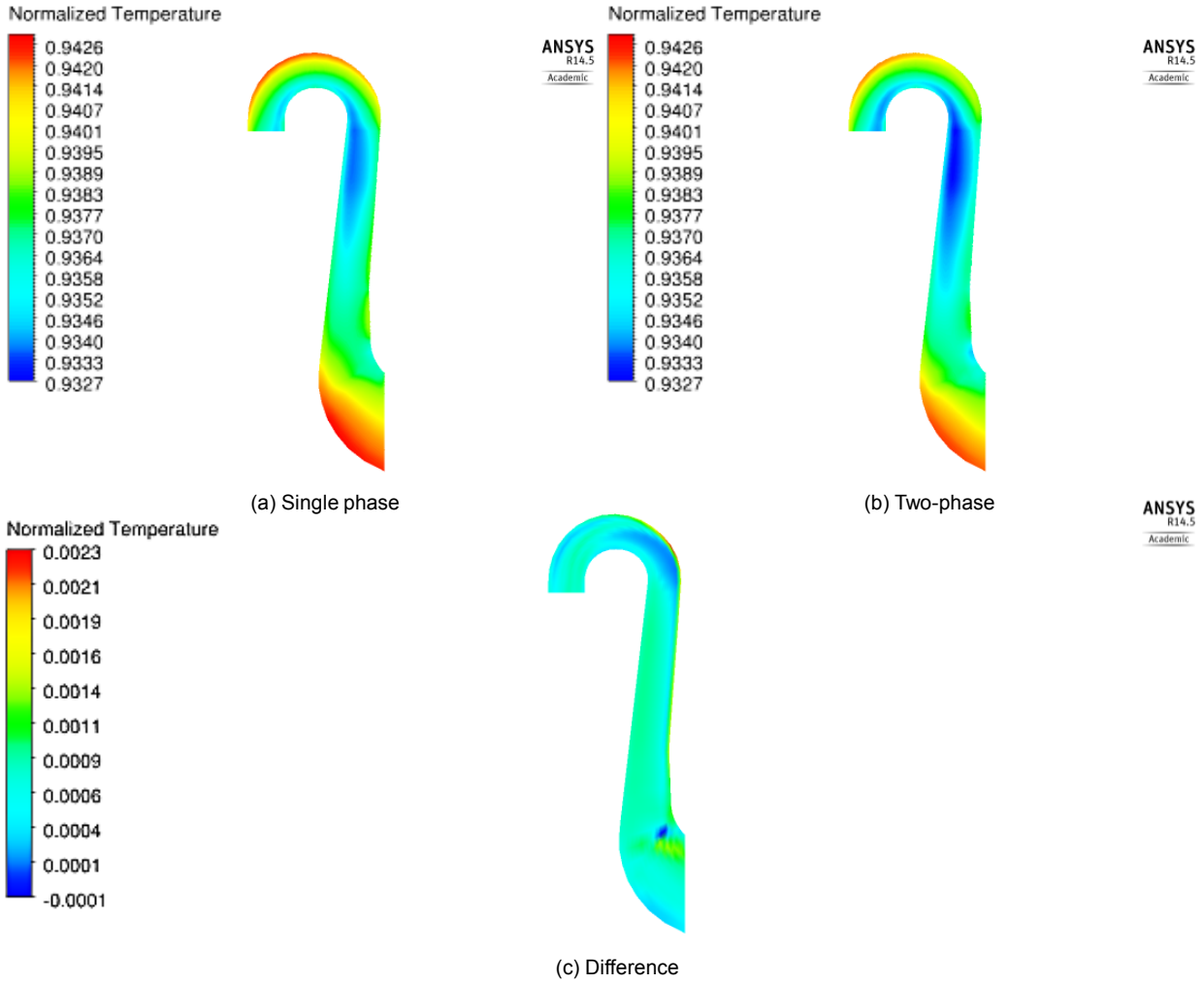

Figure 4.11: Return channel temperature contours

4.3.2.3 Return Channel Velocity

The velocity contours on the meridional plane in the Return Channel are shown in Figure 4.12. The region around the bend, near the shroud and around the exit of the Return Channel, near the hub show relatively small difference. However, the flow velocity in the two-phase flow case is seen to be higher by ~ 5% in the Return Channel passage.

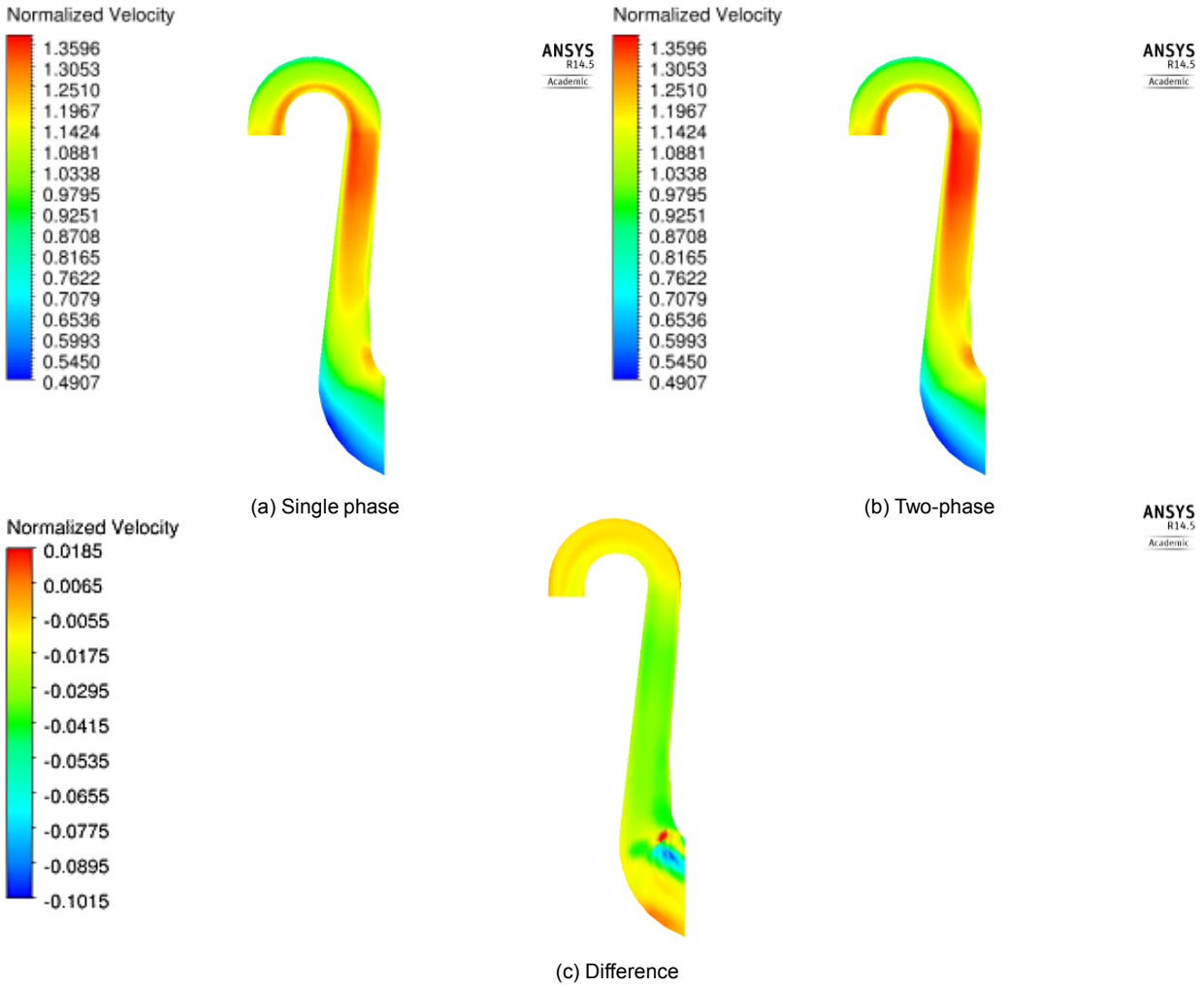

Figure 4.12: Return channel velocity contours

4.3.2.4 Return Channel Specific Entropy

Figure 4.13, which shows the specific entropy contours on the meridional plane in the Return Channel, reveals that the specific entropy is slightly higher in most of the Return Channel passage for the two-phase flow case, with the exception of a small region near the shroud. This region also matches with the droplet trajectories. The maximum difference between the single phase and two-phase flow case is ~ 0.21%.

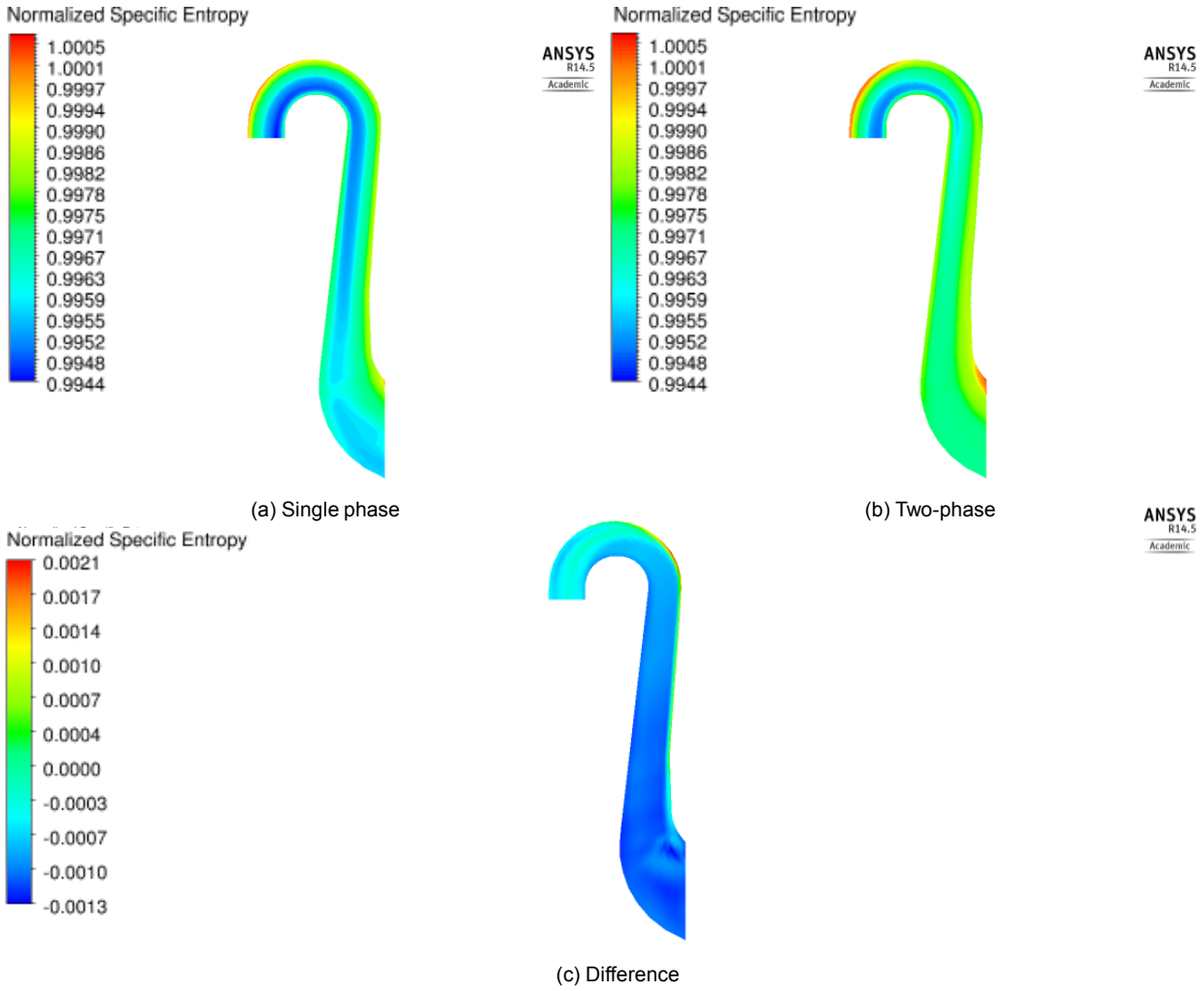

Figure 4.13: Return channel specific entropy contours

4.3.3 Flow Behavior in Stage 2

4.3.3.1 Stage 2 Pressure

As compared to Stage 1, the difference in static pressure between the single phase and two-phase flow case is significant for Stage 2. This is clearly seen from Figure 4.14. Along the streamwise direction, this difference is observed to increase, with the maximum difference (~ 5.12%) occurring at the outlet.

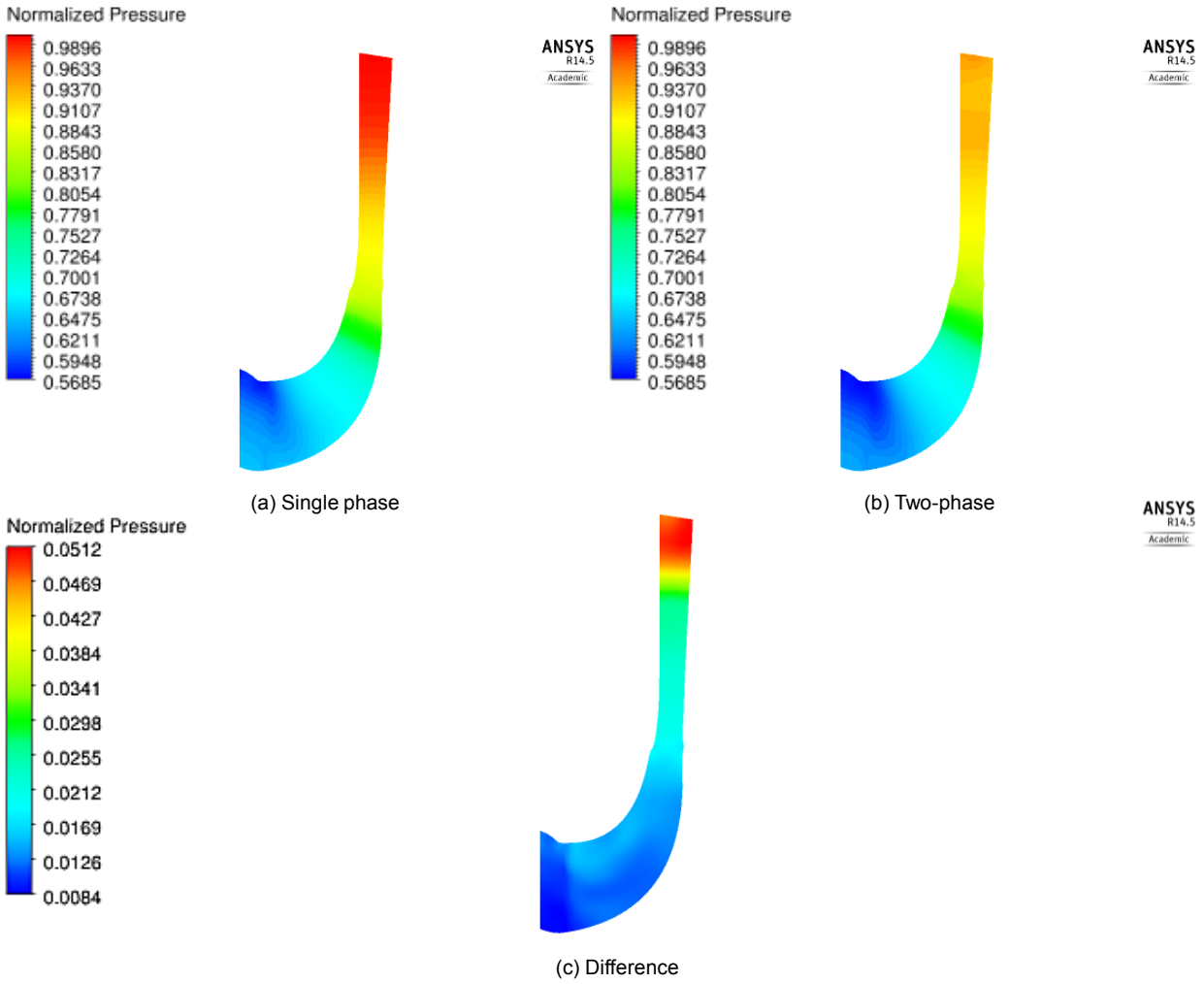

Figure 4.14: Stage 2 pressure contours

4.3.3.2 Stage 2 Temperature

Similar to Stage 1, the static temperature in the case of two-phase flow is lower as compared to the single phase flow case, as seen in Figure 4.15. The temperature differences are seen to be greater in the region that also shows more number of droplet tracks. This is clearly observed in the Impeller 2 domain. The maximum temperature difference (~ 0.41%) is seen near the outlet. Overall, as expected, the two-phase flow case shows lower static temperatures.

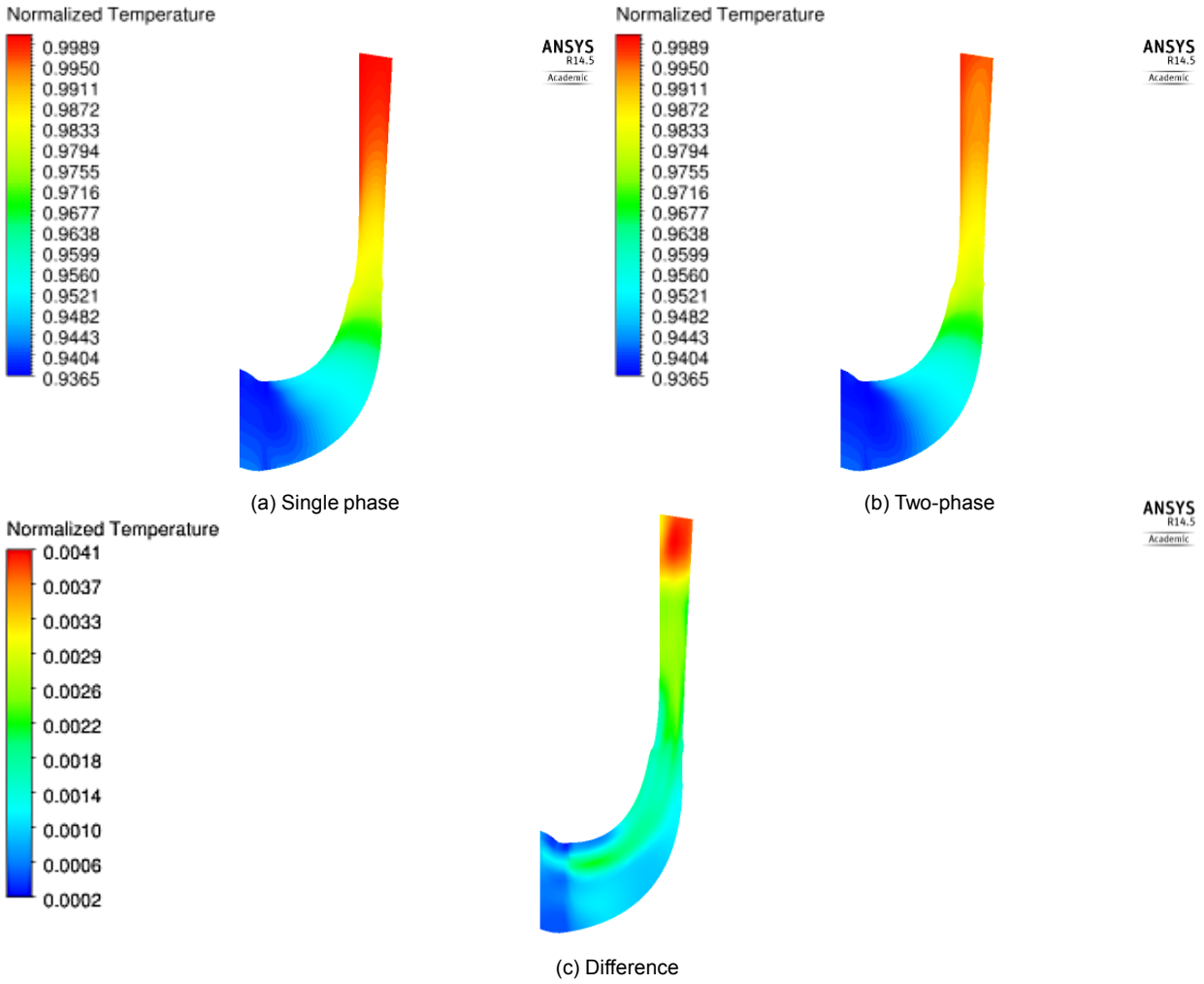

Figure 4.15: Stage 2 temperature contours

4.3.3.3 Stage 2 Velocity

Figure 4.16 shows that the two-phase flow results in higher velocity in a large region of Stage 2. In particular, the region near the shroud and the Impeller 2 leading edge shows difference as high as ~ 12.34%. However, a zone of lower velocity, which matches with the droplet trajectories, is also observed.

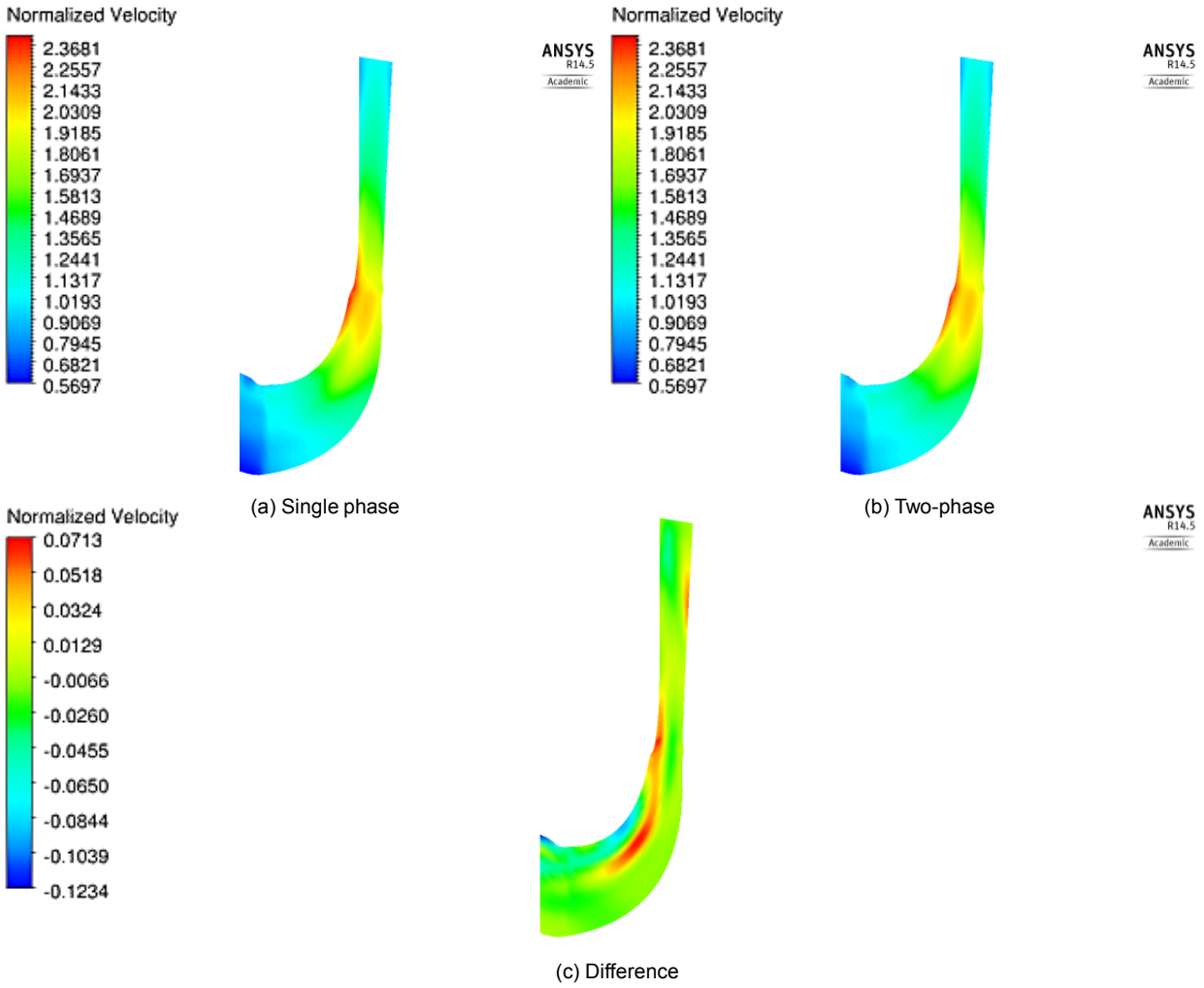

Figure 4.16: Stage 2 velocity contours

4.3.3.4 Stage 2 Specific Entropy

From Figure 4.17, the specific entropy in the two-phase flow case is seen to be higher as compared to the single phase flow case. This difference is relatively greater in Diffuser 2, with a maximum value of ~ 0.39%. The region matching with the droplet trajectories shows relatively smaller difference, which indicates that the increase in specific entropy in this region is relatively smaller.

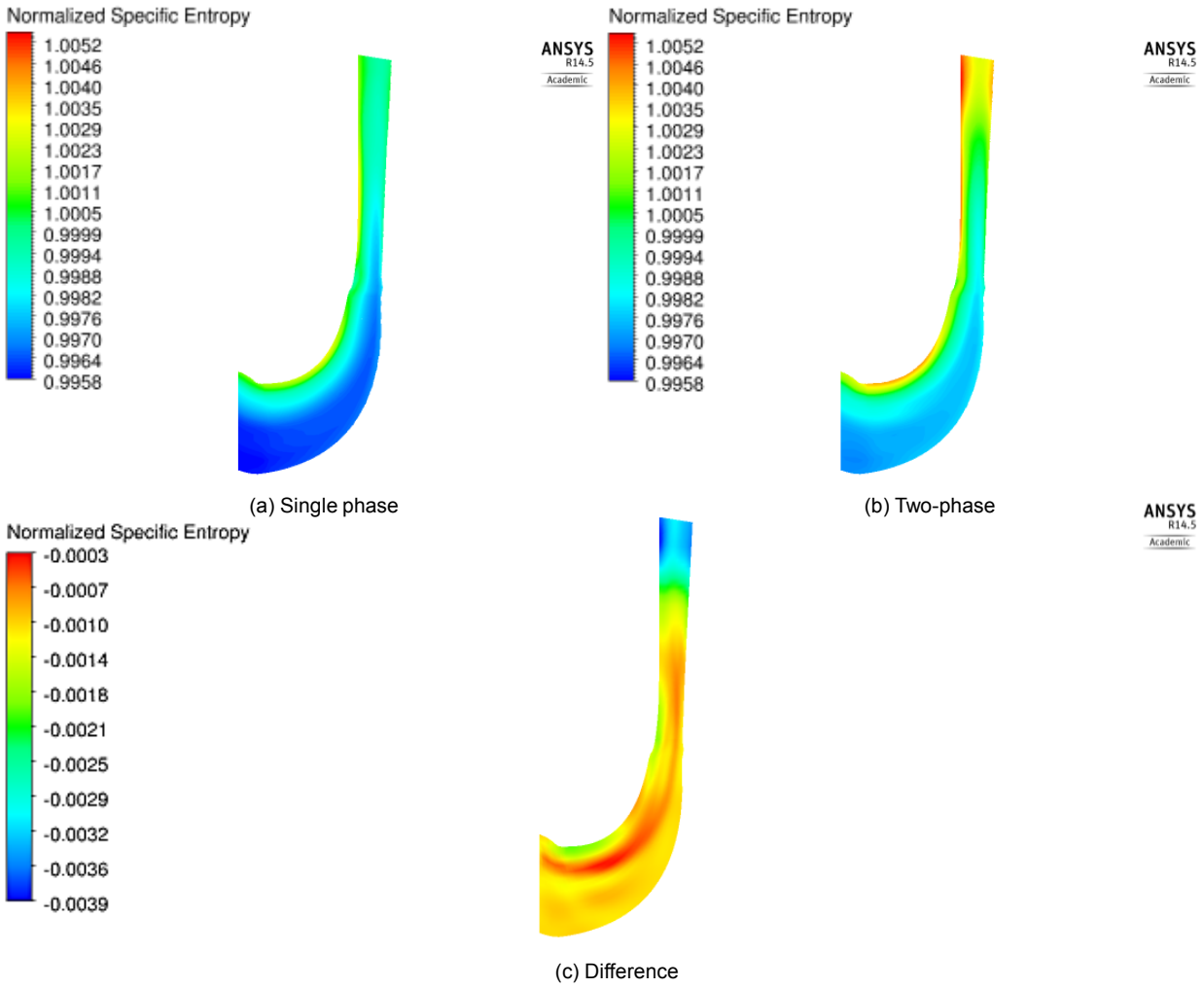

Figure 4.17: Stage 2 specific entropy contours

4.3.4 Discussions on the Flow Behavior

The above results show that overall, liquid carryover results in reducing the static pressure and temperature and increasing the specific entropy and velocity. This effect is observed in all parts i.e. Stage 1, Return Channel, and Stage 2. Also, the relative differences in static pressure and velocity are greater as compared to the relative differences in static temperature and entropy. It should also be noted that the increase in vapor mass (as a result of liquid vaporization) will result in higher net entropy, and hence the difference in net entropy between the single phase and the

two-phase flow case will be greater.

The contour plots also reveal that in the two-phase flow case, the regions of lower static temperature match with the droplet tracks. This is expected, since the vaporization of the droplets will result in lowering of the vapor phase temperature. The above can be clearly observed in the contours for the Return Channel and Stage 2, where the droplet tracks are more localized, and do not cover the entire span of the domain. The lowering of static pressure, however, is not limited to the regions corresponding to the droplet tracks, but is observed over a larger area. Since for a real gas, the specific entropy is a function of both temperature and pressure, the changes in the temperature and pressure fields due to two-phase flow result in changing the specific entropy, as seen from the contour plots.

Chapter 5

Effects of Two-Phase Flow on the Compressor Performance

As seen in Chapter 4, liquid carryover alters the flow field within the compressor and therefore is likely to affect its performance. This chapter presents a detailed analysis of the compressor performance, by quantifying it in terms of the pressure ratios, input power and the adiabatic and polytropic efficiencies. The performance of Stage 1, Return Channel and Stage 2 is evaluated separately, in addition to the analysis of the entire compressor system. The changes in blade loading of both impellers and the Return Channel vane are also reported. In addition, the implications of neglecting the turbulent dispersion of the droplets and assuming ideal gas behavior for the vapor phase on the compressor performance are discussed.

5.1 Calculation of the Performance Parameters

The calculation of the parameters that were used to quantify the performance is briefly covered in this section. These calculations apply to the single phase as well as the two-phase flow cases. In all calculations, station 1 corresponds to the inlet of the section under consideration, and station 2 corresponds to the outlet of the section.

5.1.1 Calculation of Pressure Ratios

The total to static pressure ratio was calculated by using Equation 5.1.

$$PR_{ts} = \frac{p_2}{p_{01}} \tag{5.1}$$

The total to total pressure ratio was calculated by using Equation 5.2.

$$PR_{tt} = \frac{p_{02}}{p_{01}} \tag{5.2}$$

5.1.2 Calculation of Input Power

The power input was computed from the energy balance equation, shown in Equation 5.3.

$$\dot{W}_c = \dot{m}_{2,g}\, h_{02,g} + \dot{m}_{2,f}\, h_{02,f} - (\dot{m}_{1,g}\, h_{01,g} + \dot{m}_{1,f}\, h_{01,f}) \tag{5.3}$$

It is worth noting that in the case of phase change, $\dot{m}_{2,g} \neq \dot{m}_{1,g}$, and $\dot{m}_{2,f} \neq \dot{m}_{1,f}$. Thus, the above expression accounts for the vaporization of the liquid that may be occurring within the system.

5.1.3 Calculation of Adiabatic and Polytropic Efficiencies

In addition to the irreversibilities associated with the compression process, two-phase flow involves irreversibilities due to the interphase momentum, heat, and mass transfer. At a given pressure, the phase change process is associated with a rise in entropy ($s_g - s_f$), which will occur even in an "ideal" vaporization process. Therefore, it needs to be included appropriately in the efficiency calculations. The mixing of the vaporizing liquid with the surrounding vapor also results in increasing the entropy. Thus, the calculation of the adiabatic and polytropic efficiencies under two-phase flow condition is not trivial.

In this section, only the definitions of the efficiencies are shown. The details of the calculation procedure are given in Appendix A.

The total to static adiabatic efficiency is given by Equation 5.4.

$$\eta_{ts} = \frac{H_{2,s} - H_{01}}{H_{02} - H_{01}} \tag{5.4}$$

Similarly, the total to total adiabatic efficiency is given by Equation 5.5.

$$\eta_{tt} = \frac{H_{02,s} - H_{01}}{H_{02} - H_{01}} \tag{5.5}$$

In the two-phase flow cases, the enthalpy terms in the above equations include the enthalpy of

both liquid and vapor phases.

The polytropic efficiency is given by Equation 5.6

$$\eta_p = \frac{dh_s}{dh_{actual}} \tag{5.6}$$

The total to total and total to static polytropic efficiencies are calculated by using the corresponding total or static conditions appropriately.

5.1.4 Calculation of Pressure Coefficient

The performance of the Stage 1 and Stage 2 diffusers was quantified in terms of the diffuser pressure coefficient, shown in Equation 5.7. The reference values that were used to compute the diffuser pressure coefficients were calculated at the inlet stations of that diffuser.

$$C_{p,d} = \frac{p - p_{ref}}{p_{0,ref} - p_{ref}} \tag{5.7}$$

Since the losses in the Return Channel are reflected in the form of total pressure, the Return Channel pressure coefficient, shown in Equation 5.8, was calculated using the total pressure instead of the static pressure.

$$C_{p,rc} = \frac{p_0 - p_{ref}}{p_{0,ref} - p_{ref}} \tag{5.8}$$

The above performance parameters were normalized by the values of the corresponding param-

eters in the single phase flow case. Thus, for any given parameter, a value less than one indicates that the magnitude of the parameter is less in the two-phase flow case as compared to the single phase flow case, and vice versa.

5.2 Stage 1 Performance

The effects of two-phase flow on the performance of Stage 1 (i.e. Impeller 1 and Diffuser 1) are reported in this section. For this stage, station 1 corresponds to the inlet of Impeller 1 and station 2 corresponds to the outlet of Diffuser 1.

5.2.1 Stage 1 Pressure Ratio

Figure 5.1 shows that the normalized total to static and total to total pressure ratios are lower as compared to the single phase flow case. Both pressure ratios are seen to increase almost linearly with increasing amount of liquid carryover, however the difference between the 1% and 5% liquid carryover is less than 0.5%. For the same amount of liquid carryover, the pressure ratios are observed to be slightly greater for the cases with larger initial droplet size. This is more noticeable at higher amount of liquid carryover.

5.2.2 Diffuser 1 Pressure Coefficient

From Figure 5.2, increasing liquid carryover is seen to have an adverse effect on the Diffuser 1 pressure coefficient. This effect is more pronounced for the cases with smaller initial droplet size. For example, the pressure coefficient for initial droplet size of 100 μm shows a reduction of ~ 0.9

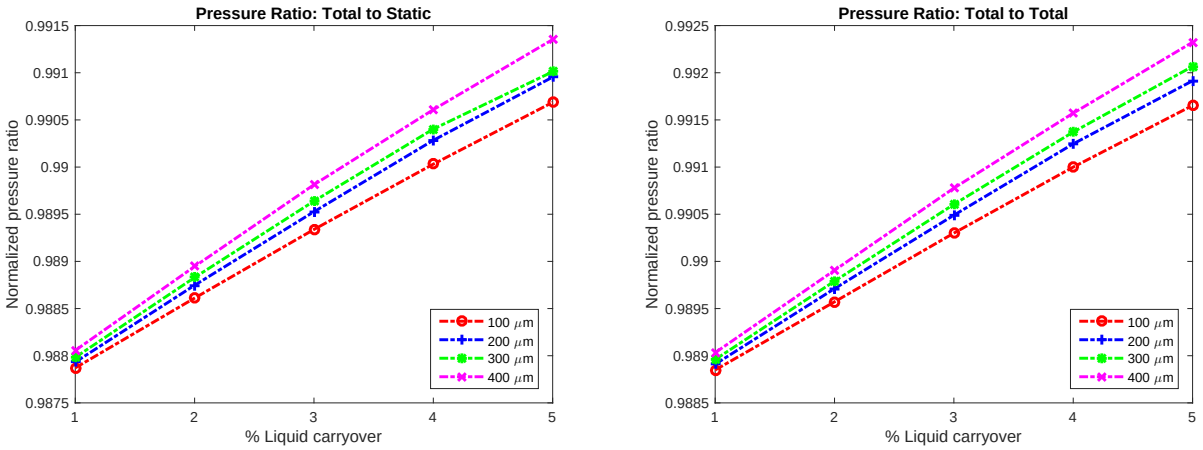

(a) Total to static

(b) Total to total

Figure 5.1: Stage 1 pressure ratio

% as the amount of liquid carryover is increased from 1% to 5%, as compared to the reduction of ~ 0.4% for initial droplet size of 400 μm.

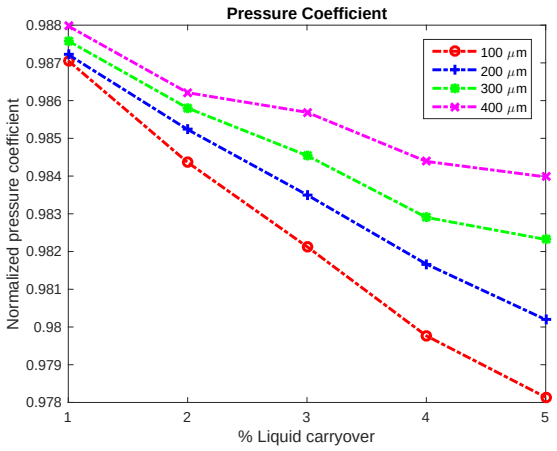

Figure 5.2: Diffuser 1 pressure coefficient

5.2.3 Stage 1 Power Input

Stage 1 consumes more power under two-phase flow conditions as compared to the single phase flow case, as seen from Figure 5.3. The figure shows increase of ~ 16% in the power input as the amount of liquid carryover is increased from 1% to 5%. However, the effect of the initial droplet size on the power input is seen to be negligible.

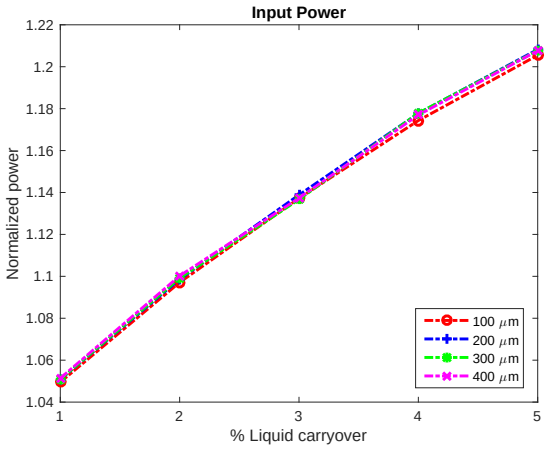

Figure 5.3: Stage 1 power input

5.2.4 Stage 1 Adiabatic Efficiency

The decrease in the pressure ratios and increase in the power input indicate that liquid carryover affects the performance of Stage 1 adversely. This is clearly seen in the total to static and total to total efficiency plots in Figure 5.4. The effects of increasing the amount of liquid carryover and the initial droplet size are consistent with the observed trends in the pressure ratios and power input.

It should be noted that the efficiencies were normalized by the corresponding efficiency for the single phase flow case, i.e. by a number that is less than one. Thus, the difference in the normal-

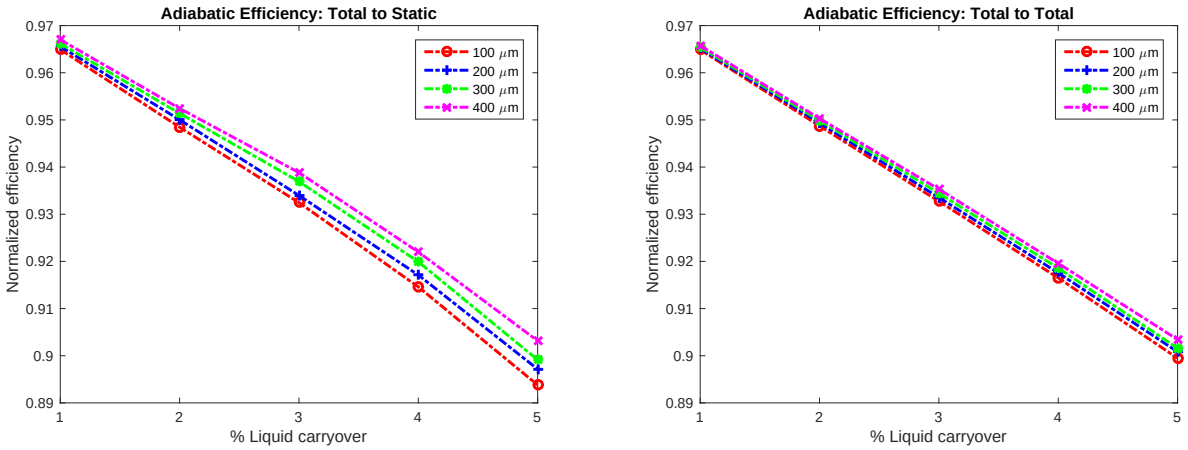

(a) Total to static

(b) Total to total

Figure 5.4: Stage 1 adiabatic efficiency

ized efficiencies in Figure 5.4 appears greater than the "actual" difference.

5.2.5 Stage 1 Polytropic Efficiency

Figure 5.5 shows that similar to the adiabatic efficiencies, the effects of liquid carryover are also detrimental to the total to static and total to total polytropic efficiencies. As compared to the adiabatic efficiencies, the reduction in polytropic efficiencies is observed to be greater. Also, the effects of initial droplet size are seen to be negligible.

5.3 Return Channel Performance

This section compares the performance of the Return Channel under single phase and two-phase flow conditions, in terms of the Return Channel pressure coefficient. For this analysis, station 1 corresponds to the inlet of the Return Channel and station 2 corresponds to the outlet of the

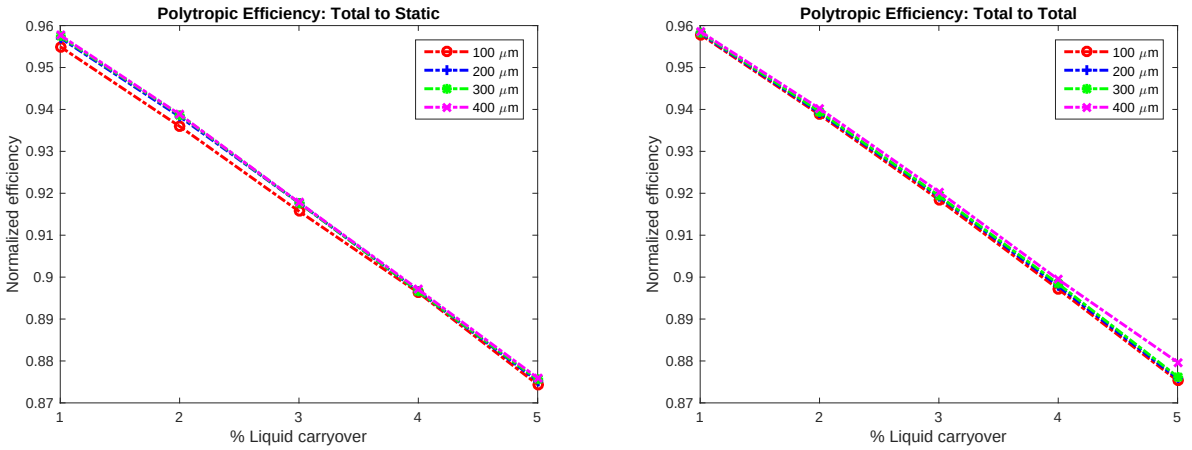

(a) Total to static

(b) Total to total

Figure 5.5: Stage 1 polytropic efficiency

Return Channel.

5.3.1 Return Channel Pressure Coefficient

Unlike Stage 1, the performance of the Return Channel improves significantly under two-phase flow conditions, as seen from Figure 5.6. The Return Channel pressure coefficient is seen to increase with increasing amount of liquid carryover as well as with increasing initial droplet size.

Since the Return Channel pressure coefficient is based on the total pressure, it can be concluded that the relative loss in total pressure decreases under two-phase flow conditions.

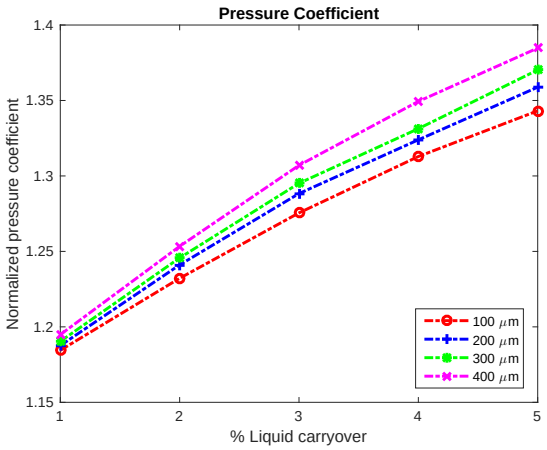

Figure 5.6: Return channel pressure coefficient

5.4 Stage 2 Performance

The effects of two-phase flow on the performance of Stage 2 (i.e. Impeller 2 and Diffuser 2) are reported in this section. For this stage, station 1 corresponds to the inlet of Impeller 2 and station 2 corresponds to the outlet of Diffuser 2.

5.4.1 Stage 2 Pressure Ratio

As seen from Figure 5.7, unlike Stage 1, the total to static and total to total pressure ratios for Stage 2 decrease with increasing amount of liquid carryover. The magnitude of this decrease is significantly greater as compared to Stage 1. Also, it can be seen that the initial droplet size has very little influence on the pressure ratios.

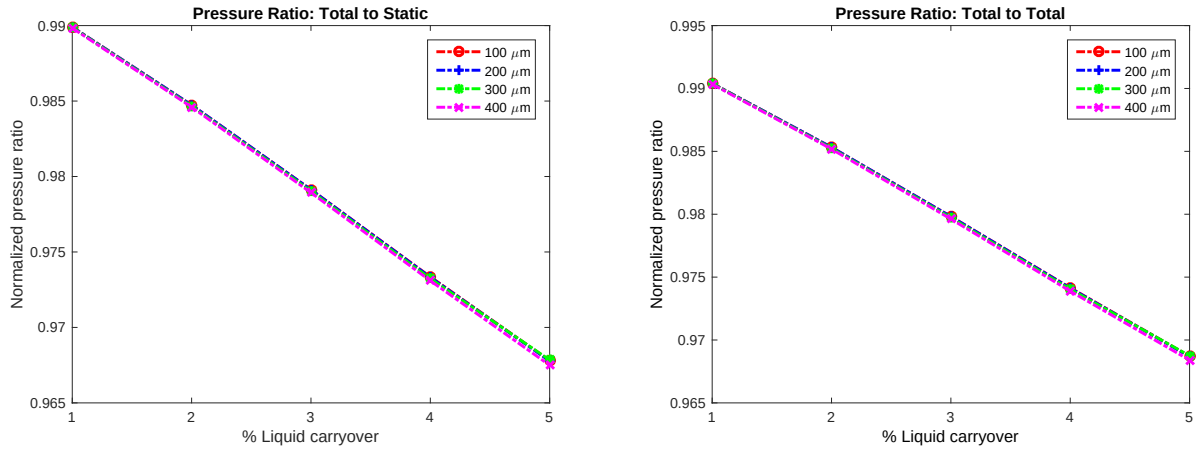

(a) Total to static

(b) Total to total

Figure 5.7: Stage 2 pressure ratio

5.4.2 Diffuser 2 Pressure Coefficient

The detrimental effects of liquid carryover on Diffuser 2 pressure coefficient are also significant as compared to Stage 1, as seen from Figure 5.8. Similar to the pressure ratios, the effects of initial droplet size are seen to be negligible.

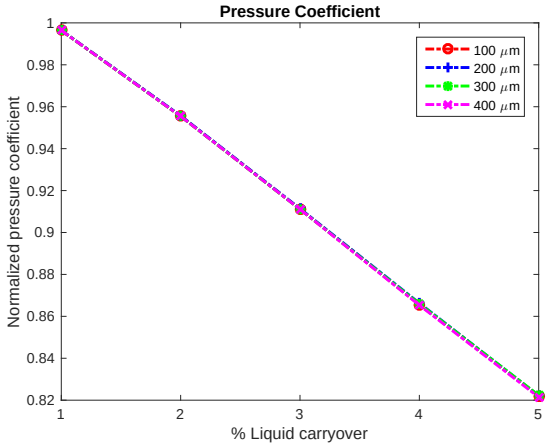

Figure 5.8: Diffuser 2 pressure coefficient

5.4.3 Stage 2 Power Input

From Figure 5.9, the power input is observed to increases with increasing amount of liquid carryover. This increase is smaller as compared to Stage 1. However, unlike Stage 1, which shows negligible effects of initial droplet size, the increase in power input with increasing liquid carryover is greater for the case with smaller initial droplet size.

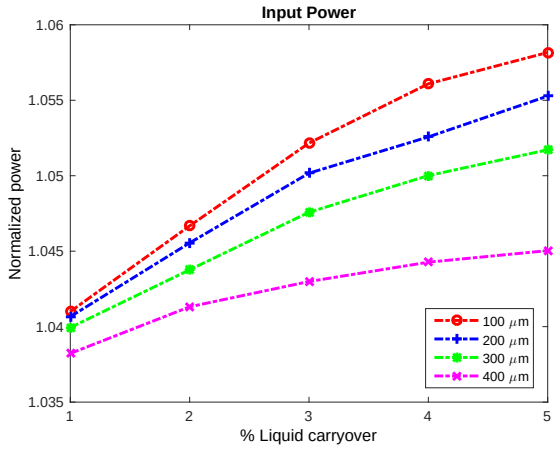

Figure 5.9: Stage 2 power input

5.4.4 Stage 2 Adiabatic Efficiency

Figure 5.10 shows that the Stage 2 total to static adiabatic efficiency increases significantly under two-phase flow conditions. The flow behavior analysis in Chapter 4 showed that liquid carryover results in reducing the static temperature in Stage 2. The beneficial effects of this intercooling is reflected in this observed increase. The effect of initial droplet size on the total to static adiabatic efficiency is seen to be negligible.

On the other hand, the total to total adiabatic efficiency under two-phase flow conditions is lower as compared to the single phase flow case, however, as compared to Stage 1, this degradation is

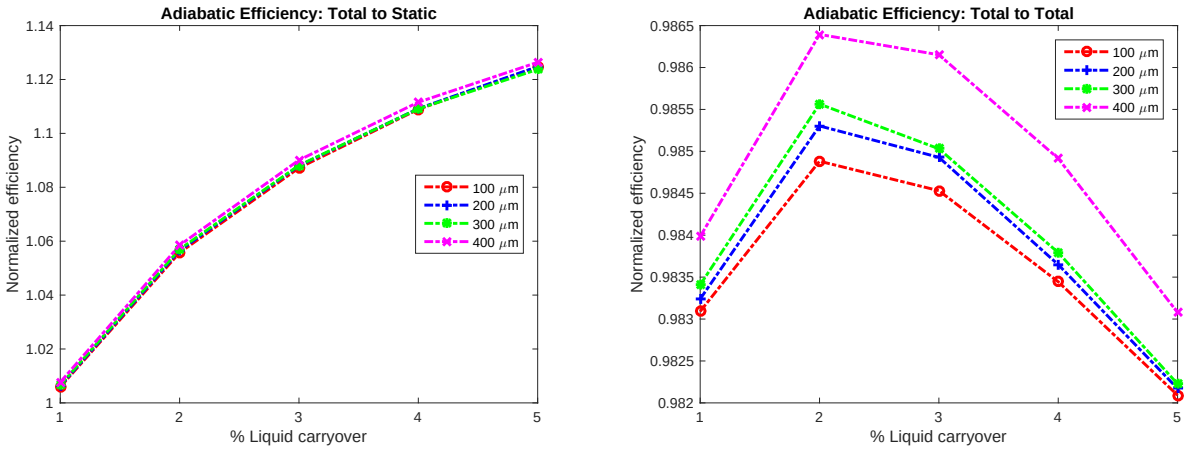

(a) Total to static

(b) Total to total

Figure 5.10: Stage 2 adiabatic efficiency

lower. Also, the efficiency trends do not show a direct relationship with the amount of liquid carryover. The maximum total to total adiabatic efficiency is observed at 2% liquid carryover whereas the minimum occurs at 5% liquid carryover. Also, for the same amount of liquid carryover, cases with larger initial droplet size show higher efficiency.

5.4.5 Stage 2 Polytropic Efficiency

The total to static and total to total polytropic efficiencies are seen to be lower in the two-phase flow cases, as seen from Figure 5.11. The figure shows that unlike the adiabatic efficiencies, increasing amount of liquid carryover has a detrimental effect on both efficiencies. Also, for the same amount of liquid carryover, cases with larger initial droplet size exhibit slightly higher efficiency.

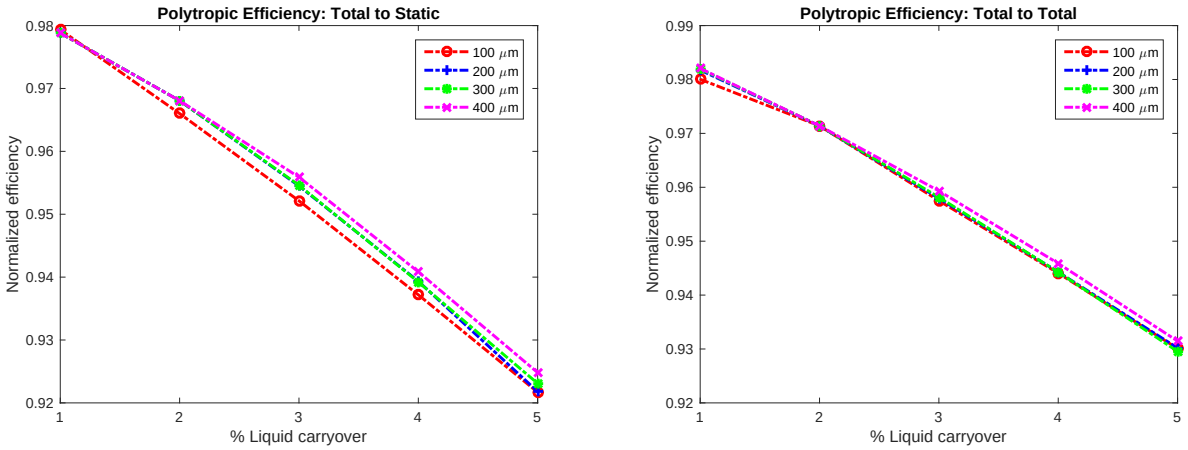

(a) Total to static

(b) Total to total

Figure 5.11: Stage 2 polytropic efficiency

5.5 Overall Performance

The effects of two-phase flow on the overall performance of the compressor are reported in this section. For this analysis, station 1 corresponds to the inlet and station 2 corresponds to the outlet of the entire computational domain.

5.5.1 Overall Pressure Ratio

Figure 5.12 shows that the decrease in overall total to static and total to total pressure ratios under two-phase flow conditions are comparable to those observed for Stage 2. This is expected, because the Stage 1 analysis indicated very small changes in the pressure ratios. The observation of negligible effects of initial droplet size is also consistent with the observations reported for Stage 1 and Stage 2.

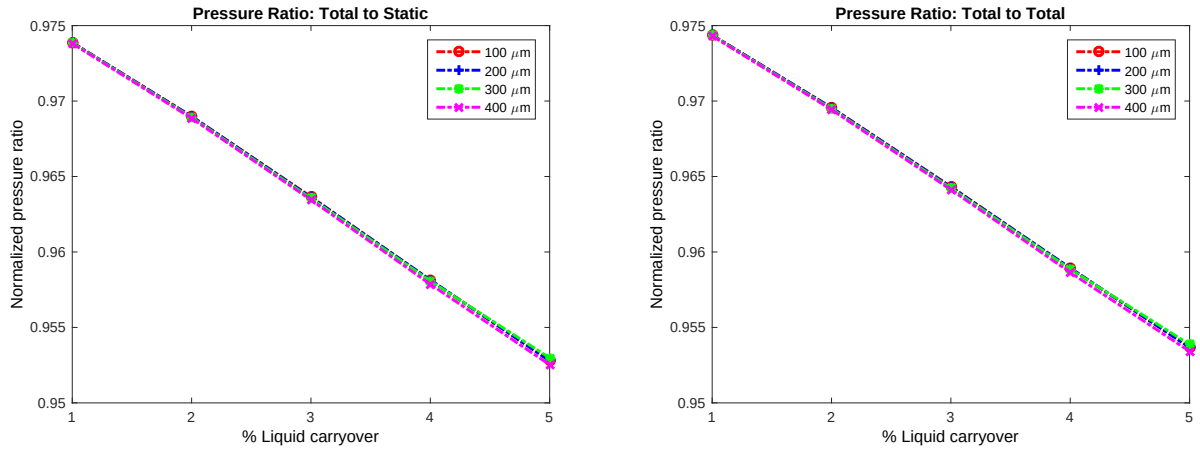

(a) Total to static

(b) Total to total

Figure 5.12: Overall pressure ratio

5.5.2 Overall Power Input

Figure 5.13 shows that the overall power input increases with increasing liquid carryover. The effects of initial droplet size are evident for higher amount of liquid carryover. These trends are consistent with those observed for Stage 1 and Stage 2.

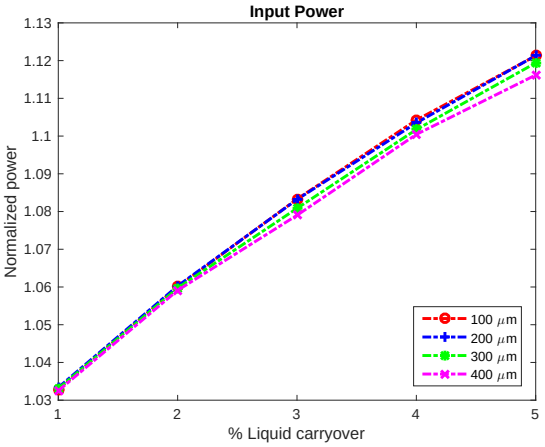

Figure 5.13: Overall Power input

5.5.3 Overall Adiabatic Efficiency

Increasing amount of liquid carryover adversely affects the overall total to static and total to total efficiencies, as seen from Figure 5.14. As compared to the total to static efficiency, the effects on the total to total adiabatic efficiency are more pronounced. Also, the initial droplet size shows negligible effects on both efficiencies.

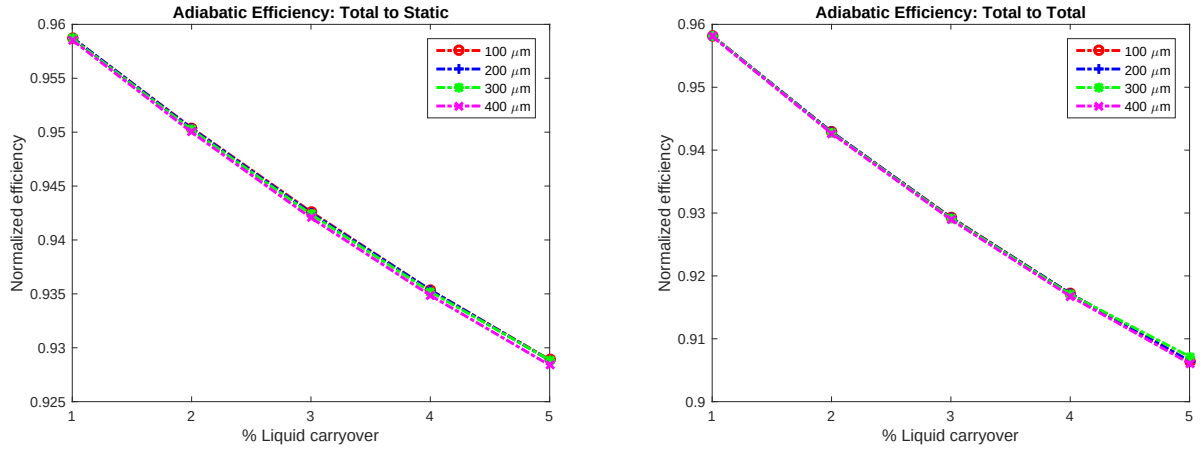

(a) Total to static

(b) Total to total

Figure 5.14: Overall adiabatic efficiency

5.5.4 Overall Polytropic Efficiency

From Figure 5.15, the total to static and total to total polytropic efficiencies are seen to decrease with increasing amount of liquid carryover. As compared to the adiabatic efficiencies, this detrimental effect is more pronounced. However, similar to the adiabatic efficiencies, the initial droplet size is observed to have very little effects.

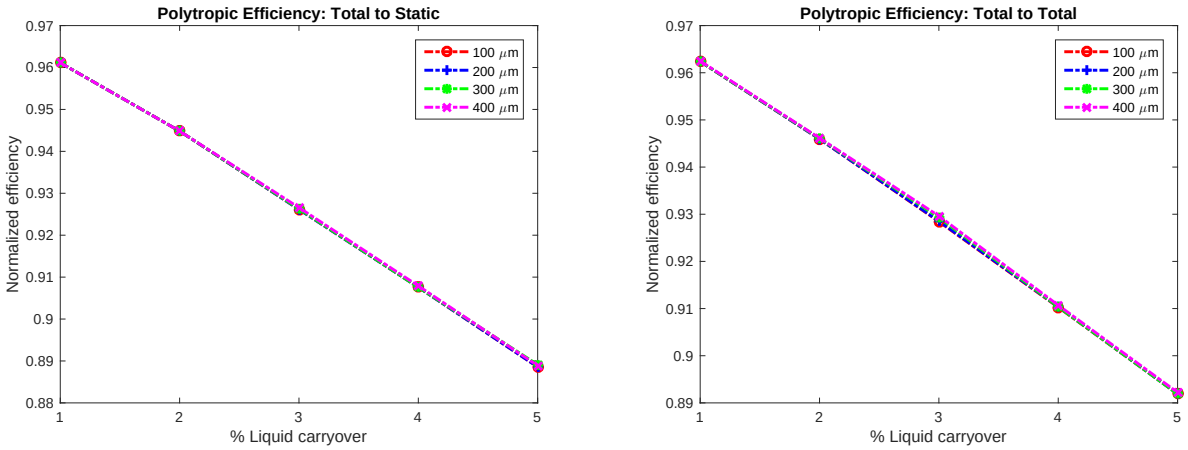

(a) Total to static

(b) Total to total

Figure 5.15: Overall polytropic efficiency

5.6 Discussions on the Compressor Performance

Figure 5.16 compares the relative flow angles (β_1, β_2) for Impeller 1 and 2 as well as the Return Channel vane. As reported in Chapter 4, negligible amount of liquid vaporizes in the Inlet domain. As a result, the flow conditions at the leading edge of Impeller 1 are not significantly different than the single phase flow case, thus, the variation in β_1 is negligible. However, liquid vaporization in the Impeller 1 passage increases the velocities (and therefore, the volumetric flow rate) near the blade trailing edge, thereby reducing the magnitudes of β_2. This indicates that the flow turning through Impeller 1 is lower as compared to the single phase flow case. The changes in the relative flow angles for the Return Channel vane and Impeller 2 blade can similarly be explained on the basis of changes in the flow velocities, as reported in Chapter 4. These observations indicate that both stages operate at off-design conditions.

Even though the overall flow turning through both impellers is lower, both stages are observed to consume more power. This can be attributed to the work done in vaporizing the liquid and the corresponding increase in the mass flow rate. The increase in entropy due to liquid vaporization

and mixing, and the off-design operation of the compressor result in decreasing the adiabatic and polytropic efficiencies. It can also be seen that the relative degradation in polytropic efficiencies is slightly greater as compared to that in the adiabatic efficiencies.

The reduction in the overall pressure ratios, increase in the net power input and the degradation in the overall adiabatic as well as polytropic efficiency indicate that the liquid carryover is detrimental for the operation of the compressor. This appears contradictory to the reported observations in the field of wet compression. However, it must be noted that the beneficial or detrimental effects of two-phase flow are highly dependent on the property relations of the fluids involved as well as the design and characteristics of the compressor. It is clear that for the two-phase flow cases analyzed in this research, the detrimental effects of liquid carryover dominate the beneficial effects of intercooling.

5.7 Effects of Two-Phase Flow on Aerodynamic Loading

The aerodynamic loading on the blades is another parameter of interest related to the working of the compressor. The blade loading on both impeller rotors and the Return Channel vane was calculated in terms of the pressure coefficient, given by Equation 5.9.

$$C_p = \frac{p - p_{ref}}{(\frac{1}{2}\rho U^2)_{ref}} \tag{5.9}$$

The reference values used to compute the pressure coefficients of each component were calculated at their respective inlet stations.

5.7.1 Aerodynamic Loading on the Blades

The aerodynamic blade loading plots at the midspan of Impeller 1 and 2 blades and the Return Channel vane are shown in Figure 5.17. For all three components, the pressure coefficients on both pressure and suction surfaces are seen to be lower under two-phase flow conditions. However, increasing amount of liquid carryover does not show any significant effect on the pressure coefficients. Similarly, the effects of initial droplet size are also observed to be negligible. These are shown in Appendix B. The blade loading plots near the hub and shroud for the two impellers and the Return Channel vane are also plotted in Appendix B.

5.7.2 Discussions on the Aerodynamic Blade Loading

The reduction in the pressure coefficient in the two-phase flow cases is consistent with the higher velocities and lower static pressures as reported previously. Since this reduction is similar on the pressure and suction surfaces of both impellers, the resultant change in the overall aerodynamic blade loading is expected to be negligible. However, greater reduction in pressure coefficient is observed on the suction surface side of the Return Channel vane, and hence, the aerodynamic blade loading around that region is likely to be higher.

5.8 Effects of Turbulent Dispersion of the Droplets

As noted in Chapter 2, the droplets cannot directly modulate the turbulence in the vapor phase. However, turbulence in the vapor phase may cause droplet dispersion. In the above reported investigations, droplet dispersion was neglected. To ascertain that this assumption does not con-

stitute a significant modeling error, a case with 1% liquid carryover and initial droplet size of 100 μm was analyzed by incorporating the turbulent dispersion of the droplets. As in the previous section, the performance parameters were normalized with the corresponding values from the single phase flow case. Table 5.1 shows the comparison of the cases with and without turbulent dispersion.

	Parameter	**Without Turbulent Dispersion**	**With Turbulent Dispersion**
Stage 1	Pressure ratio - Total to static	0.9879	0.9877
	Pressure ratio - Total to total	0.9888	0.9886
	Diffuser C_p	0.9871	0.9880
	Power input	1.0557	1.0507
Return Channel	Return Channel C_p	1.1845	1.1641
Stage 2	Pressure ratio - Total to static	0.9899	0.9905
	Pressure ratio - Total to total	0.9904	0.9910
	Diffuser C_p	0.9963	0.9929
	Power input	1.1105	1.1171
Overall	Pressure ratio - Total to static	0.9739	0.9745
	Pressure ratio - Total to total	0.9744	0.9750
	Power input	1.0321	1.0342

Table 5.1: Performance comparison with and without turbulent dispersion

The table shows that the effect of incorporating the turbulent dispersion is indeed negligible. As compared to Stage 1, the effects of turbulent droplet dispersion seem more pronounced for the Return Channel and Stage 2. This is expected, because the droplet size is relatively larger in Stage 1, and therefore the droplets are less likely to be influenced by turbulence. Including turbulent droplet dispersion results in difference of 0.062% in the overall total to static and total to total pressure ratios and 0.21% in power input. Because of these small differences, and considering the significant increase in computational resources required to incorporate turbulent dispersion (especially for higher percentage of liquid carryover) neglecting the turbulent dispersion of the droplets is justified in this research.

5.9 Comparison of Results Assuming Ideal Gas Behavior

Due to the relative simplicity of modeling and lower computational requirements, most multi-phase flow analyses available in literature assume ideal gas behavior. This implies that in addition to assuming the equation of state to follow the ideal gas equation, the properties of the materials are assumed to be constant or only temperature-dependent.

Since the compressor system in this research operates near the saturation curve of the working fluid (refrigerant R134a), the vapor phase is likely to exhibit significant deviation from ideal gas behavior. For example, the compressibility factor for R134a at the saturation temperature of 300 K is 0.8479. This indicates that in order to perform the two-phase flow analysis accurately, accounting for the real gas behavior of the vapor phase is necessary.

To understand the errors associated with ideal gas assumption, a single phase case and a two-phase case with 1% liquid carryover and initial droplet size of 100 μm were simulated. In both cases, the vapor phase was assumed to follow the ideal gas equation. Table 5.2 shows the results

for the single phase flow case. The results are normalized by the results of the single phase flow case assuming real gas behavior.

	Parameter	**Ideal Gas - Single Phase**
Stage 1	Pressure ratio - Total to static	0.9237
	Pressure ratio - Total to total	0.9200
	Diffuser C_p	0.9813
	Power input	0.8876
Return Channel	Return Channel C_p	1.3818
Stage 2	Pressure ratio - Total to static	0.8781
	Pressure ratio - Total to total	0.8697
	Diffuser C_p	1.0347
	Power input	0.9003
Overall	Pressure ratio - Total to static	0.8031
	Pressure ratio - Total to total	0.7954
	Power input	0.8782

Table 5.2: Performance comparison assuming ideal gas behavior for the single phase flow case

It can be clearly seen that the assumption of ideal gas behavior changes the results substantially. Comparing the single phase flow cases, the pressure ratios are significantly lower, whereas the Return Channel pressure coefficient shows a substantial increase. The input power, calculated

assuming ideal gas behavior, is also lower for both stages as well as the overall compressor.

Table 5.3 compares the two-phase flow calculations with ideal gas and real gas behavior. The first column of the table shows the normalized results of two-phase flow assuming ideal gas behavior. This normalization was performed on the basis of the single phase flow case with ideal gas behavior. The second column shows the corresponding normalized results assuming real gas behavior.

Table 5.3 reveals that some of the performance parameters show contradictory trends when the gas behavior is changed from ideal gas to real gas. For example, the pressure ratios for Stage 1 and the overall pressure ratios are higher for the two-phase flow case with the assumption of ideal gas behavior, as opposed to those with real gas behavior. Similarly, the Diffuser 1 and Return Channel pressure coefficients and Stage 2 power input show opposite trends.

Thus, it is clear that assumption of ideal gas behavior can lead to significant errors, and thereby to misleading conclusions. Therefore, validity of this assumption should be carefully examined prior to predicting the effects of two-phase flow on the compressor performance.

	Parameter	Effect of Two-Phase Flow - Ideal Gas	Effect of Two-Phase Flow - Real Gas
Stage 1	Pressure ratio - Total to static	1.0011	0.9879
	Pressure ratio - Total to total	1.0020	0.9888
	Diffuser C_p	1.0138	0.9871
	Power input	1.1100	1.0557
Return Channel	Return Channel C_p	0.9785	1.1845
Stage 2	Pressure ratio - Total to static	0.9959	0.9899
	Pressure ratio - Total to total	0.9981	0.9904
	Diffuser C_p	0.9766	0.9963
	Power input	0.9212	1.1105
Overall	Pressure ratio - Total to static	1.0019	0.9739
	Pressure ratio - Total to total	1.0020	0.9744
	Power input	1.0347	1.0551

Table 5.3: Effect of two-phase flow assuming ideal gas and real gas behavior

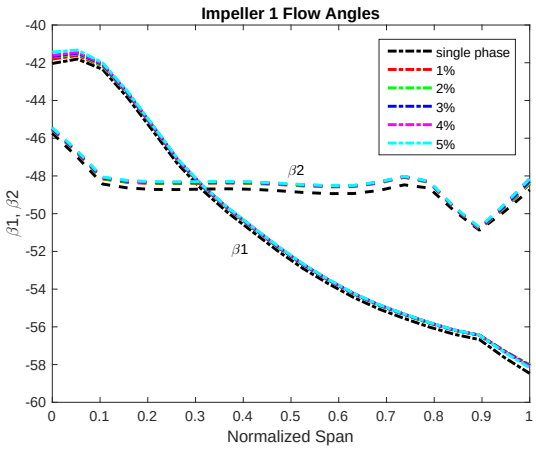

(a) Impeller 1

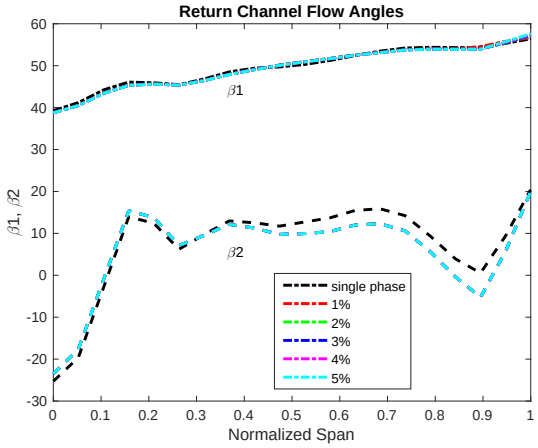

(b) Return Channel vane

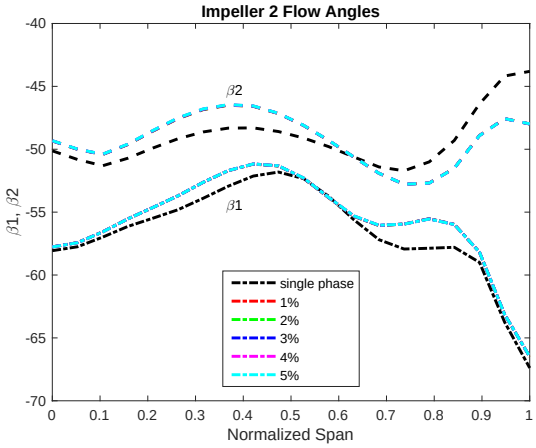

(c) Impeller 2

Figure 5.16: Comparison of relative flow angles β_1, β_2

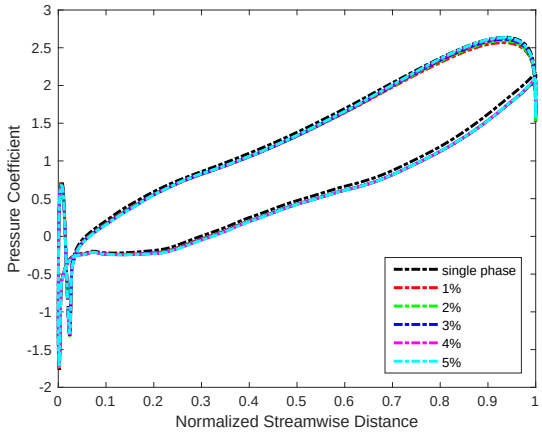

(a) Impeller 1 blade loading

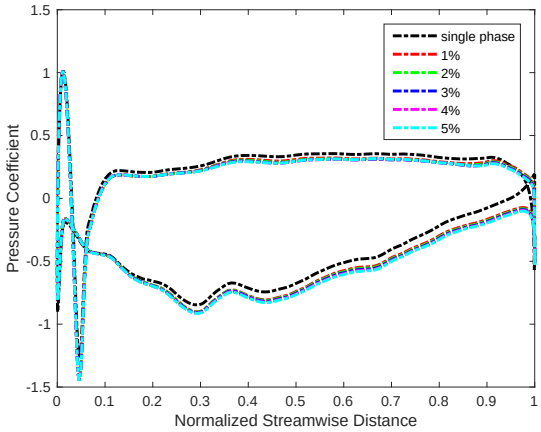

(b) Return Channel vane loading

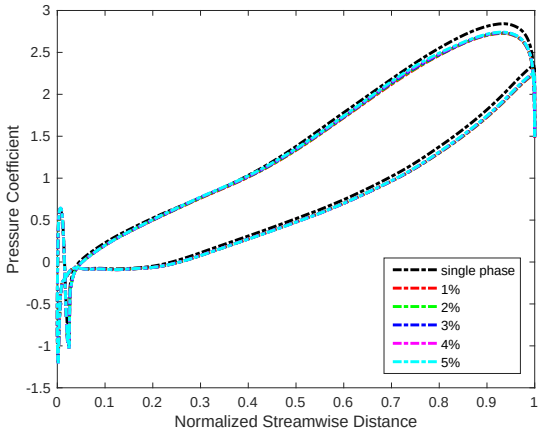

(c) Impeller 2 blade loading

Figure 5.17: Aerodynamic blade loading

Chapter 6

Erosion Predictions

Droplet impingement on the compressor surfaces can cause erosion of the surfaces. In this chapter, the surfaces where erosion is likely to occur are identified, and the potential erosion "hot-spots" on these surfaces are located. In addition, the cumulative rate of erosion on each surface is also estimated.

6.1 Surface Erosion Prediction

As explained in Chapter 2, a droplet-wall interactions model was implemented in this research to calculate the amount of material that can potentially get eroded from the compressor surfaces due to droplet impingement. This model was incorporated in the simulations through a particle user routine. This user routine computed the energy associated with the erosion process by solving the energy equation, , given by Equation 6.1, for each impinging droplet.

$$(E_{surface} + E_{kinetic})_{before\ impingement} = n\,(E_{surface} + E_{kinetic})_{after\ impingement} + E_{erosion} + E_{dissipation} \quad (6.1)$$

Where n is the number of secondary droplets formed as a result of the impingement. The volume of the material eroded was then estimated based on the surface energy of the material E_{sp}, as shown in Equation 6.2.

$$V_{erosion} = \frac{E_{erosion}}{E_{sp}} \quad (6.2)$$

6.2 Cumulative Erosion on Compressor Surfaces

The cumulative amount of erosion on the compressor surfaces was calculated for liquid carryover of 1% - 5% and initial droplet size of 100 μm - 400 μm. Figure 6.1 shows the cumulative erosion potential on all wall boundaries in the computational domain for the case corresponding to 5% liquid carryover and initial droplet size of 400 μm. Each number on the X axis corresponds to a specific surface (as shown in the figure). The Y axis shows the cumulative rate of erosion on that surface, normalized by the maximum value. Thus, the figure compares the relative amount of erosion that can potentially occur on all compressor surfaces.

The figure shows that the maximum erosion is likely to occur on Impeller 1 shroud. Impeller 1 blade is also likely to undergo considerable erosion. In addition, Impeller 1 hub, Diffuser 1 hub and the Return Channel shroud and vane are identified as the surfaces where erosion can

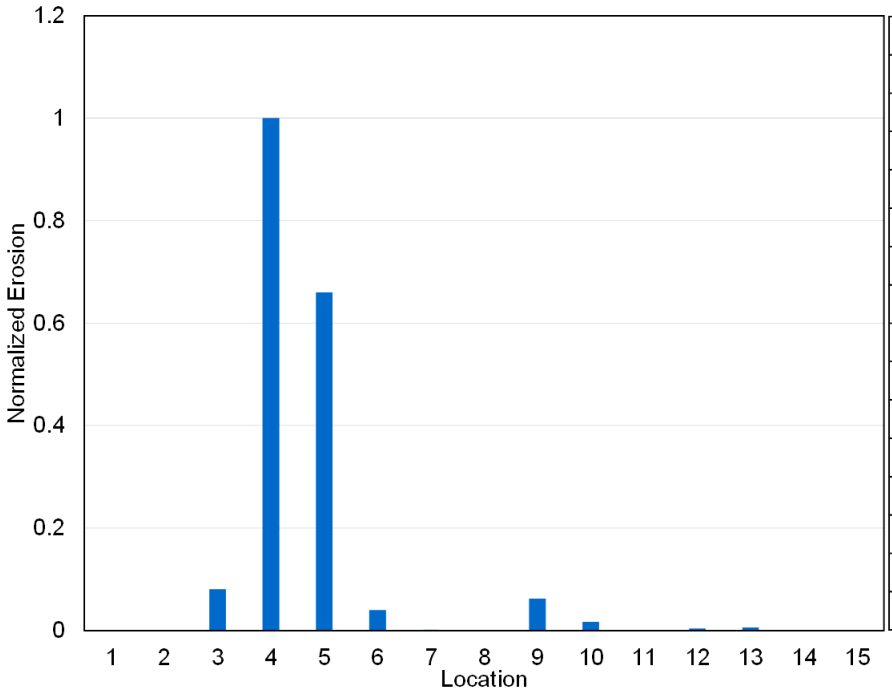

X Axis	Location
1	Inlet hub
2	Inlet shroud
3	Impeller 1 hub
4	Impeller 1 shroud
5	Impeller 1 blade
6	Diffuser 1 hub
7	Diffuser 1 shroud
8	Return Channel hub
9	Return Channel shroud
10	Return Channel vane
11	Impeller 2 hub
12	Impeller 2 shroud
13	Impeller 2 blade
14	Diffuser 2 hub
15	Diffuser 2 shroud

Figure 6.1: Net erosion on the compressor surfaces

potentially occur. However, the amount of erosion on these surfaces is estimated to be less than 10% of the maximum value. The rest of the surfaces in the compressor show negligible erosion potential.

These predictions track well with the droplet paths and dynamics, explained previously in Chapter 4. The droplets are not likely to impinge on the walls in the Inlet domain, resulting in prediction of negligible erosion. Within the Impeller 1 domain, the droplet impingement on the blade and the shroud results in prediction of relatively high amount of erosion. Similarly, in the Return Channel, erosion can potentially occur on the shroud surface and on the vane. It should be noted that the mass flow rate of the liquid also affects the volume of material that is eroded. Due to the reduced liquid mass flow rate in the Return Channel (due to vaporization), the estimated amount of erosion in this region is smaller. This also explains the negligible erosion potential seen in the Impeller 2 and Diffuser 2 domains.

Since the relative erosion on Impeller 1 hub, shroud and blade, Diffuser 1 hub and Return Channel shroud and vane was predicted to be significant, the effects of varying the liquid carryover and the initial droplet size were studied for these surfaces. The results of this analysis are presented in the following subsections.

6.2.1 Cumulative Erosion on Impeller 1 Hub, Shroud and Blade

Figure 6.2 shows the predicted amount of cumulative erosion on Impeller 1 hub, shroud and blade. As expected, the amount of erosion increases with increasing liquid carryover on all locations. On the shroud and the blade, the amount of erosion is seen to increase with increasing initial droplet size. This trend is especially noticeable for liquid carryover of 3%, 4% and 5%. This also indicates that droplet impingement on the shroud and the blade surfaces increases with increasing initial droplet size.

6.2.2 Cumulative Erosion on Diffuser 1 Hub

The predicted amount of cumulative erosion on the Diffuser 1 hub surface is shown in Figure 6.3. With increasing initial droplet size, the variation in amount of erosion is negligible. This indicates that the droplet impingement on the hub surface is not significantly affected by the initial droplet size. Also, the predicted amount of erosion is seen to increase with increasing liquid carryover, as explained previously.

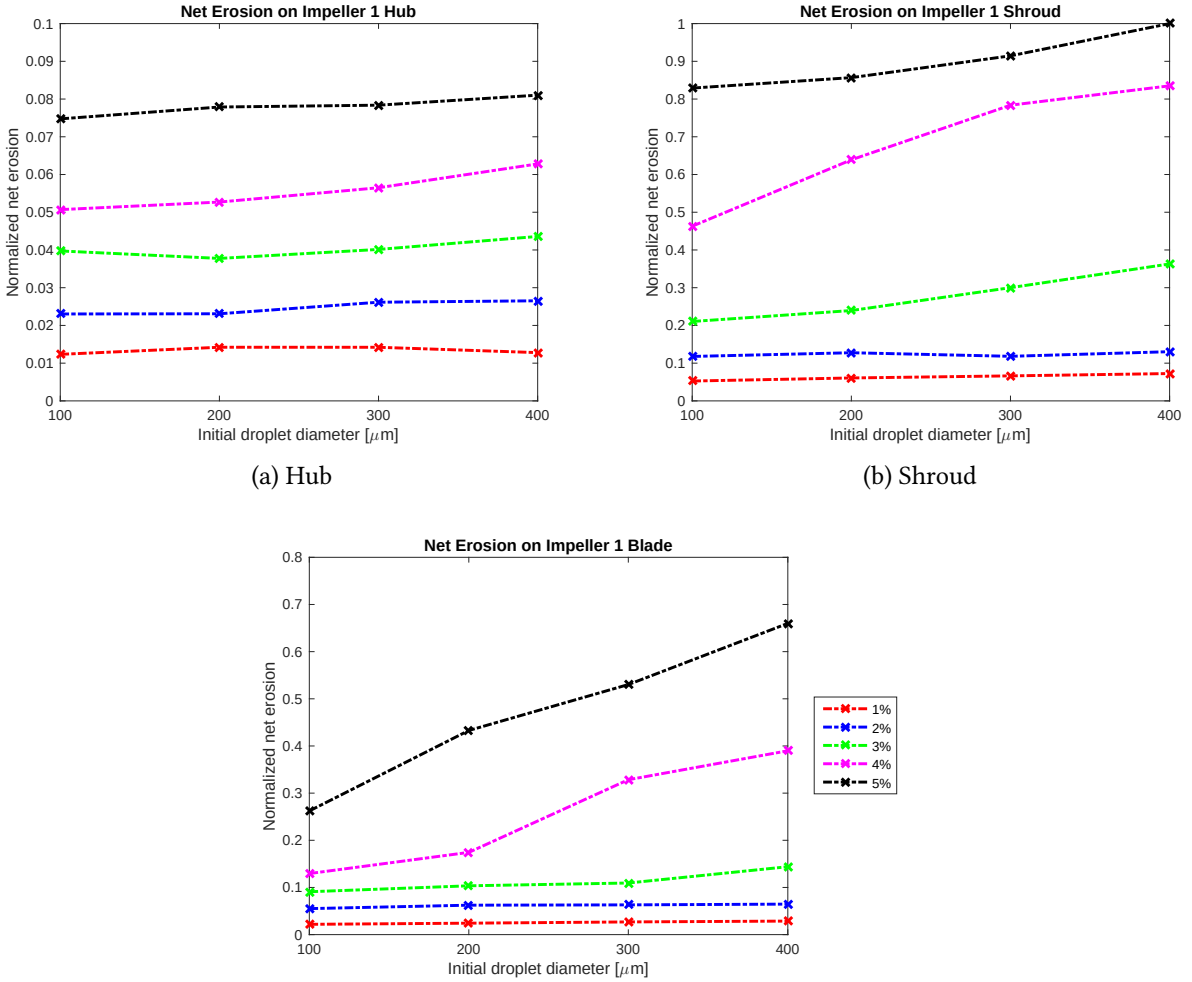

(a) Hub

(b) Shroud

(c) Blade

Figure 6.2: Total erosion on Impeller 1 surfaces

6.2.3 Cumulative Erosion on Return Channel Shroud and Vane

Figure 6.4 shows the predicted amount of cumulative erosion on the Return Channel shroud and vane. Similar to Diffuser 1, the amount of erosion is observed to increase with increasing liquid carryover. Also, the variation with increasing initial droplet size is not significant.

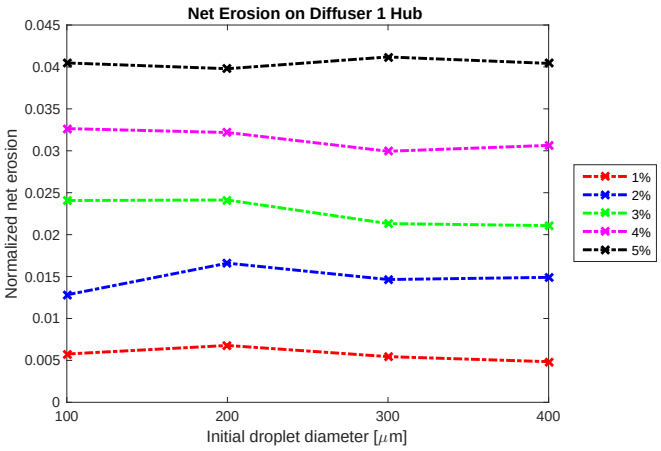

Figure 6.3: Total erosion on Diffuser 1 hub

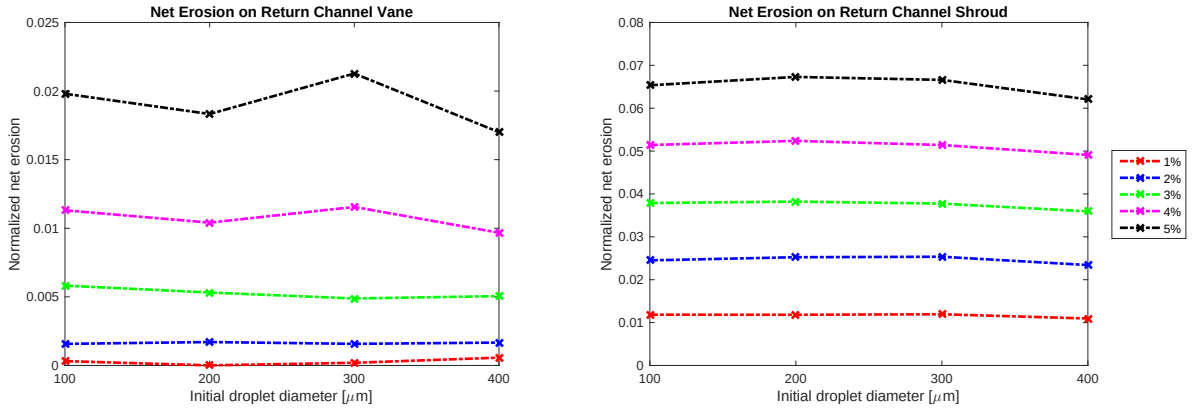

(a) Vane

(b) Shroud

Figure 6.4: Net erosion on Return Channel shroud

6.3 Erosion Locations

In addition to estimating the cumulative erosion, contours of the normalized erosion were plotted to identify potential erosion "hot-spots". The two-phase flow case with 5% liquid carryover and initial droplet size of 400 μm was used as a representative case to plot the contours.

6.3.1 Erosion Contours on Impeller 1 and Diffuser 1 Hub

The erosion contours on the hub surface of Impeller 1 and Diffuser 1 are shown in Figure 6.5. Within the blade passage, erosion is predicted to occur from the blade leading edge till approximately 40% of the chord. Downstream of the Impeller 1 blade, small areas of high erosion are likely to occur towards the pressure surface side of the blades. These areas are near the Impeller 1 - Diffuser 1 domain interface. It should be noted that this interface was defined as "Frozen Rotor" in the simulations, therefore the relative change in position between the rotating Impeller 1 domain and stationary Diffuser 1 domain was not accounted. However, in the physical system, the erosion pattern on the Diffuser 1 hub is likely to form a continuous band due to the relative motion between the Impeller 1 and Diffuser 1.

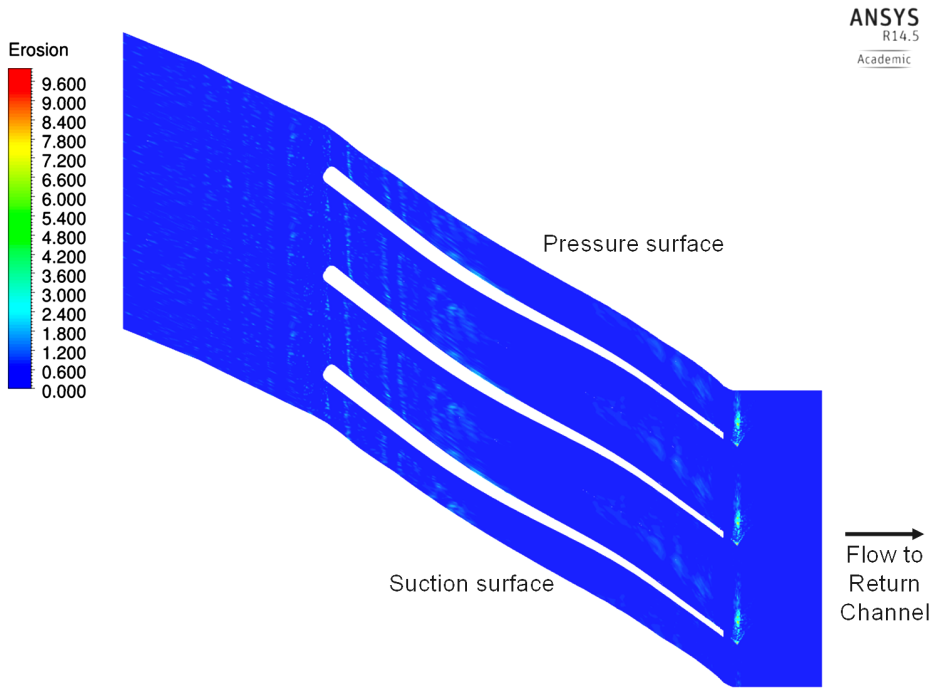

Figure 6.5: Impeller 1 and Diffuser 1 hub

6.3.2 Erosion Contours on Impeller 1 and Diffuser 1 Shroud

On the shroud surfaces, small regions of high erosion are likely to occur near the trailing edge of the impeller blade as seen in Figure 6.6. These areas are mainly towards the pressure surface side of the blades. However unlike on the hub, these areas lie on the Impeller 1 shroud, and therefore are likely to be localized. The simulation also predicts high amount of erosion in the area near the intersection of the blade pressure surface and the shroud. This is likely to occur due to the impingement of the droplets near the pressure surface that are centrifuged towards the shroud. The area within the blade passage and the Diffuser 1 shroud are likely to undergo negligible erosion.

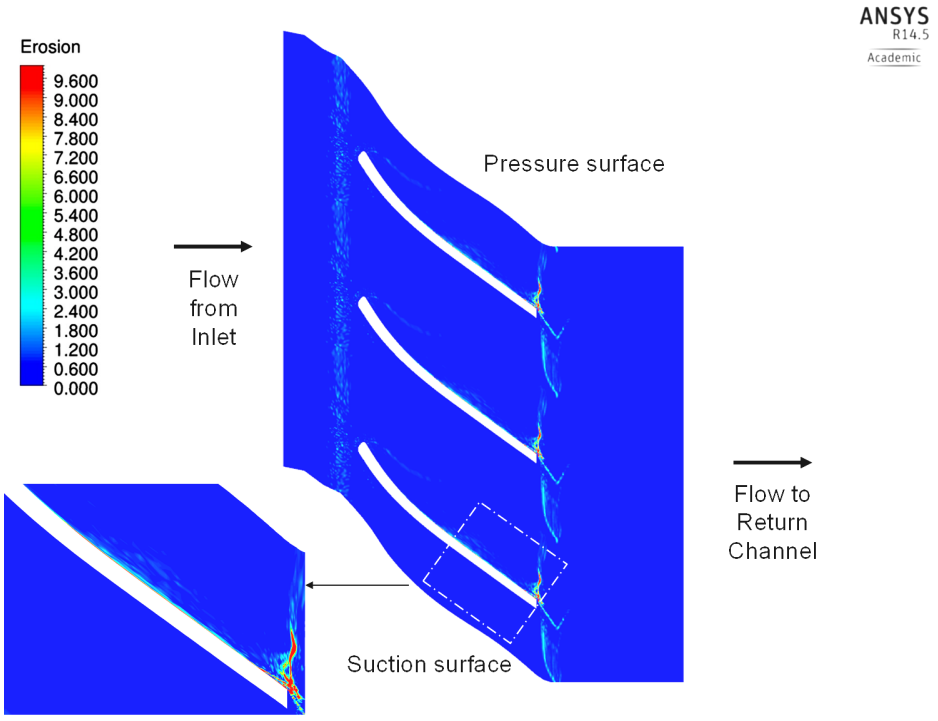

Figure 6.6: Impeller 1 and Diffuser 1 shroud

6.3.3 Erosion Contours on Impeller 1 Blade

On the Impeller 1 blade surface, erosion is likely to occur mostly on the pressure surface side, as shown in Figure 6.7. The potential erosion on the suction surface side is negligible. As expected, significant erosion is also predicted on the blade leading edge. On the pressure surface, most of the erosion is likely to occur between approximately 50% of the chord and the trailing edge, with high amount of erosion near the trailing edge. The figure also shows that the maximum erosion on the blade surface is predicted to occur in the area near the shroud, which is consistent with the erosion pattern observed on the Impeller 1 shroud.

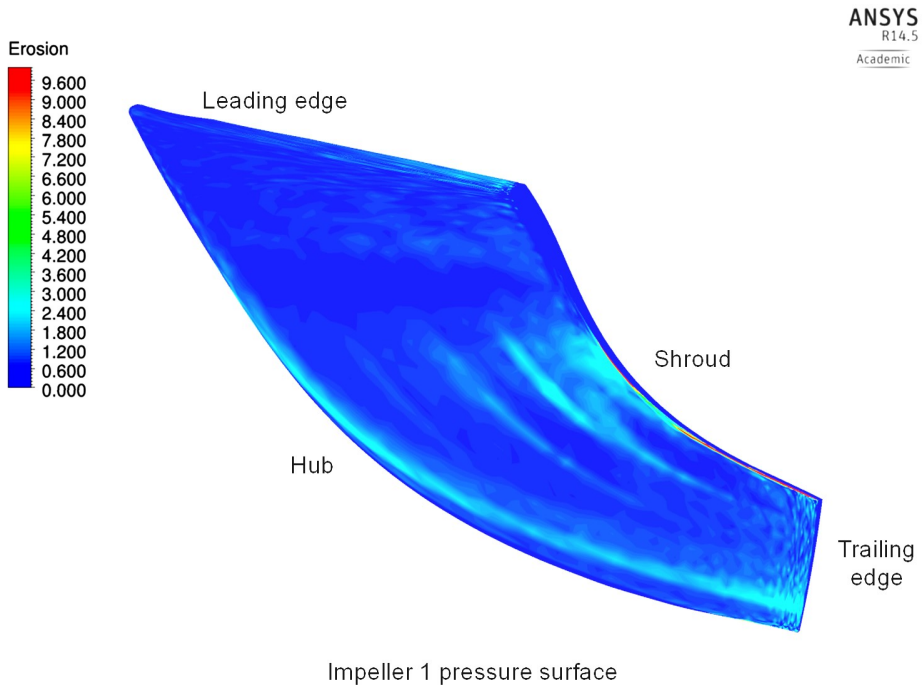

Figure 6.7: Erosion contours for Impeller 1 blade

6.3.4 Erosion Contours on Return Channel Shroud

Figure 6.8 shows the contours of predicted erosion on the Return Channel shroud surface. The figure shows that on this surface, erosion is likely to occur in the region immediately upstream of the Return Channel vane. This area lies downstream of the bend in the Return Channel and thus undergoes high amount of droplet impingement, as seen in Chapter 5. On the Return Channel vane, erosion is predicted to occur only on the leading edge, near the shroud surface.

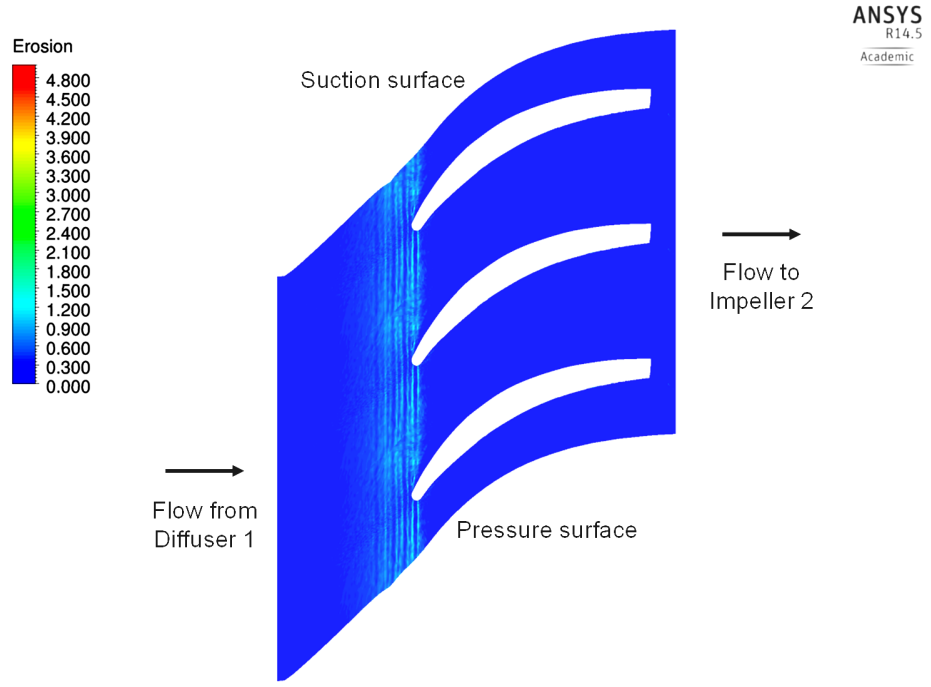

Figure 6.8: Erosion on Return Channel shroud

The above results show that the droplet-wall particle user routine can be implemented to identify regions on the compressor surfaces that are likely to undergo erosion, and to calculate the relative rate of potential erosion at these locations. Since it can take a long time for experimentally observable and measurable erosion to occur, this user routine can be used as a predictive tool to support improved design solutions for mitigating the erosion problem.

Chapter 7

Summary and Conclusions

The main goal of this work was to investigate the effects of two-phase flow on the operation of a multistage centrifugal compressor. The following objectives were set for this research:

1. Develop a CFD model that predicts the operation of a two-stage centrifugal compressor in two-phase flow conditions
2. Understand the droplet dynamics and vaporization, and compare the flow behavior in the compressor under single and two-phase flow conditions
3. Analyze and provide insights on the effects of the two-phase flow on the compressor performance
4. Identify the locations on the compressor surfaces where erosion, if any, is likely to occur and estimate the amount of eroded material
5. Based on the analysis, provide recommendations on the operating conditions in terms of liquid/vapor mass ratio and droplet size

This chapter summarizes the major findings of this research and provides recommendations for future work.

7.1 CFD Modeling

This work involved developing a unique and high fidelity CFD model that accounted for real gas behavior of the vapor phase in the two-phase flow conditions. This was accomplished by supplying a real gas property table to the CFD solver. The inability of the CFD solver to handle a liquid-real gas phase change was overcome by defining the vapor phase as a mixture of real gas and ideal gas.

To ensure accurate calculations of the interphase heat, mass and momentum transfer terms, user defined routines were developed. Droplet impact on the compressor surfaces was also handled through a novel user routine, which calculated the normal and parallel coefficients of restitution on the basis of the droplet impingement regime and also predicted number of secondary droplets in the case of splashing. In addition, an erosion model was developed and implemented to identify the potential erosion "hot spots" on the compressor components and to estimate the rate of surface erosion. The working of the user routines was validated by comparing the CFD simulations with the experimental results available in literature.

By specifying appropriate material properties, the user routines that were developed in this research can be adapted to handle multiphase flows involving a variety of fluids. This flexibility will allow the implementation of these user routines in a number of CFD simulations, for example, wet compression, methanol spray in air, etc.

7.2 Droplet Dynamics, Vaporization and Behavior of the Two-Phase Flow

The droplet tracks depicted the motion of the droplets within the compressor. Significant droplet impingement was observed near the leading edges of the impeller blades, whereas the suction surfaces showed negligible impingement. The droplets away from the blade surfaces were seen to follow the main flow path, but near the blade surfaces, small droplets were observed to be centrifuged towards the shroud. In the Return Channel, the droplets impinged on the shroud as they navigated the bend.

The droplet vaporization rate was observed to vary significantly along the streamwise direction. The Inlet domain showed negligible vaporization. High rates of vaporization were seen in the latter half of the Impeller 1 and near the entrance of the Return Channel domain, whereas Diffuser 1 showed relatively lower rates. Downstream of the Return Channel, the rate of vaporization remained almost constant. The variation in the rate of vaporization along the streamwise direction was similar for all cases; however, the mass of liquid vaporized in the compressor increased with increasing amount of liquid carryover. Also, cases with larger initial droplet size showed higher rate of vaporization downstream of the Return Channel.

The two-phase flow conditions resulted in reducing the static pressure and temperature and increasing the specific entropy and velocity, as compared to the single phase flow case. The impact of liquid carryover on the pressure and velocity field was greater as compared to the specific entropy and temperature fields. These results highlighted the changes in the flow field within the compressor due to liquid carryover.

7.3 Compressor Performance

The performance of Stage 1, Return Channel and Stage 2 as well as the entire compressor system under two-phase flows was analyzed. As a result of the changes in the flow field due to liquid carryover, both stages of the compressor operated at off-design conditions. This resulted in reducing the aerodynamic efficiency of the compressor. The effects of two-phase flow were more noticeable in Stage 2. Also, the effects of increasing the amount of liquid carryover were seen to be more significant as compared to the initial droplet size. Overall, the detrimental effects of liquid carryover dominated the beneficial effects of intercooling, resulting in performance degradation of the entire compressor system.

Due to the changes in flow field in two-phase flow conditions, the pressure coefficients on both suction and pressure surfaces of the blades of both impellers as well as the Return Channel vane were observed to be lower. Very small changes were seen in the overall aerodynamic blade loading on the impeller blades, however the Return Channel vane showed increase in the overall blade loading.

Turbulent dispersion of the droplets was seen to have negligible effects on the compressor performance. This justified neglecting the turbulent dispersion of droplets in the simulations. However, assuming ideal gas behavior for the vapor phase was seen to result in predicting contradictory effects on the performance. This showed that the assumption of ideal gas behavior constitutes a significant modeling error in the two-phase flow simulations and highlighted the importance of examining the validity of these simplifying assumptions.

7.4 Erosion Predictions

The results from the erosion calculation revealed that maximum erosion is likely to occur on the Impeller 1 shroud. Impeller 1 blade also showed significant erosion potential. On the other hand, the predicted amount of erosion on Impeller 1 hub, Diffuser 1 hub and Return Channel shroud and vane was relatively small. All other surfaces showed negligible erosion. These predictions tracked well with the droplet paths and dynamics.

The predicted rate of erosion on all surfaces increased with increasing amount of liquid carryover. Impeller 1 hub, shroud and blade showed increase in erosion rate with increasing initial droplet size; however, no clear trend could be identified for Diffuser 1 hub and the Return Channel shroud and vane.

The regions of Impeller 1 and Diffuser 1 hub and shroud that lie on the blade pressure surface side were identified as potential erosion "hot spots". Most of the erosion on Impeller 1 blade was predicted to occur near the leading edge and in the region near the shroud that fell between 50% chord and the trailing edge on the pressure surface. On the Return Channel shroud, the region downstream of the bend showed high erosion potential. Similarly, the Return Channel vane showed erosion potential on the leading edge near the shroud surface.

Thus, useful information about the relative erosion potential of the compressor surfaces was obtained and the likely erosion "hot spots" were identified through the implementation of the erosion model that was developed in this research. These results demonstrated the utility of this model as a predictive tool for supporting improvements in the design for reducing any potential erosion.

7.5 Recommendations on the Operating Conditions

In this research, the detrimental effects of liquid carryover dominated the beneficial effects of intercooling, resulting in performance degradation of the entire compressor system. For the intercooling effects to be dominant, the rate of liquid vaporization is required to be greater than the rate observed in this work. However, for a compression system that operates near the saturation conditions of the working fluid, the rate of vaporization is not likely to increase significantly, and hence the overall effect of liquid carryover on the compressor operation is likely to be detrimental. Therefore, it is recommended to reduce the amount of liquid carryover, and if possible, prevent it altogether.

For a given amount of liquid carryover, the effects of the initial droplet size on the overall performance were found to be negligible. However, for the cases with larger initial droplet size, the severity of the predicted erosion on the Impeller 1 blade, hub and shroud was more. Therefore, in case liquid carryover is not preventable, ingestion of larger droplets should be avoided.

7.6 Future Work

The following steps are suggested as future research work in this topic:

7.6.1 Improvements in the CFD Modeling

Although the CFD model implemented in this research is highly sophisticated, there is still scope for improving it further and addressing some of the limitations. Possible areas of improvements are outlined below:

1. Incorporating the effect of the particle phase on the turbulence: Since the particle source terms are not included in the turbulence equations, the current CFD model does not support turbulence modulation due the particle phase. Improvements in the current turbulence modeling capabilities are necessary to overcome this limitation.

2. Modeling the phase change between a real gas and liquid: To optimize the solver performance, the current CFD model requires the particle phase to be assigned only constant or temperature-dependent properties. As a consequence, modeling the phase change between a real gas and liquid is not possible. However, improvements in the computational resources will enable specifying real fluid properties for the liquid phase as well, and thereby support modeling the phase change between a real gas and liquid.

3. Higher order scheme for particle path calculations: The current CFD model calculates the droplet path using forward Euler integration. Although this scheme converges if the timesteps are sufficiently small, the accuracy of the particle path calculations can be ensured by implementing a higher order integration scheme.

4. Analysis of the unsteady flow behavior: The results presented in this dissertation were obtained by performing steady state numerical simulations. Transient simulations can be performed with this CFD model to understand the unsteady behavior of the flow as well as the droplets at the cost of greater computational time and resources.

7.6.2 Comparisons with Experimental Testing of the Compressor

The experimental testing of a compressor operating under two-phase flow conditions is challenging. Some of the difficulties in the experimental testing are mentioned below.

1. Since the operating conditions of the compressor fall near the saturation curve of the vapor, condensation can occur in the measurement probes. This will likely affect the readings. A detailed design of the experiment is required to mitigate this problem.

2. The liquid droplets can impinge on the probes and affect the readings, or even damage the sensors. This necessitates careful designing of the probes as well as identifying installation locations that minimize the probability of droplet impingement on the probes.

3. Installing a setup for tracking the liquid droplets will likely require modifications in the compressor system. It may not be feasible to make these modifications in an actual compressor.

Experimental data from an actual compressor will enable quantifying the accuracy of the CFD model and help in identifying areas where the model needs improvements. Therefore, in spite of the difficulties mentioned above, experimental testing of a multistage centrifugal compressor that is performed for the purpose of CFD validation is highly recommended to advance this research.

Bibliography

[1] Chaker, M., Meher-Homji, C. B., and Mee, T., 2002. "Inlet fogging of gas turbine engines: Part a - fog droplet thermodynamics, heat transfer and practical considerations". In ASME Turbo Expo 2002: Power for Land, Sea, and Air, American Society of Mechanical Engineers, pp. 413–428.

[2] Chaker, M., Meher-Homji, C. B., and Mee, T., 2002. "Inlet fogging of gas turbine engines: Part b - fog droplet sizing analysis, nozzle types, measurement and testing". In ASME Turbo Expo 2002: Power for Land, Sea, and Air, American Society of Mechanical Engineers, pp. 429–441.

[3] Chaker, M., Meher-Homji, C. B., and Mee, T., 2004. "Inlet fogging of gas turbine engines: Part iii - fog behavior in inlet ducts, computational fluid dynamics analysis, and wind tunnel experiments". *Journal of engineering for gas turbines and power,* **126**(3), pp. 571–580.

[4] Bhargava, R., and Meher-Homji, C., 2002. "Parametric analysis of existing gas turbines with inlet evaporative and overspray fogging". In ASME Turbo Expo 2002: Power for Land, Sea, and Air, American Society of Mechanical Engineers, pp. 387–401.

[5] Hill, P., 1963. "Aerodynamic and thermodynamic effects of coolant injection on axial compressors". *The Aeronautical Quarterly,* **14**(4), pp. 331–348.

[6] Horlock, J., 2001. "Compressor performance with water injection". In ASME Turbo

Expo 2001: Power for Land, Sea, and Air, American Society of Mechanical Engineers, pp. V001T03A039–V001T03A039.

[7] Khan, J. R., and Wang, T., 2008. "Simulation of inlet fogging and wet-compression in a single stage compressor including erosion analysis". In ASME Turbo Expo 2008: Power for Land, Sea, and Air, American Society of Mechanical Engineers, pp. 193–206.

[8] Khan, J. R., and Wang, T., 2011. "Three-dimensional modeling for wet compression in a single stage compressor including liquid particle erosion analysis". *Journal of Engineering for Gas Turbines and Power,* **133**(1), p. 012001.

[9] Obermueller, M., Schmidt, K., Schulte, H., and Peitsch, D., 2012. *Some Aspects on Wet Compression - Physical Effects and Modeling Strategies used in Engine Performance Tools*. Deutsche Gesellschaft fuer Luft-und Raumfahrt-Lilienthal-Oberth eV.

[10] Payne, R., and White, A., 2008. "Three-dimensional calculations of evaporative flow in compressor blade rows". *Journal of Engineering for Gas Turbines and Power,* **130**(3), p. 032001.

[11] White, A., and Meacock, A., 2003. "An evaluation of the effects of water injection on compressor performance". In ASME Turbo Expo 2003, collocated with the 2003 International Joint Power Generation Conference, American Society of Mechanical Engineers, pp. 181–189.

[12] White, A., and Meacock, A., 2011. "Wet compression analysis including velocity slip effects". *Journal of Engineering for Gas Turbines and Power,* **133**(8), p. 081701.

[13] Sun, L., Zheng, Q., Li, Y., Luo, M., and Bhargava, R. K., 2013. "Numerical simulation of a complete gas turbine engine with wet compression". *Journal of Engineering for Gas Turbines and Power,* **135**(1), p. 012002.

[14] Zheng, Q., Sun, Y., Li, S., and Wang, Y., 2002. "Thermodynamic analyses of wet compression process in the compressor of gas turbine". In ASME Turbo Expo 2002: Power for Land, Sea, and Air, American Society of Mechanical Engineers, pp. 487–496.

[15] Zheng, Q., Shao, Y., and Zhang, Y., 2006. "Numerical simulation of aerodynamic performances of wet compression compressor cascade". In ASME Turbo Expo 2006: Power for Land, Sea, and Air, American Society of Mechanical Engineers, pp. 857–865.

[16] Brun, K., Kurz, R., and Simmons, H. R., 2006. "Aerodynamic instability and life-limiting effects of inlet and interstage water injection into gas turbines". *Journal of engineering for gas turbines and power,* **128**(3), pp. 617–625.

[17] Matz, C., Cataldi, G., Kappis, W., Mundinger, G., Bischoff, S., Helland, E., and Ripken, M., 2010. "Prediction of evaporative effects within the blading of an industrial axial compressor". *Journal of Turbomachinery,* **132**(4), p. 041013.

[18] Sexton, W. R., and Sexton, M. R., 2003. "The effects of wet compression on gas turbine engine operating performance". In ASME Turbo Expo 2003, collocated with the 2003 International Joint Power Generation Conference, American Society of Mechanical Engineers, pp. 673–679.

[19] Williams, J., and Young, J. B., 2007. "Movement of deposited water on turbomachinery rotor blade surfaces". *Journal of turbomachinery,* **129**(2), pp. 394–403.

[20] Nikolaidis, T., Pilidis, P., Teixeira, J., and Pachidis, V., 2008. "Water film formation on an axial flow compressor rotor blade". In ASME Turbo Expo 2008: Power for Land, Sea, and Air, American Society of Mechanical Engineers, pp. 79–87.

[21] Sun, L., Zheng, Q., Luo, M., Li, Y., and Bhargava, R., 2011. "On the behavior of water droplets

when moving onto blade surface in a wet compression transonic compressor". *Journal of Engineering for Gas Turbines and Power,* **133**(8), p. 082001.

[22] Kang, J.-S., Cha, B.-J., and Yang, S.-S., 2006. "Thermodynamic and aerodynamic meanline analysis of wet compression in a centrifugal compressor". *Journal of mechanical science and technology,* **20**(9), pp. 1475–1482.

[23] Surendran, A., and Kim, H. D., 2014. "Effects of wet compression on the flow behavior of a centrifugal compressor: A cfd analysis". In ASME Turbo Expo 2014: Turbine Technical Conference and Exposition, American Society of Mechanical Engineers, pp. V02DT42A002–V02DT42A002.

[24] Tonini, S., and Cossali, G. E., 2014. "A novel vaporisation model for a single-component drop in high temperature air streams". *International Journal of Thermal Sciences,* **75**, pp. 194–203.

[25] Hubbard, G., Denny, V., and Mills, A., 1975. "Droplet evaporation: effects of transients and variable properties". *International Journal of Heat and Mass Transfer,* **18**(9), pp. 1003–1008.

[26] Young, J., 1995. "The fundamental equations of gas-droplet multiphase flow". *International journal of multiphase flow,* **21**(2), pp. 175–191.

[27] Dushin, V., Kulchitskiy, A., Nerchenko, V., Nikitin, V., Osadchaya, E., Phylippov, Y. G., and Smirnov, N., 2008. "Mathematical simulation for non-equilibrium droplet evaporation". *Acta Astronautica,* **63**(11), pp. 1360–1371.

[28] Renksizbulut, M., and Yuen, M., 1983. "Experimental study of droplet evaporation in a high-temperature air stream". *Journal of heat transfer,* **105**(2), pp. 384–388.

[29] Ranz, W., and Marshall, W., 1952. "Evaporation from drops". *Chemical Engineering Progress,* **48**(3), p. 141446.

[30] Chiang, C., Raju, M., and Sirignano, W., 1992. "Numerical analysis of convecting, vaporizing fuel droplet with variable properties". *International journal of heat and mass transfer,* **35**(5), pp. 1307–1324.

[31] Schmehl, R., Rosskamp, H., Willmann, M., and Wittig, S., 1999. "Cfd analysis of spray propagation and evaporation including wall film formation and spray-film interactions". *International Journal of Heat and Fluid Flow,* **20**(5), pp. 520–529.

[32] Sun, H., Bai, B., and Zhang, H., 2014. "Comparative investigation on droplet evaporation models for modeling spray in cross-flow". *Heat Transfer Engineering,* **35**(6-8), pp. 664–673.

[33] Sazhin, S. S., 2006. "Advanced models of fuel droplet heating and evaporation". *Progress in energy and combustion science,* **32**(2), pp. 162–214.

[34] Abramzon, B., and Sirignano, W., 1989. "Droplet vaporization model for spray combustion calculations". *International journal of heat and mass transfer,* **32**(9), pp. 1605–1618.

[35] Miller, R. S., Harstad, K., and Bellan, J., 1998. "Evaluation of equilibrium and non-equilibrium evaporation models for many-droplet gas-liquid flow simulations". *International Journal of Multiphase Flow,* **24**(6), pp. 1025–1055.

[36] Zhifu, Z., Guoxiang, W., Bin, C., Liejin, G., and Yueshe, W., 2013. "Evaluation of evaporation models for single moving droplet with a high evaporation rate". *Powder technology,* **240**, pp. 95–102.

[37] Crowe, C. T., 2005. *Multiphase flow handbook*, Vol. 59. CRC press.

[38] Crowe, C. T., Schwarzkopf, J. D., Sommerfeld, M., and Tsuji, Y., 2011. *Multiphase flows with droplets and particles.* CRC press.

[39] Oberkampf, W. L., and Roy, C. J., 2010. *Verification and validation in scientific computing*. Cambridge University Press.

[40] Bai, C., and Gosman, A., 1995. Development of methodology for spray impingement simulation. Tech. rep., SAE.

[41] Bai, C., Rusche, H., and Gosman, A., 2002. "Modeling of gasoline spray impingement". *Atomization and Sprays,* **12**(1-3).

[42] Lesser, M., 1995. "Thirty years of liquid impact research: a tutorial review". *Wear,* **186**, pp. 28–34.

[43] Park, K., and Watkins, A., 1996. "Comparison of wall spray impaction models with experimental data on drop velocities and sizes". *International journal of heat and fluid flow,* **17**(4), pp. 424–438.

[44] Yarin, A., 2006. "Drop impact dynamics: splashing, spreading, receding, bouncing". *Annu. Rev. Fluid Mech.,* **38**, pp. 159–192.

[45] Cossali, G. E., Marengo, M., and Santini, M., 2005. "Single-drop empirical models for spray impact on solid walls: a review". *Atomization and Sprays,* **15**(6).

[46] Roisman, I., Araneo, L., Marengo, M., and Tropea, C., 1999. "Evaluation of drop impingement models: experimental and numerical analysis of a spray impact". In Thirteenth Annual Conference on Liquid Atomization and Spray Systems ILASS-Europe, Florence, Italy.

[47] Finnie, I., 1960. "Erosion of surfaces by solid particles". *Wear,* **3**(2), pp. 87–103.

[48] Grant, G., and Tabakoff, W., 1975. "Erosion prediction in turbomachinery resulting from environmental solid particles". *Journal of Aircraft,* **12**(5), pp. 471–478.

[49] Hamed, A., Tabakoff, W., and Wenglarz, R., 2006. "Erosion and deposition in turbomachinery". *Journal of Propulsion and Power,* **22**(2), pp. 350–360.

[50] Li, N., Zhou, Q., Chen, X., Xu, T., Hui, S., and Zhang, D., 2008. "Liquid drop impact on solid surface with application to water drop erosion on turbine blades, part i: Nonlinear wave model and solution of one-dimensional impact". *International Journal of Mechanical Sciences,* **50**(10), pp. 1526–1542.

[51] Zhou, Q., Li, N., Chen, X., Xu, T., Hui, S., and Zhang, D., 2008. "Liquid drop impact on solid surface with application to water drop erosion on turbine blades, part ii: Axisymmetric solution and erosion analysis". *International Journal of Mechanical Sciences,* **50**(10), pp. 1543–1558.

[52] Lee, B.-E., Riu, K.-J., Shin, S.-H., and Kwon, S.-B., 2003. "Development of a water droplet erosion model for large steam turbine blades". *KSME international journal,* **17**(1), pp. 114–121.

[53] Oka, Y., Mihara, S., and Miyata, H., 2007. "Effective parameters for erosion caused by water droplet impingement and applications to surface treatment technology". *Wear,* **263**(1), pp. 386–394.

[54] Kamkar, N., Bridier, F., Bocher, P., and Jedrzejowski, P., 2013. "Water droplet erosion mechanisms in rolled ti–6al–4v". *Wear,* **301**(1), pp. 442–448.

[55] ANSYS, 2012. "Ansys-solver theory guide". *Release, 14.5.*

[56] Menter, F. R., 1994. "Two-equation eddy-viscosity turbulence models for engineering applications". *AIAA journal,* **32**(8), pp. 1598–1605.

[57] Bardina, J., Huang, P., and Coakley, T., 1997. "Turbulence modeling validation". *AIAA paper,* **2121**, p. 1997.

[58] Lemmon, E., Huber, M., and McLinden, M., 2013. Nist standard reference database 23: Reference fluid thermodynamic and transport properties-refprop, version 9.1. National Institute of Standards and Technology, Standard Reference Data Program, Gaithersburg.

[59] Tillner-Roth, R., and Baehr, H. D., 1994. "An international standard formulation for the thermodynamic properties of 1, 1, 1, 2-tetrafluoroethane (hfc-134a) for temperatures from 170 k to 455 k and pressures up to 70 mpa". *Journal of Physical and Chemical Reference Data,* **23**(5), pp. 657–729.

[60] Wang, Q., Squires, K., Chen, M., and McLaughlin, J., 1997. "On the role of the lift force in turbulence simulations of particle deposition". *International Journal of Multiphase Flow,* **23**(4), pp. 749–763.

[61] Elghobashi, S., and Truesdell, G., 1992. "Direct simulation of particle dispersion in a decaying isotropic turbulence". *Journal of Fluid Mechanics,* **242**, pp. 655–700.

[62] Liu, A. B., Mather, D., and Reitz, R. D., 1993. Modeling the effects of drop drag and breakup on fuel sprays. Tech. rep., DTIC Document.

[63] Reid, R. C., Prausnitz, J. M., and Poling, B. E., 1987. *The properties of gases and liquids.* McGraw Hill Book Co., New York, NY.

[64] Tanner, F. X., 2004. "Development and validation of a cascade atomization and drop breakup model for high-velocity dense sprays". *Atomization and sprays,* **14**(3).

[65] Bai, B.-F., Zhang, H.-B., Liu, L., and Sun, H.-J., 2009. "Experimental study on turbulent mixing of spray droplets in crossflow". *Experimental Thermal and Fluid Science,* **33**(6), pp. 1012–1020.

[66] Bai, B., Sun, H., Zhang, H., and Liu, L., 2011. "Numerical study on turbulent mixing of spray droplets in crossflow". *Journal of Propulsion and Power,* **27**(1), pp. 132–143.

[67] Hundseid, O., Bakken, L. E., and Helde, T., 2006. "A revised compressor polytropic performance analysis". In ASME Turbo Expo 2006: Power for Land, Sea, and Air, American Society of Mechanical Engineers, pp. 617–624.

[68] Schultz, J. M., 1962. "The polytropic analysis of centrifugal compressors". *Journal of Engineering for Power,* **84**(1), pp. 69–82.

[69] Mallen, M., and Saville, G., 1977. "Polytropic processes in the performance prediction of centrifugal compressors". *Institution of Mechanical Engineers: London, UK*, pp. 89–96.

[70] Huntington, R., 1985. "Evaluation of polytropic calculation methods for turbomachinery performance". *Journal of Engineering for gas Turbines and Power,* **107**(4), pp. 872–876.

Appendix A

Calculation of Input Power, Adiabatic Efficiency and Polytropic Efficiency

The compressor performance parameters can be calculated by simplifying the computational domain as shown in Figure A.1. For the calculations, the gaseous phase is assumed to enter at the inlet of the domain with mass flow rate $\dot{m}_{1,g}$ and at p_1, $T_{1,g}$, $s_{1,g}$ and $h_{01,g}$. The liquid droplets are assumed to enter with mass flow rate $\dot{m}_{1,f}$ and at $T_{1,f}$, $s_{1,f}$ and $h_{01,f}$. The temperature of the vapor and the liquid phase is assumed to be the same at the inlet, i.e. $T_{1,g} = T_{1,f}$.

Similarly, at the outlet of the computational domain, the gas mass flow rate is assumed to be $\dot{m}_{2,g}$ and at p_2, $T_{2,g}$, $s_{2,g}$ and $h_{2,g}$. The mass flow rate of the liquid droplets is assumed to be $\dot{m}_{2,f}$ and at $T_{2,f}$, $s_{2,f}$ and $h_{02,f}$. All wall boundaries are assumed to be adiabatic, which is consistent with the assumptions in the CFD simulations. Therefore, the heat interactions across the wall boundaries that result in entropy exchange between the system and the surroundings are not considered. The compressor is assumed to interact with the system through only a work interaction and therefore

does not exchange entropy with the system.

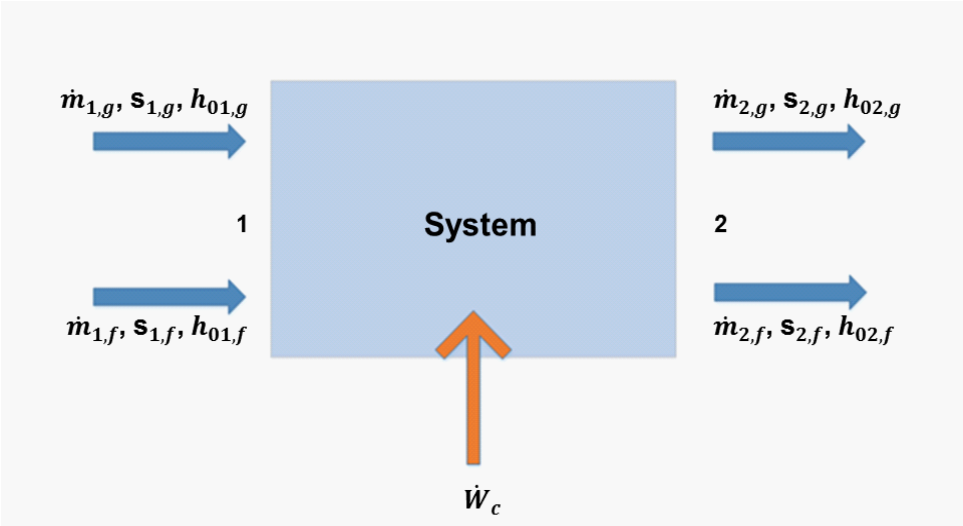

Figure A.1: System for calculating compressor performance

A.1 Calculation of Power

The compressor power can be calculated by writing the energy balance equation for the system, shown in Equation A.1.

$$\frac{dE}{dt} = \dot{W}_c + \sum_i \dot{m}_i h_i \tag{A.1}$$

At steady state, the above equation simplifies to Equation A.2.

$$\dot{W}_c = -\sum_i \dot{m}_i h_i = \dot{m}_{2,g} h_{02,g} + \dot{m}_{2,f} h_{02,f} - (\dot{m}_{1,g} h_{01,g} + \dot{m}_{1,f} h_{01,f}) \tag{A.2}$$

Thus, the total enthalpies of both phases at station 1 and station 2 are needed for calculating the compressor power. For the vapor phase, the total enthalpy is calculated by using the property

relations as shown in Equation A.3.

$$h_{0,g} = h_{0,g}(T_0, p_0) \tag{A.3}$$

For the liquid phase, the total enthalpy is calculated by using Equation A.4

$$h_{0,f} = h_f(T, p) + \frac{1}{2}U_f^2 \tag{A.4}$$

Note that this calculation also accounts for the enthalpy of vaporization since $\dot{m}_{1,g} \neq \dot{m}_{2,g}$.

A.2 Calculation of Adiabatic Efficiencies

To calculate the adiabatic efficiency, the entropy balance equation, given by Equation A.5 is used.

$$\frac{dS}{dt} = \dot{S}_{irr} + \sum_i \dot{m}_i s_i \tag{A.5}$$

At steady state, the above equation can be written as shown in Equation A.6.

$$\dot{S}_{irr} = -\sum_i \dot{m}_i s_i = \dot{m}_{2,g} s_{2,g} + \dot{m}_{2,f} s_{2,f} - (\dot{m}_{1,g} s_{1,g} + \dot{m}_{1,f} s_{1,f}) \tag{A.6}$$

The term $\dot{S}_{irr}$ in the above equation also includes the change in entropy due to vaporization of the liquid droplets.

The amount of liquid vaporized can be written as shown Equation A.7

$$\Delta\dot{m} = \dot{m}_{1,f} - \dot{m}_{2,f} = \dot{m}_{2,g} - \dot{m}_{1,g} \tag{A.7}$$

Therefore, the Equation A.6 can be simplified to Equation A.8.

$$\dot{S}_{irr} = \dot{m}_{1,g}(s_{2,g} - s_{1,g}) + \dot{m}_{1,f}(s_{2,f} - s_{1,f}) + \Delta\dot{m}(s_{2,g} - s_{2,f}) \tag{A.8}$$

Now, in an optimum compression process involving two-phase flow, the irreversibilities occurring within the system will be due to the phase change process only. Assuming that the same amount of liquid is vaporized in the optimum process, the entropy rise due to the phase change process can be estimated by the term $\Delta\dot{m}(s_{2,g} - s_{2,f})$. Therefore, in an optimum two-phase compression process,

$$\dot{S}_{irr} - \Delta\dot{m}(s_{2,g} - s_{2,f}) = 0$$

Using this in Equation A.8,

$$\dot{m}_{1,g}(s_{2,g,s} - s_{1,g}) + \dot{m}_{1,f}(s_{2,f,s} - s_{1,f}) = 0$$

Therefore,

$$s_{2,g,s} = s_{1,g} - \frac{\dot{m}_{1,f}}{\dot{m}_{1,g}}(s_{2,f,s} - s_{1,f})$$

Assuming that the difference in the liquid specific entropy between an optimum and the actual process is negligible, i.e. $s_{2,f,s} \approx s_{2,f}$, the above equation can be written as Equation A.9.

$$s_{2,g,s} = s_{1,g} - \frac{\dot{m}_{1,f}}{\dot{m}_{1,g}}(s_{2,f} - s_{1,f}) \tag{A.9}$$

$T_{2,g,s}$ can be then calculated from Equation A.10.

$$s_{2,g} - s_{2,g,s} = \int_{T_{2,s}}^{T_2} (\frac{c_p(T,p)}{T})_{p_2} \, dT \tag{A.10}$$

$T_{02,g,s}$ can be calculated by following a similar procedure.

Using the above values of $T_{2,g,s}$ and $T_{02,g,s}$ $H_{2,s}(T_{2,g,s}, p_2)$ and $H_{02,s}(T_{02,g,s}, p_2)$ can be calculated.

Total to static adiabatic efficiency can then be calculated by using Equation A.11.

$$\eta_{ts} = \frac{H_{2,s} - H_{01}}{H_{02} - H_{01}} \tag{A.11}$$

Similarly, total to total adiabatic efficiency can be calculated by using Equation A.12.

$$\eta_{tt} = \frac{H_{02,s} - H_{01}}{H_{02} - H_{01}} \tag{A.12}$$

A.3 Calculation of Polytropic Efficiencies

The procedure implemented for calculating the polytropic efficiencies uses a direct integration method, similar to the one reported in [67]. The step-by-step procedure is given below.

A.3.1 Computation Procedure Steps

The computation requires dividing the entire compression process into a number of small compression steps with equal pressure ratio. A constant initial value of polytropic efficiency η_p is assumed for all compression steps. For each compression step (i.e. from state 1- state 2):

1. Knowing p_1 and T_1, $h_1(T_1, p_1)$ and $s(T_1, p_1)$ can be calculated at the start of the integration step.

2. Using s and p_2, $h_{2s}(s, p_2)$ can be calculated. This gives the isentropic enthalpy rise dh_s in the compression step.

3. From the definition of polytropic efficiency, the actual enthalpy rise in the compression step is given by $dh = \frac{dh_s}{\eta_p}$. Using the assumed value of η_p, h_2 i.e. the enthalpy at state 2 can be calculated.

4. Knowing h_2 and p_2, the temperature $T_2(h_2, p_2)$ and entropy $s_2(h_2, p_2)$ at state 2 can be calculated.

5. Thus the properties at the end of the first integration step are known. The same procedure can now be repeated for the subsequent compression steps.

6. The temperature and pressure computed at state 2 of the final compression step correspond to the outlet conditions of the compressor. Note that the calculated temperature from the

above procedure depends on the initially assumed value of η_p. The calculated temperature will match the actual outlet temperature only when the value of η_p is equal to the actual value of the polytropic efficiency. In this calculation, bisection method is employed to find the value of η_p that gives the outlet temperature within a set error criterion (0.001 K) of the actual outlet temperature. The value of η_p thus calculated is then the correct polytropic efficiency of the compressor.

A.3.2 Additional Remarks on the Calculation Procedure

The real gas properties in the above procedure are computed using NIST REFPROP program [58, 59]. The REFPROP program can calculate properties of a liquid-vapor mixture that is in thermal and phase equilibrium, and thus the above procedure can be used for two-phase flow conditions. In this research, the two phases are not always in thermal / phase equilibrium. However, the properties of both phases for each small compression step cannot be obtained directly from the CFD data. Also, for small departure from equilibrium conditions, the error in the property calculation of the two-phase mixture can be assumed to be negligible.

It should also be noted that the commonly used approximate methods of calculating polytropic efficiency such as the Schultz method [68], Mallen method [69] or the Huntington method [70] are valid for gaseous phase only. Therefore, the method used in this research can be considered to be more accurate for computing the polytropic efficiency in two-phase flow conditions.

Appendix B

Blade Loading on Impeller 1, Impeller 2 and Return Channel Vane

The effects of increasing liquid carryover from 1% to 5%, as well as increasing the initial droplet size from 100 μm to 400 μm on the aerodynamic blade loading of both impellers and the Return Channel vane were studied. The variation with liquid carryover was analyzed for an initial droplet size of 400 μm, while the variation with initial droplet size was analyzed for liquid carryover of 5%.

B.0.1 Impeller 1 Aerodynamic Blade Loading

The comparison of Impeller 1 blade loading near the hub, midspan and the shroud is shown in Figure B.1. In the two-phase flow cases, the pressure coefficients at all three locations are seen to be slightly lower for both pressure and suction surfaces. Increasing liquid carryover and initial

droplet size do not show any significant effects on the pressure coefficients.

B.0.2 Return Channel Vane Aerodynamic Blade Loading

The pressure coefficients at all three locations are slightly lower for both pressure and suction surfaces in case of two-phase flow, as seen from Figure B.2. The difference is more pronounced on the suction surface, especially near the trailing edge (streamwise distance of 0.9 - 1) near the shroud. As before, increasing liquid carryover or the initial droplet size do not show any noticeable effects on the Return Channel blade loading.

B.0.3 Impeller 2 Aerodynamic Blade Loading

Figure B.3 shows the comparison of Impeller 2 blade loading. Again, the pressure coefficients at all three locations are slightly lower for both pressure and suction surfaces in case of two-phase flow, especially near the trailing edge. As with previous cases, increasing liquid carryover or the initial droplet size does not seem to affect Impeller 2 blade loading.

B.0.4 Discussions on the Aerodynamic Blade Loading

Figures B.1, B.2, and B.3 show that the pressure coefficients at the hub, midspan and shroud of both impellers and the Return Channel vane show similar trends, i.e. slight reduction from the single phase flow case. The change in overall aerodynamic blade loading on both impeller blades is observed to be negligible, however, the loading on the Return Channel vane is likely to be higher, especially near the trailing edge. Also, the impact of increasing the amount of liquid

carryover as well as varying the initial droplet size is seen to be negligible.

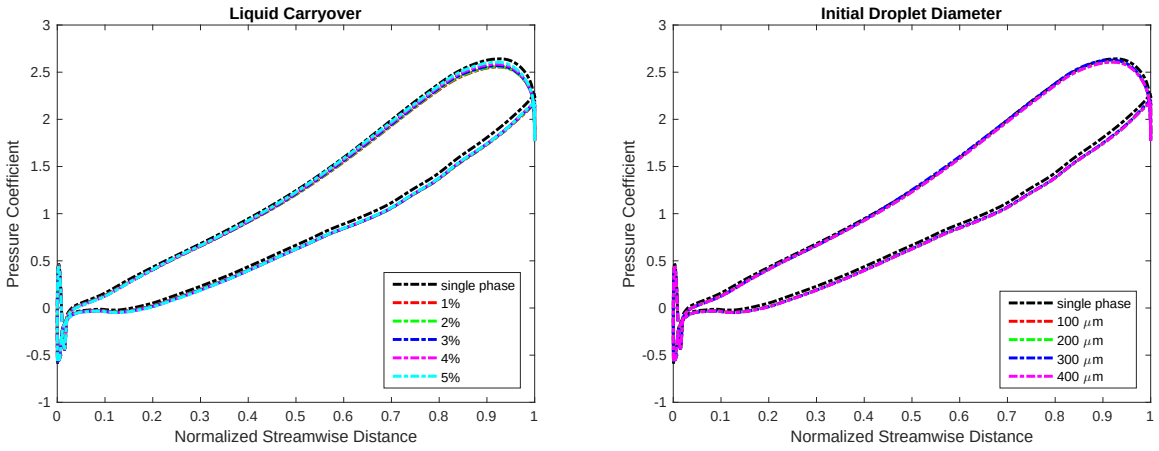

(a) Blade loading near hub

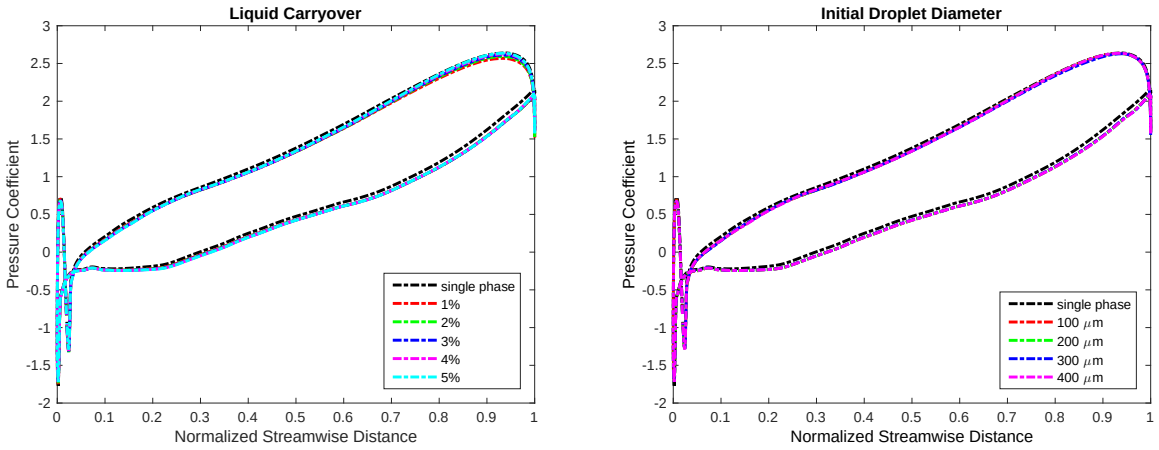

(b) Blade loading near midspan

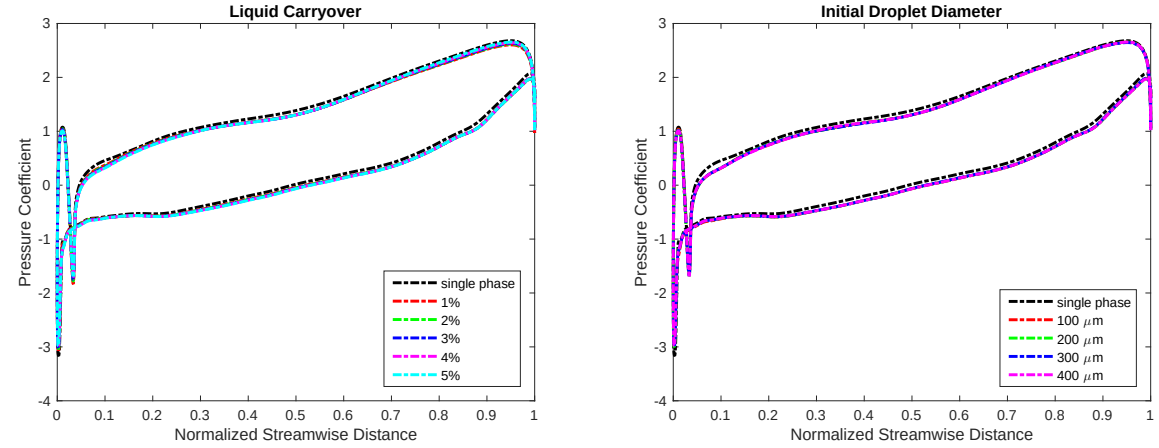

(c) Blade loading near shroud

Figure B.1: Impeller 1 blade loading

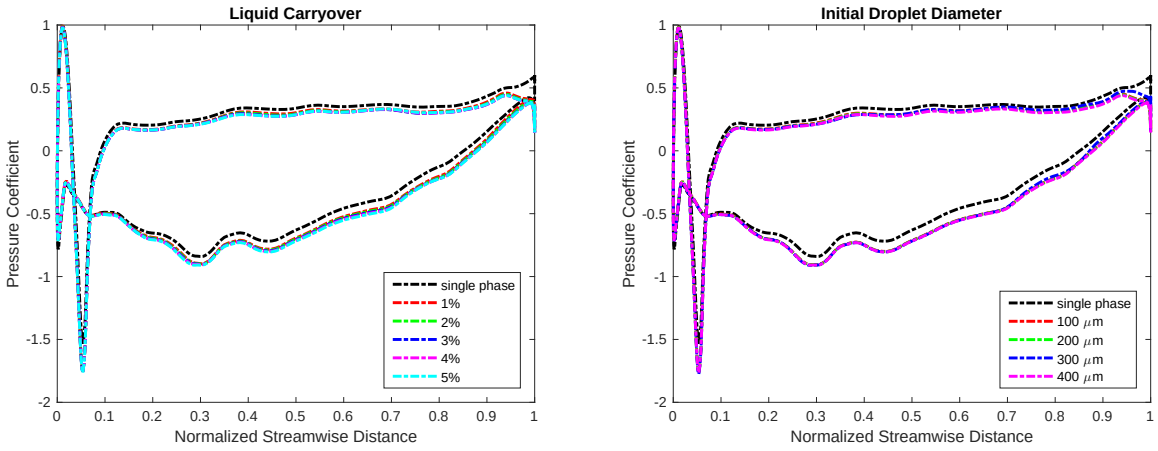

(a) Blade loading near hub

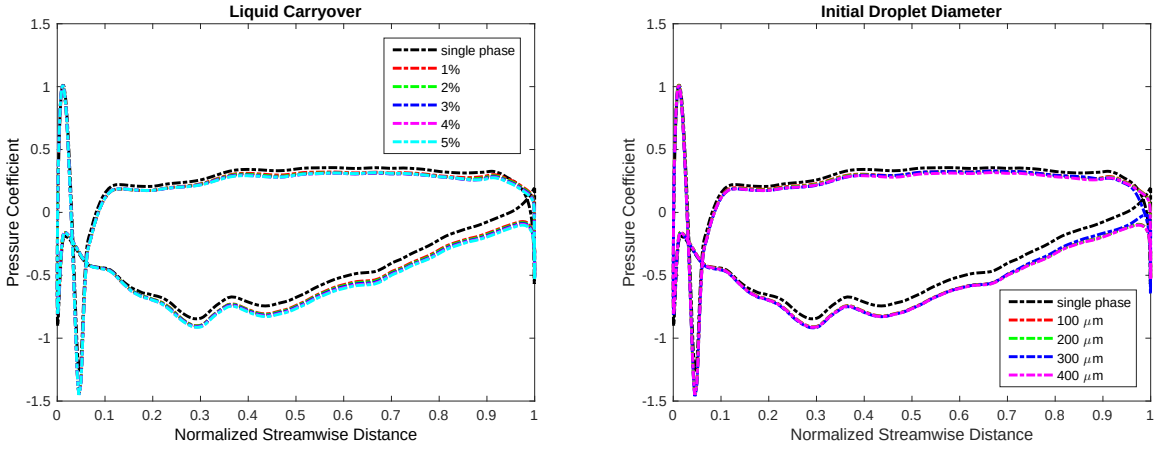

(b) Blade loading near midspan

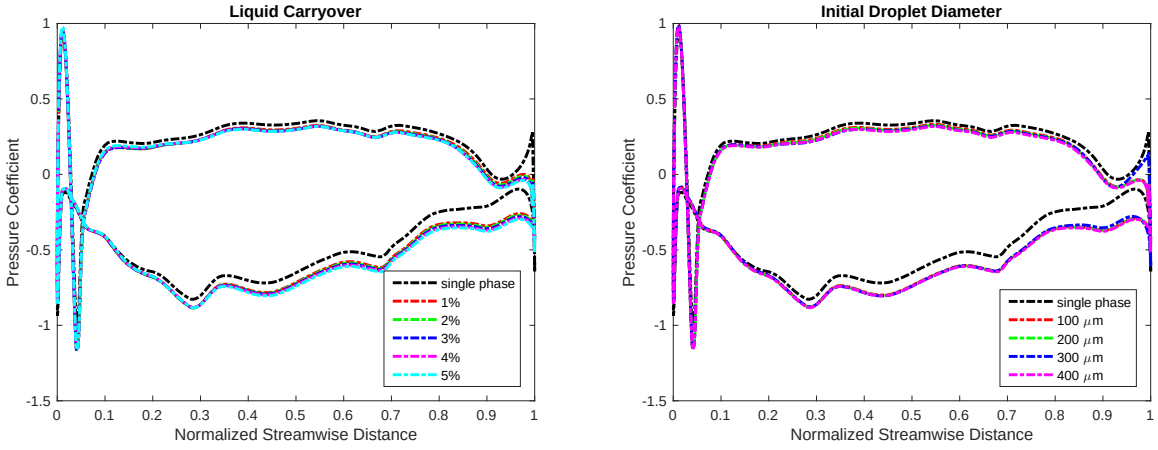

(c) Blade loading near shroud

Figure B.2: Return channel vane blade loading

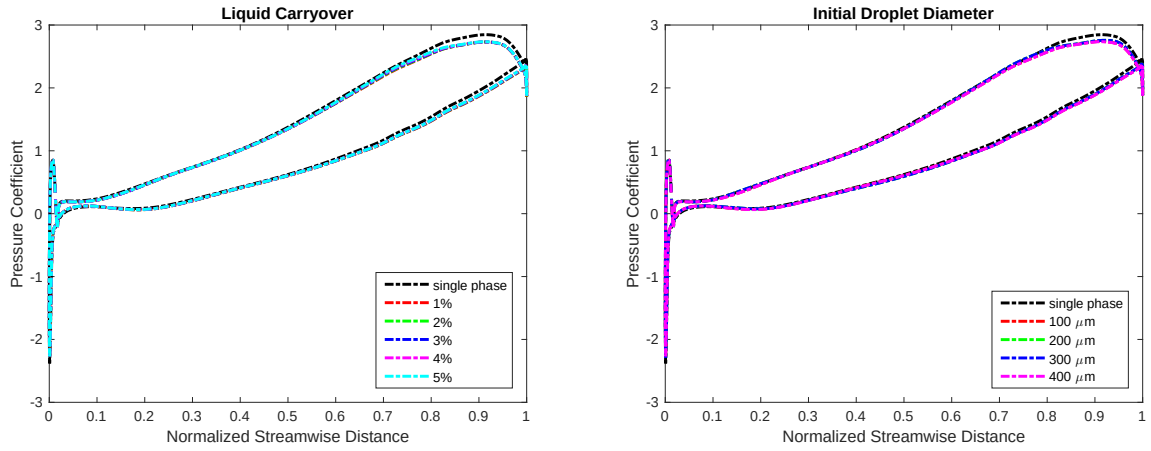

(a) Blade loading near hub

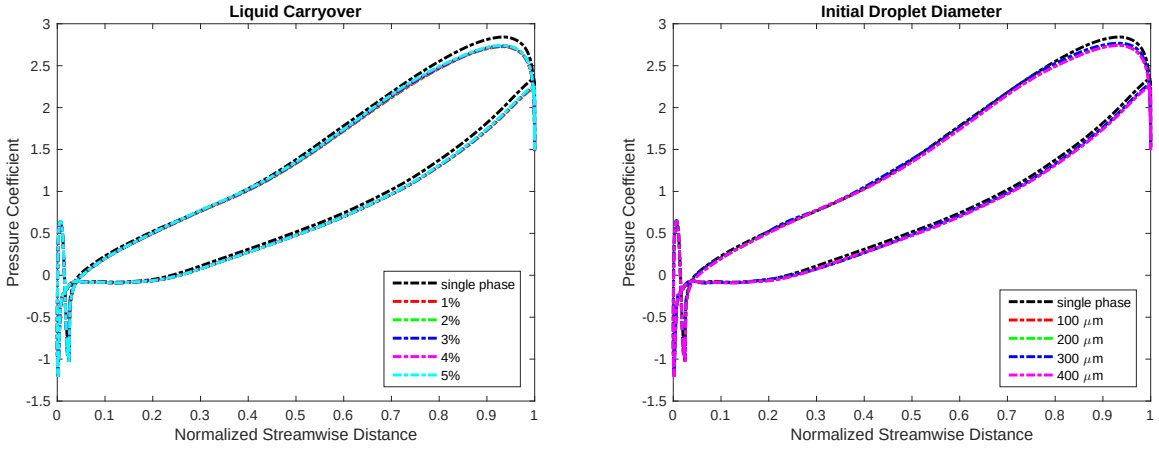

(b) Blade loading near mid-span

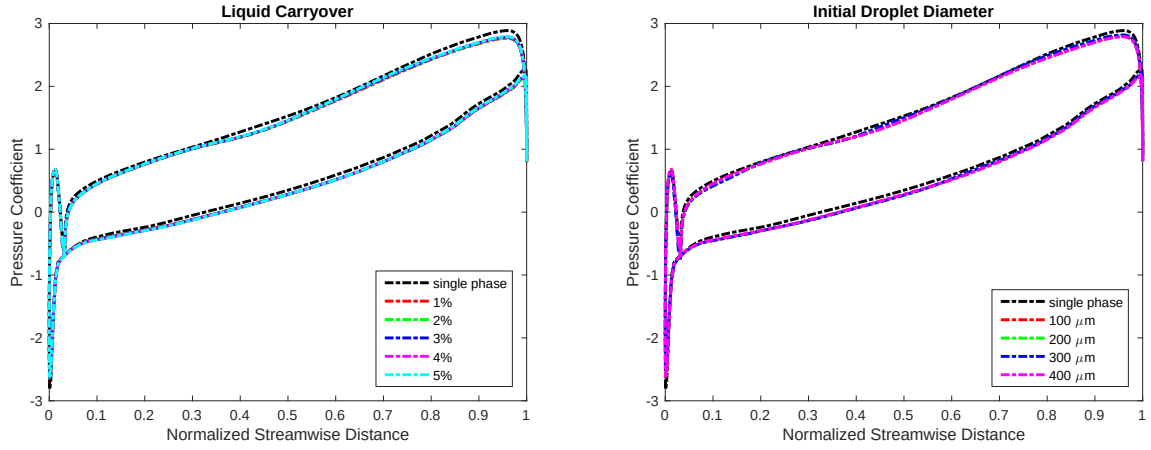

(c) Blade loading near shroud

Figure B.3: Impeller 2 blade loading